Final Report on Probabilistic Cloud Optimized Day-Ahead Forecasting System Based on WRF-Solar

Manajit Sengupta,[1] Pedro A. Jimenez,[2] Ju-Hye Kim,[2] Jaemo Yang,[1] and Yu Xie[1]

1 National Renewable Energy Laboratory
2 National Center for Atmospheric Research

NREL is a national laboratory of the U.S. Department of Energy
Office of Energy Efficiency & Renewable Energy
Operated by the Alliance for Sustainable Energy, LLC

This report is available at no cost from the National Renewable Energy Laboratory (NREL) at www.nrel.gov/publications.

Contract No. DE-AC36-08GO28308

Technical Report
NREL/TP-5D00-81904
March 2022

Final Report on Probabilistic Cloud Optimized Day-Ahead Forecasting System Based on WRF-Solar

Manajit Sengupta,[1] Pedro A. Jimenez,[2] Ju-Hye Kim,[2] Jaemo Yang,[1] and Yu Xie[1]

1 National Renewable Energy Laboratory
2 National Center for Atmospheric Research

Suggested Citation
Sengupta, Manajit, Pedro A. Jimenez, Ju-Hye Kim, Jaemo Yang, and Yu Xie. 2022. *Final Report on Probabilistic Cloud Optimized Day-Ahead Forecasting System Based on WRF-Solar*. Golden, CO: National Renewable Energy Laboratory. NREL/TP-5D00-81904. https://www.nrel.gov/docs/fy22osti/81904.pdf.

NREL is a national laboratory of the U.S. Department of Energy
Office of Energy Efficiency & Renewable Energy
Operated by the Alliance for Sustainable Energy, LLC

This report is available at no cost from the National Renewable Energy Laboratory (NREL) at www.nrel.gov/publications.

Contract No. DE-AC36-08GO28308

Technical Report
NREL/TP-5D00-81904
March 2022

National Renewable Energy Laboratory
15013 Denver West Parkway
Golden, CO 80401
303-275-3000 • www.nrel.gov

NOTICE

This work was authored in part by the National Renewable Energy Laboratory, operated by Alliance for Sustainable Energy, LLC, for the U.S. Department of Energy (DOE) under Contract No. DE-AC36-08GO28308. Funding provided by U.S. Department of Energy Office of Energy Efficiency and Renewable Energy Solar Energy Technologies Office. The views expressed herein do not necessarily represent the views of the DOE or the U.S. Government.

Cover Photos by Dennis Schroeder: (clockwise, left to right) NREL 51934, NREL 45897, NREL 42160, NREL 45891, NREL 48097, NREL 46526.

Acknowledgments

The authors acknowledge Dr. Tassos Golnas and Robert (Bob) Reedy, technology managers of the Systems Integration program of the U.S. Department of Energy Office of Energy Efficiency and Renewable Energy Solar Energy Technologies Office, for their support of this project. The authors also acknowledge Dr. Jimy Dudhia, of the National Center for Atmospheric Research, for providing technical assistance on the development of stochastic perturbations in the Weather Research and Forecasting-Solar Ensemble Prediction System (WRF-Solar EPS); and Dr. Stefano Alessandrini, also from the National Center for Atmospheric Research, for assisting with the analog ensemble technique for the calibration of WRF-Solar EPS forecasts. We thank Grant Buster and Aron Habte, from the National Renewable Energy Laboratory, for their technical assistance and valuable advice and feedback in producing the National Solar Radiation Database (NSRDB) for the WRF-Solar EPS evaluation. The authors also thank Dr. Ralf Giering, from FastOpt GmbH, for the technical assistance and advice in generating efficient derivative codes of WRF-Solar modules with the Transformation of Algorithms in Fortran. Last, we thank Dr. William F. Holmgren, from the University of Arizona, for assisting with the upload of forecast data to the Solar Forecast Arbiter.

List of Acronyms

AnEn	analog ensemble
AOD	Aerosol Optical Depth
BON	Bondville, Illinois
CLD3	Unresolved clouds parameterization module based on relative humidity
CONUS	contiguous United States
CTH	Cloud Top Height
DNI	direct normal irradiance
DRA	Desert Rock, Nevada
FAR	false alarm rate
FARMS	Fast All-Sky Radiation Model for Solar Applications
FPK	Fort Peck, Montana
FWM	forward model
GHI	global horizontal irradiance
GOES	Geostationary Operational Environmental Satellite
GWN	Goodwin Creek, Mississippi
HR	hit rate
KSS	Kuiper's skill score
LSM	land surface model
MAE	mean absolute error
MBE	mean bias error
MRE	missing rate error
MYNN	Mellor–Yamada–Nakanishi–Niino
OPD	cloud optical depth
NSRDB	National Solar Radiation Database
NWP	numerical weather prediction
PBL	planetary boundary layer
POD	probability of detection
PSM	Physical Solar Model
PSU	Pennsylvania State University
RMSE	root mean square error
RRTMG	Rapid Radiative Transfer Model for General Circulation Models
SKEBS	stochastic kinetic energy backscatter scheme
SURFRAD	Surface Radiation Budget
SXF	Sioux Falls, South Dakota
TAF	Transformation of Algorithms in Fortran
TBL	Table Mountain, Colorado
TLM	tangent linear model
WRF-Solar EPS	WRF-Solar Ensemble Prediction System
WRF-Solar PHSY	WRF-Solar multiphysics ensemble
WRF-Solar REF	WRF-Solar reference
WRF-Solar	Weather Research and Forecasting-Solar

Executive Summary

The most persistent challenge in both intraday and day-ahead solar forecasting is to get numerical weather prediction models to produce the right type of clouds with the right frequency at the right time and place. Another challenge is to understand and communicate the forecast uncertainty. The objective of this project was to develop an optimized ensemble-based solar irradiance forecasting system that will (1) demonstrably improve the current state-of-the-art solar forecasts from the deterministic Weather Research and Forecasting-Solar (WRF-Solar) model and (2) provide probabilistic forecasts for grid operations. This probabilistic solar forecasting system, referred to as the WRF-Solar Ensemble Prediction System (WRF-Solar EPS), aims to significantly enhance both the intraday and the day-ahead solar forecasting capability for grid operations.

This technical report summarizes the work performed in the past 3 years through a collaboration between the National Renewable Energy Laboratory and the National Center for Atmospheric Research as part of the U.S. Department of Energy's Solar Forecasting 2 program that aims to improve the accuracy of solar energy forecasts and enable increased deployment of solar energy on the electric grid.

The research steps in developing the ensemble solar forecasting system based on WRF-Solar were:

1. Identify variables that significantly influence the formation and dissipation of clouds and solar radiation through a tangent linear analysis of WRF-Solar modules that influence cloud and radiation processes.
2. Introduce stochastic perturbations in the variables identified in Step 1 to develop the WRF-Solar EPS.
3. Calibrate WRF-Solar EPS using observations to ensure that the forecasts' trajectories are unbiased and provide accurate estimates of forecast uncertainties under a wide range of meteorological regimes.
4. Demonstrate the improvements of WRF-Solar EPS.
5. Develop and deliver an open-source WRF-Solar EPS for the solar energy community.

The first stage of our framework in developing WRF-Solar EPS required a specially designed method using a tangent linear sensitivity analysis to efficiently investigate uncertainties of WRF-Solar variables in forecasting clouds and solar irradiance. We identified 14 variables in this analysis (Yang et al. 2021a). For the second stage, we introduced stochastic perturbations in the 14 variables to generate the ensemble members. A user-friendly interface was developed in WRF-Solar EPS to enable the control of the parameters of stochastic perturbations using configuration files. Last, we implemented an analog technique as an ensemble post-processing method to calibrate the solar irradiance probabilistic forecasts (Kim et al. 2021). For the evaluation of the forecasts, we adapted and used satellite-derived solar radiation data from the National Solar Radiation Database (NSRDB) as well as in situ observations (Jiménez et al. 2022). The improvements obtained by the ensemble calibration reduced forecast bias by 81% and 75% with respect to the stochastic ensemble for global horizontal irradiance (GHI) and direct normal irradiance (DNI), respectively. Overall, the ensemble forecasts calibrated from the analog

method provided unbiased estimations of the irradiance within 1% and 3.2% of the satellite observations of GHI and DNI, respectively.

The probabilistic WRF-Solar system, referred as WRF-Solar EPS, developed under this project is now publicly available and will form part of the next WRF major release in 2022 to support the integration of solar generation resources and improve the accuracy of intraday and day-ahead probabilistic solar forecasts.

Table of Contents

List of Figures

List of Tables

1 Introduction

The contribution of solar energy to the electric grid has been rapidly increasing during the last few years, and it has reached a point where integration has become a major source of concern for system operators. One cost-effective integration method is the use of solar irradiance and energy forecasts to improve both the unit commitment and dispatch of this variable resource.

To help integrate solar generation resources, the U.S. Department of Energy is now seeking to improve the accuracy and the ease of delivery of both day-ahead and intraday solar forecasts. This is the second phase of funding for solar forecasting technologies. In the first phase of funding, the Weather Research and Forecasting model was enhanced to better support for solar applications (WRF-Solar) (Jiménez et al. 2016a) by the National Center for Atmospheric Research and its partners. Developments focused on improving the representation of processes that impact solar irradiance on the ground. More specifically, WRF-Solar was developed to provide accurate solar forecasts through significant improvements in the representation of aerosols, cloud formation, and radiative transfer calculations.

Operational weather forecasts are usually derived from single model runs because of the high computational cost of running high-resolution forecasts. This means that there is little or no information about the uncertainty of the forecast. A key challenge in integrating solar resources is accurately predicting the confidence in a forecast of solar power. This can be achieved by creating an ensemble of forecasts through the optimized perturbation of initial conditions and generating a probabilistic forecast using the ensemble members. Systems such as the National Oceanic and Atmospheric Administration's Global Ensemble Forecast System and the National Hurricane Center's Track and Intensity models produce ensemble-based probabilistic forecasts geared toward specific weather events, but there are no systems that are tuned to optimally provide a probabilistic forecast for solar energy.

A high-quality probabilistic forecasting system would result in forecasts that can be used as a decision aid by system operators, utilities, and market participants. This will result in an increase in both the penetration and value of solar energy by significantly reducing the cost of integration; however, no easy-to-use probabilistic forecasting model optimized for solar energy applications exists in the public domain, and the proposed system would fill a significant gap in existing capabilities.

WRF-Solar is currently being enhanced, and it has robust basis for developing probabilistic forecasts for the solar energy community. The development of a publicly available model for probabilistic solar forecasts building on the capabilities of WRF-Solar is a natural progression of development in the solar forecasting arena, and it can provide a low-risk pathway to significant enhancement in the ability of the energy industry to produce actionable information for grid operations.

The objective of this project is to develop an optimized ensemble-based solar forecasting system that will:

- Demonstrably improve the current state-of-the-art solar forecasts.
- Provide probabilistic forecasts for grid operations.

The research steps in developing the ensemble solar forecasting system based on WRF-Solar, as shown in Figure 1, are:

1. Identify variables that significantly influence the formation and dissipation of clouds and solar radiation through a **tangent linear analysis** of WRF-Solar modules that influence cloud processes.
2. Introduce stochastic perturbations in the variables identified in step (1) to develop the **WRF-Solar Ensemble Prediction System (WRF-Solar EPS).**
3. **Calibrate WRF-Solar EPS** using observations to ensure that the forecasts' trajectories are unbiased and provide accurate estimates of forecast uncertainties under a wide range of meteorological regimes.
4. **Demonstrate the improvements of WRF-Solar EPS.**
5. Develop and deliver an **open-source WRF-Solar EPS** for the solar energy community.

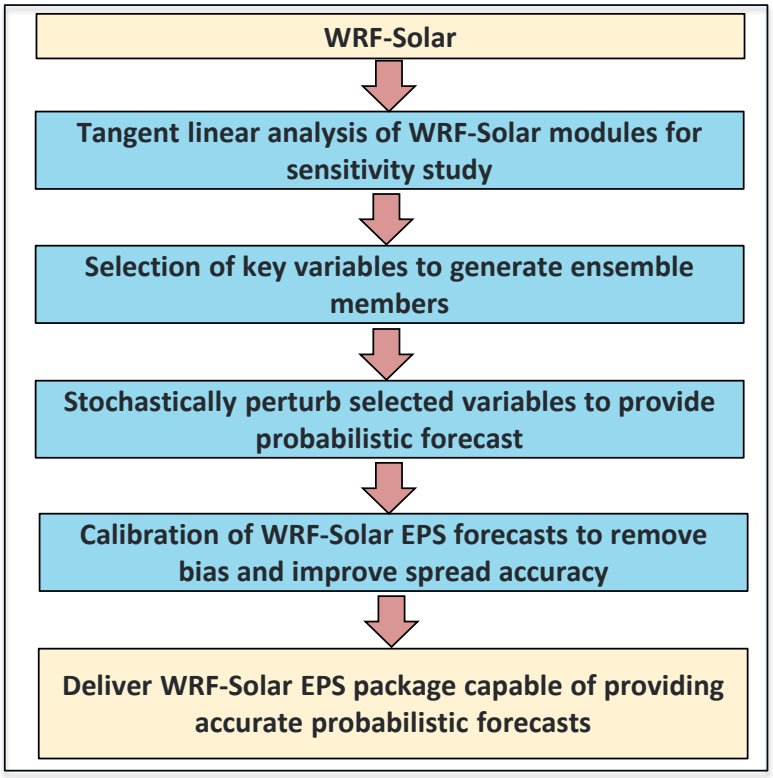

Figure 1. Research flowchart for the WRF-Solar EPS development

The forecasting system we developed, referred as WRF-Solar EPS, is now ready to be disseminated to support the integration of solar generation resources and improve the accuracy of intraday and day-ahead probabilistic solar forecasts (Sengupta et al. 2021, 2022; Jiménez et al. 2021). These activities were conducted during a 3-year period spanning 2018–2021, and this report summarizes activities conducted through a collaboration between the National Renewable Energy Laboratory and the National Center for Atmospheric Research under the project.

2 Data Acquisition for Model Calibration and Validation

2.1 Development of 9-km National Solar Radiation Database for WRF-Solar Ensemble Prediction System Evaluation and Calibration

Numerical weather prediction (NWP) developers and forecast users need to evaluate forecast outputs at arbitrary locations on the model grid; thus, an important requirement for evaluating the forecasts is to build the gridded observations that match the NWP grid because the spatial resolution and the projection of the two data sets are dissimilar. To achieve this task, we aggregated the National Solar Radiation Database (NSRDB) data (Sengupta et al. 2018) (2 km or 4 km) to the WRF-Solar grid points (9 km). In addition, we reprocessed the native NSRDB to produce data for originally excluded parts of the domain over the ocean. This provides us the capability to evaluate the full extent of the WRF-Solar forecasts, including oceans and the contiguous United States (CONUS). Multiyear NSRDB data sets, which cover the period from 2016–2018, were reprocessed and finally aggregated to the WRF-Solar grid. We created a full inventory of native NSRDB for the newly processed NSRDB (9 km), and this enables us to provide insights on the predictive capability of the WRF-Solar ensemble forecasts in terms of irradiance variables and cloud properties.

While processing the satellite data sets to produce the 9-km NSRDB, we identified that uncertainties in cloud properties are influenced by viewing geometry (e.g., satellite viewing angle), with the Geostationary Operational Environmental Satellite- (GOES)-East and GOES-West satellites producing different results in some of the overlapping regions. This implies that it is necessary to consider the viewing geometry dependence of retrieved cloud properties from satellites when we are evaluating the solar forecasts. To address this concern, we produced the 9-km NSRDB based on viewing angles of the GOES satellites, which differs from the current blending method used in the existing version of the NSRDB.

Figure 2 exhibits the satellite viewing angle calculated from GOES-East on the 9-km WRF-Solar grid. The black shadow denotes the area when the viewing angle of GOES-East is larger than 70°. We consider the viewing angle cutoff at 70° because angles beyond that cause serious off-nadir view angle effects for GOES-East. For the black shadow area, retrieved cloud properties from GOES-West are included in the processing of the 9-km NSRDB, and GOES-East data are used for the remaining parts of the domain.

The following are the main steps of processing the 9-km NSRDB:

1. We generate 2-km NSRDB in which the data sets obtained from GOES-East and GOES-West satellites are processed through the Physical Solar Model (PSM) and combined by stitching at 105°W longitude.
2. Another 2-km NSRDB is produced from Step 1 but with 123°W longitude as the line for merging the two satellites.
3. A data aggregation is conducted to generate two sets of half-hourly, 9-km NSRDB (processed by 105°W and 123°W longitudes merging longitudes, respectively) from the native data sets (2 km).

4. We select data from the two sets of the 9-km NSRDB—which are referred to as the 9-km_NSRDB_105°W and the 9-km_NSRDB_123°W, based on satellite viewing angle (**Figure 2**)—to produce the final products.

Note that the 123°W and 105°W longitudes used in our method indicate the approximate longitude at the southwest corner of the WRF-Solar grid and the closest line to the center of common area of two satellites, respectively; thus, the 9-km_NSRDB_123°W includes a larger extent from the GOES-East data than the 9-km_NSRDB_105°W. In Step 4, we produce the final product by selecting data from the 9-km_NSRDB_123°W for the area where the viewing angle of GOES-East is smaller than 70° and data from the 9-km_NSRDB_105°W for the black shadow area (viewing angle >70°) in **Figure 2**. The newly processed NSRDB data sets have been used for the validation of the WRF-Solar models (Jiménez et al. 2022; Kim et al. 2021; Yang et al. 2021b; Xie et al. 2022).

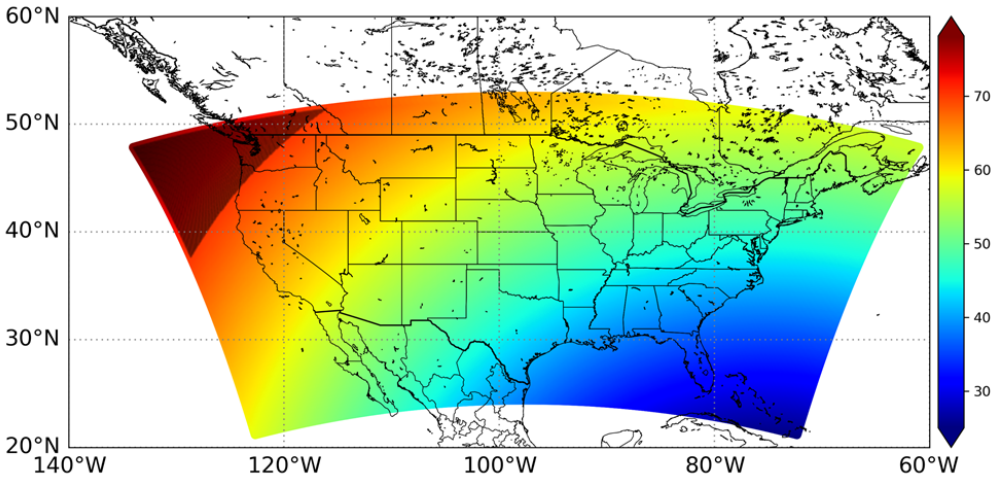

Figure 2. Viewing angle (degrees) for the GOES-East satellite. The area where the viewing angle is larger than 70° is indicated by the dark red color.

2.2 Evaluation of 9-km National Solar Radiation Database Against Ground Observations

The 9-km, half-hourly NSRDB data sets were compared with ground-measured data. The ground observations obtained from seven Surface Radiation Budget (SURFRAD) network sites that provide 1-minute data were used to evaluate the 9-km NSRDB data set. **Table 1** includes general information for locations of the ground measuremnts. The NSRDB global horizontal irradiance (GHI) data for the years 2016–2018 were analyzed for each measurement location. Averaged SURFRAD observations over a 30-minute time interval (e.g., averaged 1-minute observations from hh:15 to hh:45) were considered to assess the performance of the NSRDB GHI. Prior to comparing between the NSRDB and ground observations, we filtered the two data sets using the following criteria (Habte et al. 2017):

- 0° < solar zenith angles < 85°
- GHI > 0 W/m^2
- Missing values of ground observations are not included in the data sets.
- Cloud types from the NSRDB are used to determine clear-/cloudy-sky conditions.

Table 1. Information on SURFRAD Sites

Name	Latitude (°N)	Longitude (°W)	Elevation (m)	Time Zone
Table Mountain, CO (TBL)	40.12	105.24	1689	UTC-7
Bondville, IL (BON)	40.05	88.37	230	UTC-6
Fort Peck, MT (FPK)	48.31	105.10	634	UTC-7
Goodwin Creek, MS (GWN)	34.25	89.87	98	UTC-6
Penn. State Univ., PA (PSU)	40.72	77.93	376	UTC-5
Desert Rock, NV (DRA)	36.62	116.02	1007	UTC-8
Sioux Falls, SD (SXF)	43.73	96.62	473	UTC-6

Four statistical metrics were used for the evaluation of the NSRDB against ground-measured observations: mean absolute error (MAE) (W/m^2), mean bias error (MBE) (W/m^2), normalized MAE (%), and normalized MBE (%), which are determined as follows:

$$MAE\ (W/m^2) = \frac{1}{N}\sum_{N}|X - O| \tag{2.1}$$

$$MBE\ (W/m^2) = \frac{1}{N}\sum_{N}(X - O) \tag{2.2}$$

$$Normalized\ MAE\ (\%) = \frac{\frac{1}{N}\sum_{N}|X - O|}{\bar{O}} \times 100\ (\%) \tag{2.3}$$

$$Normalized\ BIAS\ (\%) = \frac{\frac{1}{N}\sum_{N}(X - O)}{\bar{O}} \times 100\ (\%) \tag{2.4}$$

where the ground-measured GHI is denoted by O, the NSRDB GHI is represented by X, N is the total number of data pairs, and $\bar{O}$ is the ground-measured GHI average over the N values used in the calculation.

The comparison of the NSRDB against the ground observations using global statistical metrics are presented in **Figure 3**. The normalized MAEs computed with all available data for the period from 2016–2018, indicated by 3-YRS in **Figure 3b**, show that the 9-km NSRDB provides more accurate GHI in clear-sky (MAE: 4%–8%) than cloudy-sky (MAE: 22%–28%) conditions. The normalized MBE for 3-YRS is less than 5% with respect to the GHI under all-sky, clear-sky, and cloudy-sky conditions for all stations; however, the 9-km NSRDB produces positive MBEs, indicating GHI overestimation (**Figure 3d**).

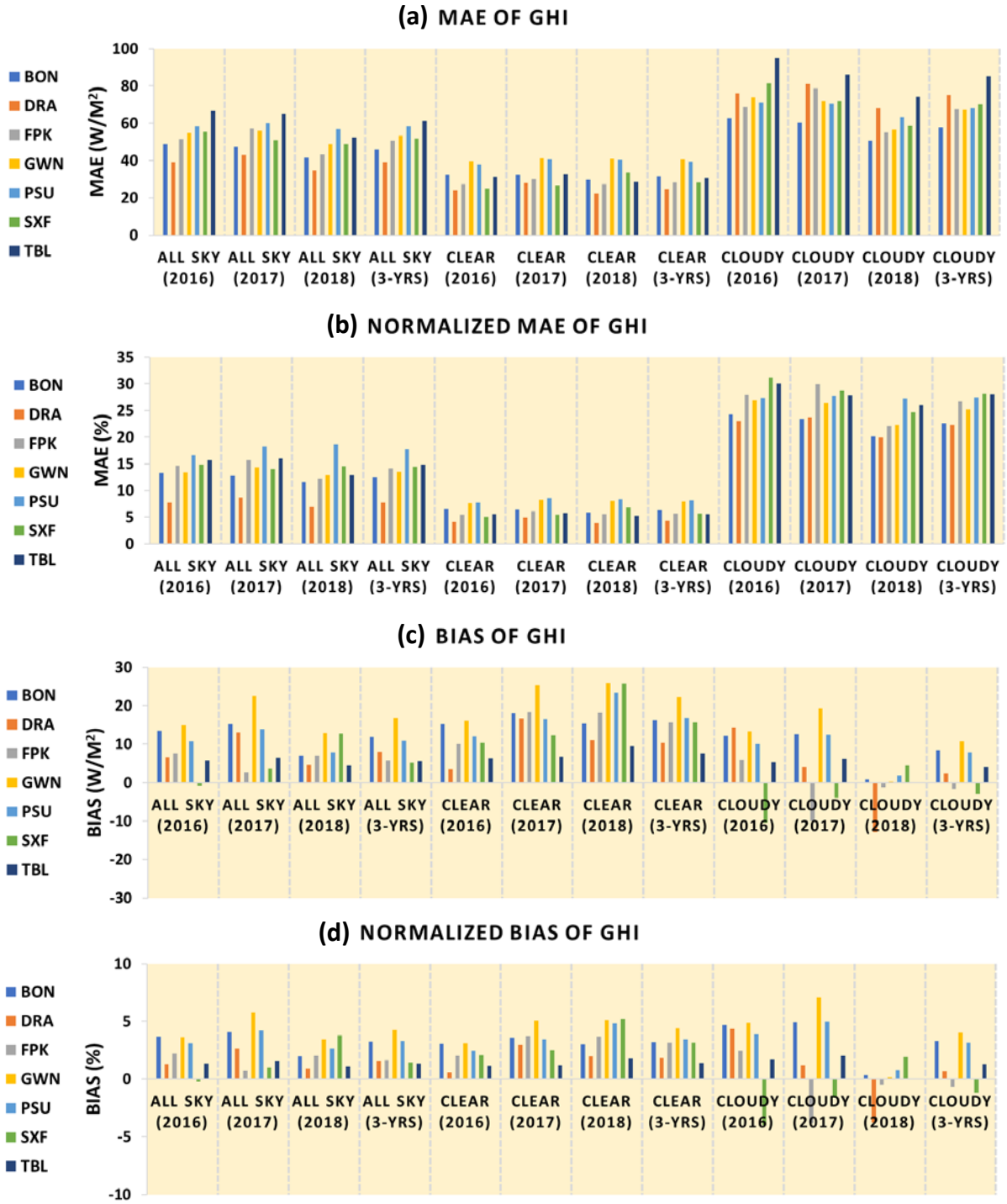

Figure 3. (a) MAE (W/m^2), (b) normalized MAE (%), (c) MBE (BIAS) (W/m^2), and (d) normalized MBE (BIAS) (%) of the 9-km NSRDB GHI computed with all available data for seven SURFRAD sites for the period from 2016–2018

Comparing the statistical metrics of the 2018 NSRDB with the 2016 and 2017 NSRDB data sets demonstrates notable improvement in the MAE and MBE (**figures 3a and 3c**). The 2018 NSRDB shows considerable reduction in the MAE of GHI across most of the seven SURFRAD sites compared to the 2016 and 2017 GHI data sets in all-sky conditions. The improvements in

the 2018 NSRDB are attributed to the use of quarter-hourly, 2-km data of cloud properties retrieved from GOES-16, which has a higher temporal and spatial resolution than cloud data obtained from GOES-13 (half-hourly, 4 km was used in producing the data sets for the 2016 and 2017 NSRDB). Especially for the BIAS in cloudy-sky conditions, the 2018 NSRDB produces BIAS values near zero for all stations except the DRA site (**Fig 3c**). To summarize the results in **Figure 3**, we calculated the average of the MAE and BIAS for seven SURFRAD sites under three sky conditions (**Figure 4**). Improvements in the 2018 NSRDB are shown for all-sky and cloudy-sky conditions, indicated by the MAE reductions of approximately 13% (cloudy: 19%) and 14% (cloudy: 18%) compared to the 2016 and 2017 data sets, respectively (**Figure 4a**). The MAEs of the three data sets are similar under clear-sky conditions. Consistent with the results in **figures 3c and 3d**, the 2018 NSRDB shows good agreement with the ground measurements with an average BIAS of almost zero (**Figure 4b**).

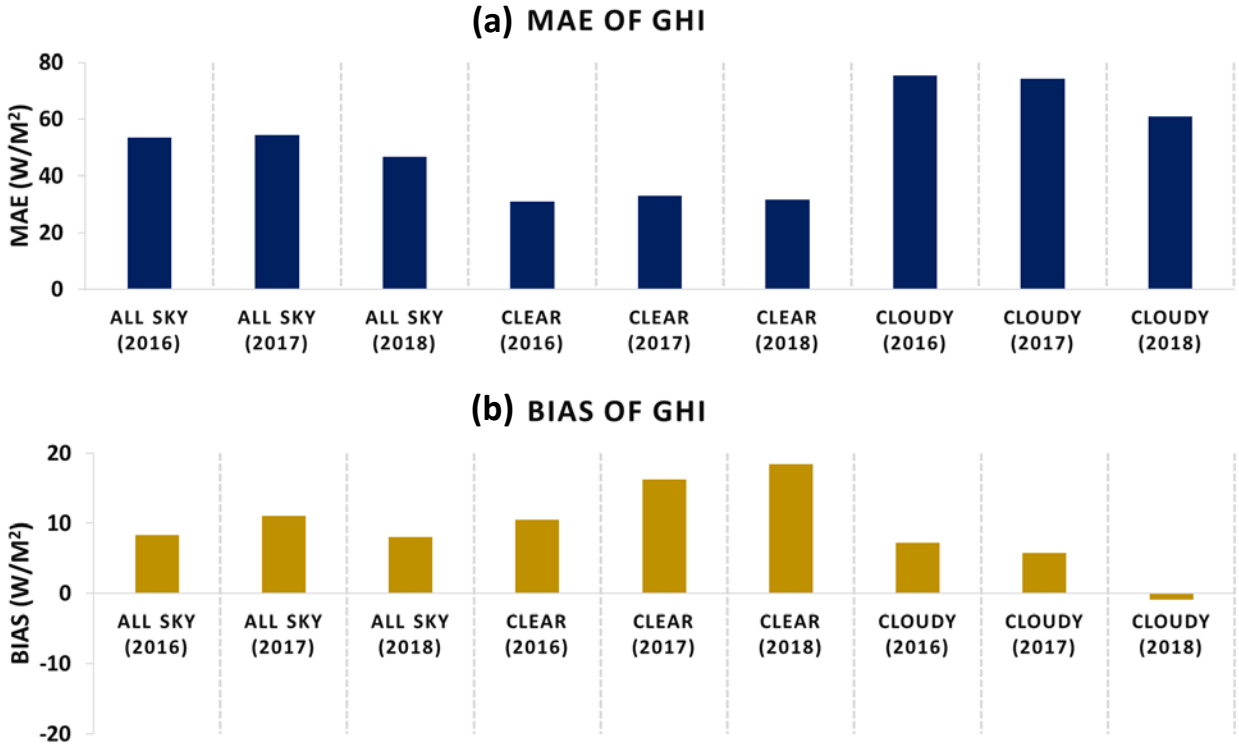

Figure 4. (a) MAE (W/m^2) and (b) MBE (BIAS) (W/m^2) of GHI averaged across seven SURFRAD sties for the 2016, 2017, and 2018 9-km NSRDB data sets

3 WRF-Solar Ensemble Prediction System Development

3.1 Tangent Linear Analysis

3.1.1 Theory of Tangent Linear and Automatic Differentiation Tool

The first stage of the project framework in developing WRF-Solar EPS required a specially designed method using a tangent linear analysis to efficiently investigate uncertainties of WRF-Solar variables in predicting clouds and solar irradiance (Yang et al. 2021a). To develop the tangent linear version of the modules for the sensitivity analysis, we selected six modules that affect solar irradiance and directly impact the representation of clouds. In particular, CLD3 parameterization was newly added to the tangent linear analysis. (The original plan was to implement a sensitivity analysis for five WRF-Solar modules.)

WRF-Solar physics modules selected for the tangent linear analysis:

- Fast All-Sky Radiation Model for Solar Applications (FARMS) (Xie, Sengupta, and Dudhia 2016)
- Thompson microphysics (Thompson, Rasmussen, and Manning 2004; Thompson et al. 2008)
- Mellor–Yamada–Nakanishi–Niino (MYNN) for the planetary boundary layer (PBL) (Nakanishi and Niino 2009)
- Deng shallow cumulus system (Deng, Seaman, Kain 2003)
- Unresolved clouds parameterization module based on relative humidity (CLD3)
- Noah land surface model (LSM) (Chen and Dudhia 2001)

The tangent linear models (TLMs) for each of the six WRF-Solar modules selected were developed using the Transformation of Algorithms in Fortran (TAF) (Talagrand 1991; Giering and Kaminski 1998) software. TAF is a tool for automatic differentiation. TAF is a source-to-source transformation tool for functions written in Fortran 90/95 or Fortran 77. This means that TAF accepts functions defined by source code in either language, with a few restrictions. From this source code, TAF can generate derivative code that operates either in forward mode or in reverse mode. Via command line options, the user can influence the coding standard of the generated code. Applying TAF recursively, code for the evaluation of higher-order derivatives can be generated. For functions defined by a program, automatic differentiation constitutes an alternative way of providing derivatives. The source code of a program represents a decomposition of the underlying (composite) function into elementary functions. On the level of these elementary functions, derivatives (or local Jacobian matrices) can be derived according to simple rules. According to the chain rule, the product of all the local Jacobians represents the derivative of the composite function. These multiple products of local Jacobians can be evaluated in arbitrary order; any order will yield the same result, but the computational cost usually depends strongly on the order. If the evaluation works in the order given by the function, the derivative algorithm is said to operate in forward (or tangent linear) mode. If it works in the opposite order, the derivative algorithm is said to operate in reverse (or adjoint) mode. The computational resources needed in forward mode, similar to those of divided differences, are

proportional to the number of independent variables. In reverse mode, they are proportional to the number of dependent variables.

The TAF software package enables the sensitivity analysis of complex functions that have been coded into Fortran. TAF generates tangent linear code of forward models (FWMs) that evaluates the derivative of the output variables with respect to the input variables, thereby providing the capability to analyze the sensitivity of the input variables to the output.

For this project, TAF was used to analyze the sensitivity of six different WRF-Solar modules that influence clouds and solar irradiance. Among other outputs for the module, the TAF-generated TLM provides the derivative of output variables with respect to input variables, and this is the information we use for our analysis. Prior to transforming the numerical codes of WRF-Solar to the TLMs, we extracted the selected modules from WRF-Solar, the FWMs, for the efficient development of the TLMs and their subsequent sensitivity analysis of the output variables under a variety of conditions.

The TLM is derived from the FWM. The FWM is defined as:

$$\mathbf{Y} = M(\mathbf{X}) \tag{3.1}$$

where M is the FWM (in our case, the WRF-Solar modules), $\mathbf{X}$ is the $n \times 1$ vector of the input variables of M, and $\mathbf{Y}$ is the $m \times 1$ vector of the output variables of M. The tangent linear operator ($\mathbf{J}$), also called the Jacobian matrix, contains the partial derivatives of the FWM (Eq. 3.1) with respect to the input variables, and it is given by:

$$\mathbf{J} = \frac{\partial \mathbf{Y}}{\partial \mathbf{X}} \tag{3.2}$$

where $\mathbf{J}$ is a $m \times n$ matrix, where m and n are the number of output variables and input variables, respectively. For the WRF-Solar modules, each component of $\mathbf{J}$ in Eq. 3.2 estimates the influence of each input variable on the individual output variables.

The validity of the TLM generated by TAF as a linear approximation of the nonlinear model, the FWM, should be verified. This is verified with a linearity test. The linearity test compares the ratio of the derivatives in Eq. 3.2 calculated with the FWM and the derivatives from the TLM, e.g., Xiao et al. (2008) and Zhang, Huang, and Pan (2013). The derivatives with the FWM are calculated using the derivative definition, which requires introducing perturbations to the input variables. The metric for the linearity test is determined as follows:

$$\Phi(\Delta\mathbf{X}) = \frac{\|M(\mathbf{X} + \Delta\mathbf{X}) - M(\mathbf{X}))\|}{\|\Delta\mathbf{X} \cdot \mathbf{J}\|}, \lim_{\Delta\mathbf{X} \to 0} \Phi(\Delta\mathbf{X}) = 1 \tag{3.3}$$

where $\Delta\mathbf{X}$ is a perturbation, $M(\mathbf{X} + \Delta\mathbf{X})$ and $M(\mathbf{X})$ are perturbed FWM and FWM outputs, and $\mathbf{J}$ is the sensitivity from the TLM (Eq. 3.2). In Eq. 3.3, as the perturbations decrease and approach zero, the ratio $[\Phi(\Delta\mathbf{X})]$ should converge to 1 if the TLM has been correctly generated by TAF. The input variables of the WRF-Solar modules have quite different characteristic values, e.g., $5 \cdot 10^{-3}$kg/kg for water vapor mixing ratio and 300K for temperature; thus, reasonable perturbations, which are small enough to calculate the derivatives with the FWM, are applied to input variables in this linearity test. The model state inputs ($\mathbf{X}$) calculated from the WRF-Solar

simulations are used because this builds confidence in the validation of the TLMs for realistic scenarios under all-sky conditions (see Section 3.1.2).

Table 2 shows the results of the linearity test for the six WRF-Solar modules. $\Phi(\Delta\mathbf{X})$ was repeatedly calculated with all perturbed input variables of the individual modules and with 128-bit precision. Clearly, $\Phi(\Delta\mathbf{X})$ converges to 1 as the magnitude of the perturbations is reduced. This indicates that the TLMs accurately approximate the derivatives of the output variables with respect to the input variables. We also performed the test by perturbing the input variables individually and found that in all cases the results converged, similar to the results shown in **Table 2**. In summary, the linearity tests were conducted to validate the accuracy of the TLM by comparing the results from the perturbations of the FWM.

Table 2. Validation Results of TLMs Developed for WRF-Solar Modules

Relative Perturbation						
Perturbation	$\Phi(\Delta\mathbf{X})$					
	FARMS	Thompson Microphysics	MYNN-PBL	Deng Shallow Cumulus	CLD3	Noah LSM
0.10000000000000000·**X**	1.00382202657812190	8.40532778431445196	0.06686879658617226	0.09818640407425982	0.07946947745956231	1.95871019138368918
0.01000000000000000·**X**	1.00112431685746888	3.58213603506903987	0.39812514470897838	0.98148044148417833	0.62022510991009561	1.07012301126729319
0.00100000000000000·**X**	1.00002193066539698	0.98876942531880101	0.65799013982880905	2.73987449915886884	1.26337810990238063	1.00670638148017697
0.00010000000000000·**X**	1.00000219754714054	0.99995285758007716	0.95825212484169588	0.99879600028879147	0.98030439222280128	1.00066760665367331
0.00001000000000000·**X**	1.00000021979951057	0.99999322280220673	0.99579498903314501	1.00059113905074119	0.99794703609719434	1.00006673038986377
0.00000100000000000·**X**	1.00000002198039901	0.99999930093096164	0.99957929378280519	1.00007797560531154	0.99979381727280132	1.00000667274218920
0.00000010000000000·**X**	1.00000000219804438	0.99999992987887805	0.99995792742856240	1.00000798529004398	0.99997937280779208	1.00000066727717477
0.00000001000000000·**X**	1.00000000021980448	0.99999999298574490	0.99999579272346088	1.00000080044709553	0.99999793719152780	1.00000006673367082
0.00000000100000000·**X**	1.00000000002198044	0.99999999929855306	0.99999957927215227	1.00000008009434688	0.99999979371826021	1.00000000667935040
0.00000000010000000·**X**	1.00000000000219804	0.99999999992985509	0.99999995792721332	1.00000000804037734	0.99999997937181710	1.00000000067391866
0.00000000001000000·**X**	1.00000000000021980	0.99999999999298551	0.99999999579272135	1.00000000083479343	0.99999999793718162	1.00000000007337549
0.00000000000100000·**X**	1.00000000000002198	0.99999999999929855	0.99999999957927217	1.00000000011423317	0.99999999979371816	1.00000000001332117
0.00000000000010000·**X**	1.00000000000000219	0.99999999999992986	0.99999999995792725	1.00000000004217712	0.99999999997937182	1.00000000000731574
0.00000000000001000·**X**	1.00000000000000022	0.99999999999999299	0.99999999999579276	1.00000000003497152	0.99999999999793718	1.00000000000671520
0.00000000000000100·**X**	1.00000000000000002	0.99999999999999930	0.99999999999957931	1.00000000003425096	0.99999999999979372	1.00000000000665515
0.00000000000000010·**X**	1.00000000000000000	0.99999999999999993	0.99999999999995797	1.00000000003417890	0.99999999999997937	1.00000000000664915
0.00000000000000001·**X**	0.99999999999999997	0.99999999999999998	0.99999999999999581	1.00000000003417169	0.99999999999999793	1.00000000000664856

3.1.2 Method for Quantifying Uncertainties of WRF-Solar Variables in Tangent Linear Analysis

To investigate uncertainties of the output variables with respect to the uncertainties in the input variables of the parameterizations under investigation, we first identified a large set of atmospheric states with the input variables, **X**, to run the TLMs. For these purposes, we used both WRF-Solar simulations and satellite-derived data.

The satellite-derived data were used only for providing the input variables to the FARMS module. For FARMS, the analysis was performed independently for clear-sky and cloudy-sky conditions. Data obtained from the NSRDB (Sengupta et al. 2018), which provides gridded observations at a 4-km horizontal resolution for each 30-minute interval, were used for the FARMS input variables. We extracted 2017 CONUS data for nine parameters—solar zenith angle, surface pressure, surface albedo, Ångström wavelength exponent, aerosol optical depth (AOD), asymmetry factor of aerosol, total precipitable water, cloud optical depth, and cloud effective radius—which correspond to FARMS inputs. The data were processed to determine the minimum, maximum, and percentiles, and the information was used to generate cases for clear-sky and cloudy-sky conditions for the FARMS sensitivity analysis. For the clear-sky condition, 8,100 input vectors (**X**) were generated with various combinations of input parameters given the constraint of the lower 5% and the upper 95% percentiles. The cloud optical depth and the cloud effective radius were set to zero in this set of input vectors. In general, uncertainties in

calculating the solar irradiance are larger in cloudy regions than the regions where no clouds exist; therefore, we examined more cloudy cases in the sensitivity analysis of FARMS. For cloudy-sky conditions, 262,144 input vectors were considered, with cloud optical depths and effective radius being positive quantities.

The input variables to the other WRF-Solar modules were obtained from a WRF-Solar simulation. The WRF-Solar domain covered CONUS at a 9-km horizontal grid spacing. The National Centers for Environmental Prediction Global Forecast System (0.25° x 0.25°; 3-hourly intervals) forecast data were used for the initial and boundary conditions. The forecast spanned the period from 0000 UTC April 15–0000 UTC April 16. The forecast provided the input variables to the TLMs of the other five parameterizations under this study.

The sensitivities from the TLMs (**J**) were used to calculate the uncertainties in the output variables. In this derivation, we used the derivatives of the output variables with respect to the input variables provided by the TLMs (**J**) and estimations of the uncertainties in the input variables (see X_E in Eq. 3.4). This procedure serves two purposes: (1) It provides us realistic weighting based on estimates of input uncertainty, and (2) it removes dependence on the input units (Yang et al. 2019) and allows a direct intercomparison of the importance of particular input variables. For example, GHI is very sensitivity to the solar zenith angle; however, the uncertainty in calculating the solar zenith angle is small, which leads to the small impact of the uncertainty of solar zenith angle on the GHI estimation.

By multiplying the sensitivity calculated from the TLM (Eq. 3.2) by the uncertainty in the input variable, we obtain the uncertainty in the output variable:

$$\frac{\partial Y}{\partial X} \cdot X_E = Y_U \tag{3.4}$$

where X and Y are the input and the output variables of the WRF-Solar module, respectively; X_E is the representative value of the uncertainty in the input variable; $\frac{\partial Y}{\partial X}$ is the sensitivity or the partial derivate from the TLM; and Y_U is the uncertainty of the output variable resulting from the uncertainty in the input variable. Note that there is a linear relationship between the uncertainty in the output variables (Y_U) and the uncertainty in the input variables (X_E). If the uncertainty of the input variables is increased (or reduced) by a factor of two, then the uncertainty in GHI estimation, for example, will be doubled (or halved).

Perfectly representing the actual uncertainty of the input variables for individual WRF-Solar modules is difficult because of the limited availability of the observations for all meteorological variables and for the vertical layers of the WRF-Solar model. In this study, the uncertainties in the input variables, X_E, are estimated using three strategies: (1) an error determined based on our experience; (2) a standard deviation of the input variables, X, calculated with the 1-day WRF-Solar simulation; and (3) the input value itself (i.e., $X_E = X$). Even though this methodology is very basic, our choice of the uncertainty estimation with three approaches considers different characteristics for the input variables and yields approximately the representative value of the input errors without actual observations.

In the first approach, the uncertainties were determined based on our experience. This approach involves a certain degree of subjectivity, but it takes advantage of the error estimation for some two-dimensional variables where the representative value of the error can be inferred empirically without actual measurements. This method was also used for the three-dimensional variables, which have low variability over whole atmospheric layers, in which case the uncertainty was estimated by using an absolute change as a percentage of the value of the input variable in the vertical layers (e.g., 10% of X as X_E).

In the second approach, the uncertainties were estimated by the standard deviation of the input variable. We calculated the standard deviation at each vertical layer independently. For each vertical layer, the standard deviation was computed with all predicted model state values across the model grid (CONUS) and the simulation period (1 day). Additionally, the uncertainty of specific variables was estimated for the ocean grid points separately to further assess the model state uncertainties. This approach is used for the variables that have relatively higher variability over land in regions of the complex terrain, such as water vapor, Exner pressure, and pressure.

In the third approach, we assumed that the uncertainties are the values of the input variables. This method might be suitable if the variability of the input variable is high across the vertical layers.

For this study, we selected the appropriate combinations of error estimation schemes for each input variable and each WRF-Solar module. Note that we opted to use the first method in FARMS because it was possible to estimate the uncertainties for all input variables based on our experience with WRF-Solar. It was not possible to infer the input uncertainties for the other WRF-Solar modules that include atmospheric profiles using only the first method; thus, we adopted the three methodologies together, in which the uncertainties of the input variables can be estimated across vertical layers. Although more sophisticated and objective methods could be applied to infer the representative value of errors for the input variables, we chose basic methods because of the simplicity of their application because of the limited availability of observations that can be used to estimate the uncertainties in the input variables.

3.1.3 Identification of Key Variables from Six WRF-Solar Modules

3.1.3.1 Fast All-Sky Radiation Model for Solar Applications

The impact of the uncertainty of the input variables on the output variables was analyzed for the six WRF-Solar modules independently. For FARMS, the uncertainty of GHI and direct normal irradiance (DNI) was analyzed with respect to the uncertainties in seven input variables for clear-sky and six input variables for cloudy-sky conditions, respectively (**Figure 5**). In clear-sky conditions, GHI was highly sensitive to uncertainties in surface albedo (albdo), AOD, total precipitable water (w), and aerosol asymmetry factor (g), and it was less sensitive to uncertainty in surface pressure (p) (**Figure 5a**). The uncertainty in surface albedo produced the highest positive uncertainties across all scenarios for GHI under clear-sky conditions because an increase in surface albedo increases the magnitude of the backscattered radiation from the aerosols to the land surface. For DNI, all cases of AOD and Ångström wavelength exponent (alpha) produced negative uncertainties, indicating that an increase in the magnitude of the variables leads to a decrease in DNI. Under cloudy-sky conditions, GHI exhibited its notable uncertainties regarding uncertainties in the variables of cloud optical depth (e.g., qc and qs); this is because of the

transmittances of the cloud for direct incident radiation/direct outgoing radiation and direct incident radiation/diffuse outgoing radiation, which are mainly governed by cloud optical depth (**Figure 5b**), whereas DNI brings its uncertainties near zero for cloud optical depth and cloud effective radius (re_qc, re_qi, and re_qs). The small uncertainty of DNI to uncertainty in cloud optical depth occurred because nearly all DNI is attenuated for most clouds and changes in cloud optical depth can no longer influence changes is DNI. In the case of cloud effective radius, the same holds true because in most cases, the cloud is sufficiently optically thick to scatter all direct radiation irrespective of the size of the cloud particles.

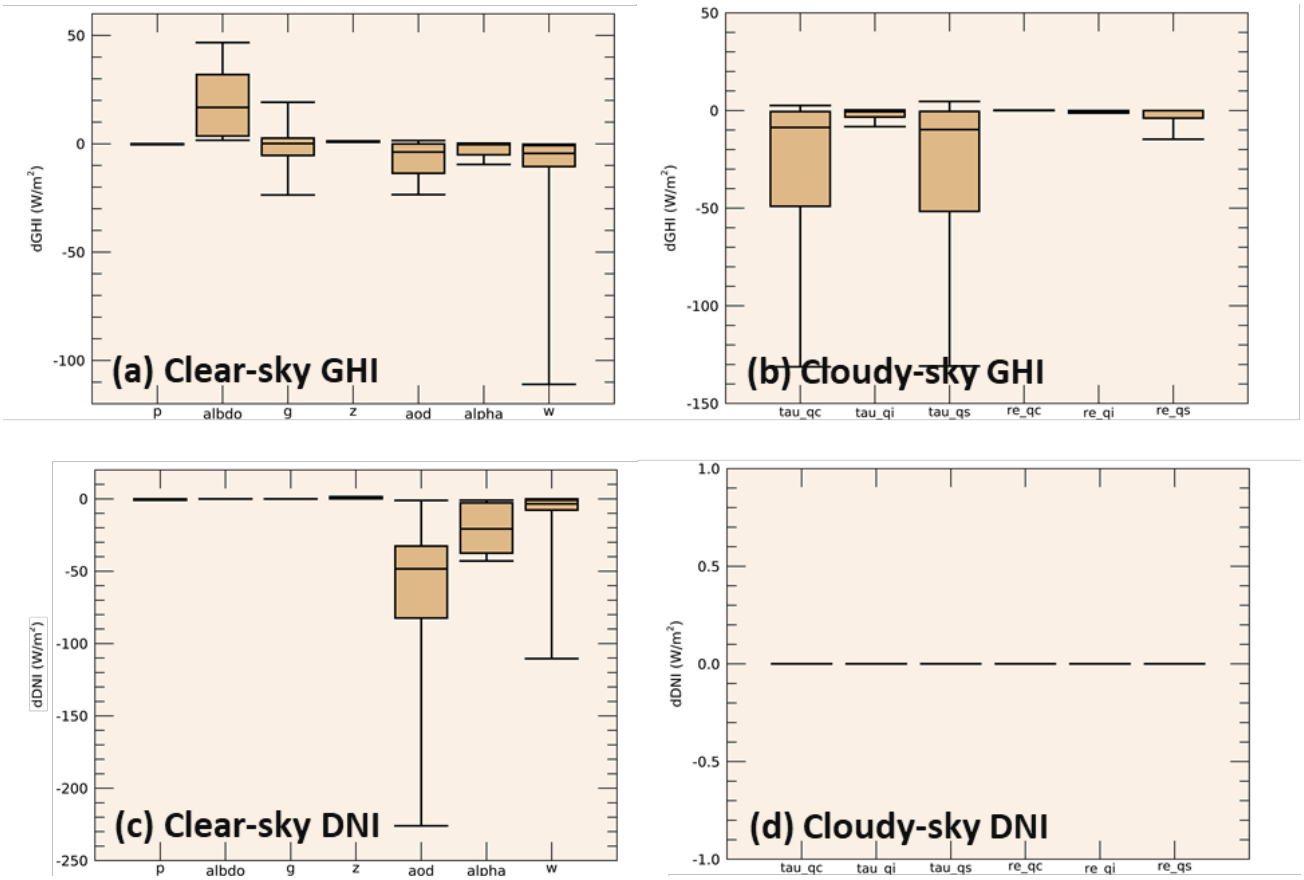

Figure 5. Uncertainty in (a), (b) GHI and (c), (d) DNI with respect to uncertainty in the main input variables for FARMS under clear-sky and cloudy-sky conditions. The $\mathbf{d(Variable)}$ in the vertical axis represents Y_U in Eq. 3.4. The Inner box indicates the lower quartile, the median, and the upper quartile of data; and the lower and upper bars represent the lower 10% and the upper 90% of the data, respectively.

3.1.3.2 Thompson Microphysics

The analysis of sensitivity of the Thompson microphysics to input variable uncertainty was performed using 6,480 input vectors from a 1-day WRF-simulation (see Section 3.1.2). We focused on the output variables associated with the cloud formation and dissipation. In particular, we analyzed uncertainties of the six vertical profiles of cloud mixing ratio and effective particle size for liquid water, ice, and snow with respect to uncertainties in 11 input variables (**Figure 6**). The mixing ratio (QC) and effective radius (RE_QC) of cloud water was sensitive to

uncertainties in the amount of water vapor (qv), temperature (th), Exner pressure (pii $= \left(\frac{p}{p_0}\right)^{\frac{R_d}{c_p}} = \frac{T}{\theta}$), and pressure (p). The cloud ice mixing ratio (QI), effective radius (RE_QI), and number concentration (not shown) were also sensitive to uncertainties in water vapor and temperature. For effective radii for water and ice, the negative uncertainty for the temperature denotes that cloud condensation decreases with increasing temperature. In addition, the cloud ice number concentration (ni) had negative uncertainties across all cases for cloud ice mixing ratio. This means that as ice number concentration decreases, the effective size of ice increases. The uncertainty in the effective radius of snow (RE_QS) was highly sensitive to the uncertainty in the snow mixing ratio (QS). Most hydrometeor mixing ratios tend to be more sensitive to their own values than to others.

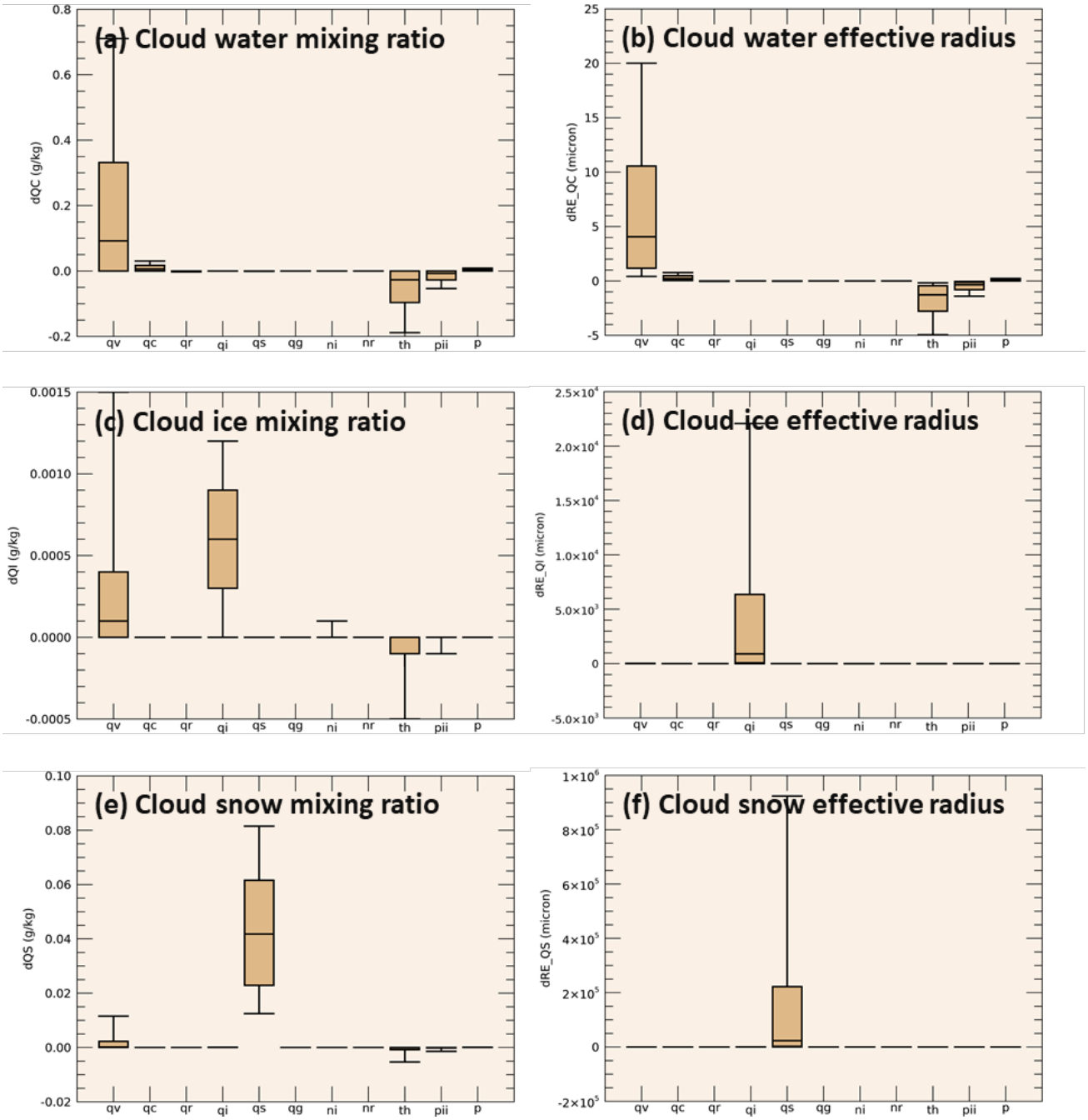

Figure 6. Same as Figure 5 but for uncertainty in (a), (c), (e) mixing ratio and (b), (d), (f) effective radius of cloud with respect to uncertainties in the main input variables for the Thompson microphysics scheme

3.1.3.3 Mellor–Yamada–Nakanishi–Niino Planetary Boundary Layer

Figure 7 shows the uncertainty results for the sensitivity analysis of the MYNN-PBL scheme. Four output variables of the MYNN-PBL related to boundary layer clouds, which dominate uncertainties in predicting solar irradiance, were examined: cloud water (QC_BL) and cloud fraction (CLD_FRA) from the boundary layer, tendency variables for temperature (TH tendency), and water vapor (QV tendency). The key input variables responsible for the largest

uncertainties in predicting cloud water and cloud fraction are air temperature (th) and water vapor mixing ratio (qv). Uncertainties in the tendencies of temperature and water vapor were sensitive to uncertainties in the air density (rho) and turbulent kinetic energy (qke), respectively.

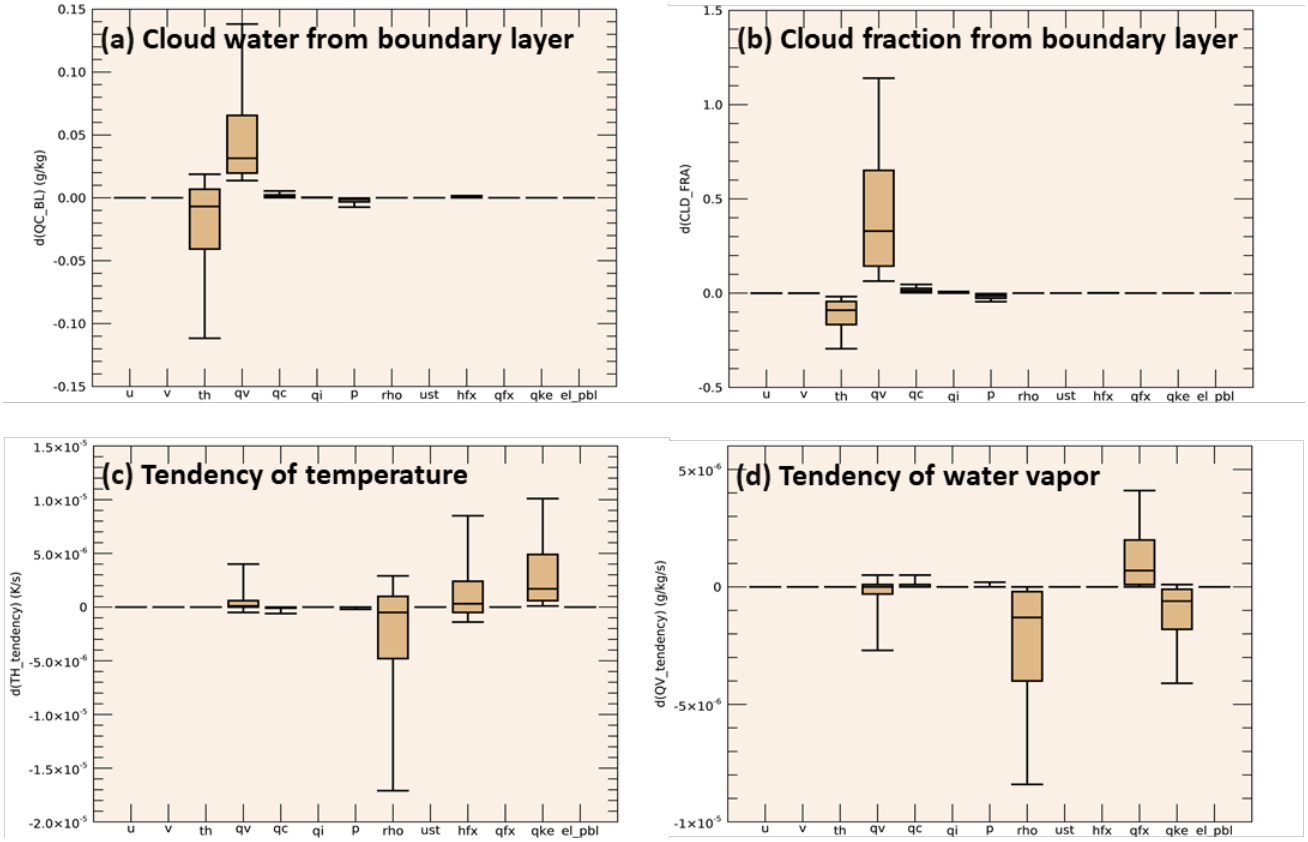

Figure 7. Same as Figure 5 but for uncertainty in (a) cloud water from the boundary layer, (b) cloud fraction from the boundary layer, (c) tendency of temperature, and (d) tendency of water vapor with respect to uncertainties in the main input variables for the MYNN-PBL scheme

3.1.3.4 Deng Shallow Cumulus System

The analysis of the sensitivity of the Deng shallow cumulus scheme was performed to identify the input variables that cause the largest uncertainties in three output variables: effective cloud fraction for radiation (ca_rad), effective cloud water for radiation (cw_rad), and tendency of water vapor (rqvshten). Note that the "effective" cloud fraction proposed by Deng, Seaman, and Kain (2003) represents the net effect of subgrid clouds on radiation; the effective cloud water is calculated with the sum of the grid-averaged condensed water content and the resolved scale of cloud water mixing ratio; and the tendency of water vapor is estimated by feedback of the convective tendency to the resolvable-scale cloud in the Deng shallow cumulus scheme. **Figure 8** shows the uncertainty results calculated with all cases from the 1-day WRF simulation for the three output variables. This confirms that temperature (t) and two mixing ratio variables of water vapor (qv) and cloud water (qc) had a relatively large width distribution compared with the other variables for effective cloud fraction for radiation. The uncertainty of the cloud water mixing ratio produced the highest impact on the effective cloud water for radiation. The uncertainty of the tendency of water vapor was found to be sensitive to uncertainties in vertical velocity (w) as well as to water vapor mixing ratio (qv).

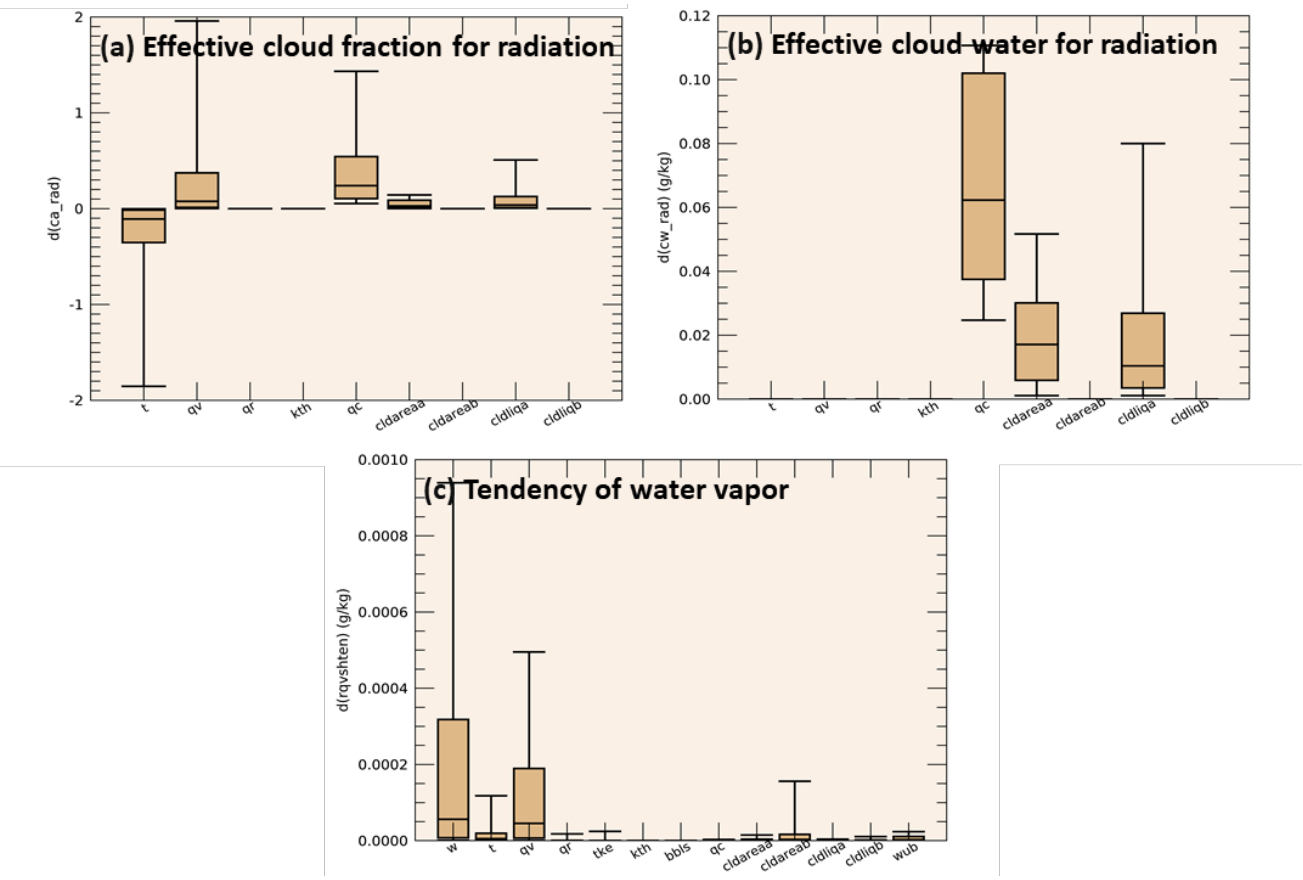

Figure 8. Same as Figure 5 but for uncertainty in (a) effective cloud fraction for radiation, (b) effective cloud water for radiation, and (c) tendency of water vapor with respect to uncertainty in the main input variables for the Deng shallow cumulus scheme

3.1.3.5 CLD3

The CLD3 scheme was designed to capture unresolved clouds based on the temperature and moisture profiles of each grid. It was also analyzed to identify the input variables responsible for the largest uncertainties in predicting subgrid-scale cloud fraction (CLDFRA), cloud water mixing ratio (QC), and cloud ice mixing ratio (QI). The analysis showed similar results from the Deng shallow cumulus scheme because subgrid-scale clouds are predominantly controlled by moisture and temperature. It is evident that uncertainties in the selected output variables of CLD3 are sensitive to uncertainties in water vapor mixing ratio (qv) and temperature (t) (**Figure 9**).

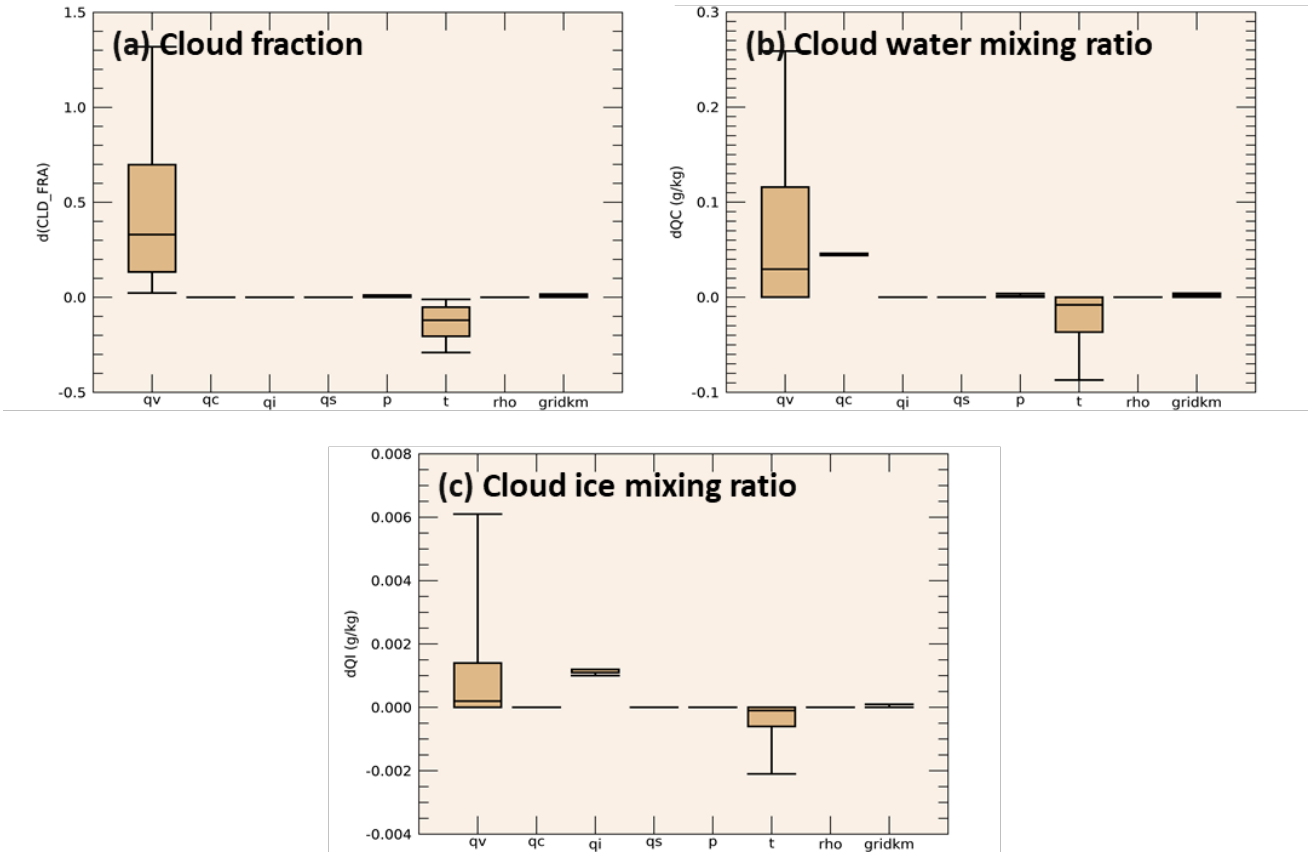

Figure 9. Same as Figure 5 but for uncertainty in (a) cloud fraction, (b) cloud water mixing ratio, and (c) cloud ice mixing ratio with respect to uncertainties in the main input variables for the CLD3 unresolved cloud fraction scheme

3.1.3.6 Noah Land Surface Model

The sensitivity analysis of the Noah LSM was conducted for sensible heat flux (HFX) and latent heat flux (LH), which influence cloud formation and evolution by the land surface interactions. The goal was to identify the input variables that caused the largest uncertainties in the surface fluxes. In **Figure 10**, uncertainties in temperature variables (T3D and TSLB, temperature at first layer and soil temperature) exhibit high impact across all scenarios on uncertainties in sensible heat flux, which is an expected outcome of the sensitivity test. The soil moisture (SMOIS) and water vapor mixing ratio (QV3D) were confirmed as important variables that cause high uncertainties to the latent heat flux. In the Noah LSM scheme, the latent heat flux is calculated as a function of the direct soil evaporation, canopy water evaporation, total plant transpiration, and sublimation from snowpack. The soil moisture and water vapor mixing ratio predominantly affect the change in the direct soil evaporation and are thus applicable to the stochastic perturbations of input variables in the Noah LSM.

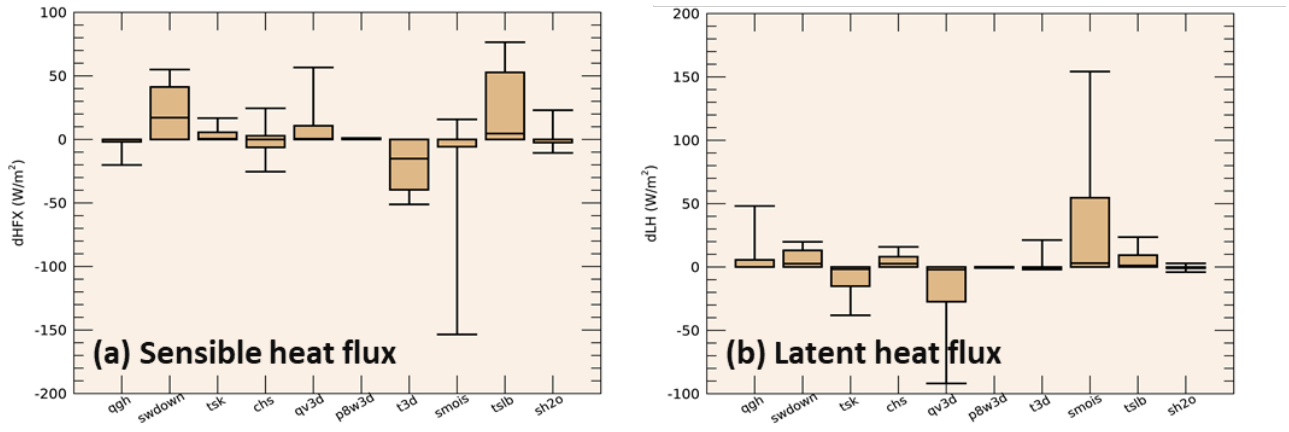

Figure 10. Same as Figure 5 but for uncertainty in (a) sensible heat flux and (b) latent heat flux with respect to uncertainties in the main input variables for the Noah LSM scheme

3.2 Development of WRF-Solar Capabilities to Enable Perturbation of Variables

3.2.1 Variable Selection to Perturb

Variables to perturb are selected based on our sensitivity analysis for the six WRF-Solar modules. **Table 3** shows 14 selected variables and the locations where they will be perturbed inside the six modules. Perturbation types can be controlled in two ways, with the first one assigning an absolute value and the second using a relative percentage of the variable value. Perturbations of relative percentage are applied to the first trial.

Table 3. Selected Variables to Perturb in the Six WRF-Solar Modules

#	Variable	Name in Code	Location	Perturb Type
1	Albedo	ALBEDO	Inside FARMS	%
2	Aerosol optical depth	AOD5502D	Inside FARMS	%
3	Angstrom wavelength exponent	Angexp2d	Inside FARMS	%
4	Asymmetry factor	Aerasy2d	Inside FARMS	%
5	Water vapor mixing ratio	QVAPOR	Inside FARMS, MYNN, Thompson, Noah, Deng, and Icloud3	%
6	Cloud water mixing ratio	QCLOUD	Inside FARMS, MYNN, Thompson, and Deng	%
7	Ice mixing ratio	QICE	Inside Thompson	%
8	Snow mixing ratio	QSNOW	Inside FARMS and Thompson	%
9	Ice number concentration	NI	Inside Thompson	%
10	Potential temperature	Theta	Inside MYNN, Noah, Deng, and Icloud3	%
11	Turbulent kinetic energy	QKE	Inside MYNN	%
12	Soil moisture content	SMOIS	Inside Noah	%
13	Soil temperature	TSLB	Inside Noah	%
14	Vertical velocity	W	Inside Deng	%

3.2.2 Stochastic Perturbations

We specify the characteristics of the stochastic perturbations for each variable using a text file (Kim et al. 2020). We have updated WRF-Solar to generate multiple stochastic perturbations according to this text file, and the perturbations are stored in the array pert3d(i,k,j,n). The perturbations in pert3d are linked to the six WRF-Solar modules, which are the FARMS radiation scheme, the Thompson cloud microphysics scheme, the Noah LSM scheme, the MYNN-PBL scheme, the Deng shallow cumulus scheme, and the CLD3 unresolved cloud fraction scheme, respectively.

Our strategy for introducing stochastic perturbations is summarized in **Table 4**. Standard deviation (Std) indicates the size of the perturbation. This number is a relative percentage of each value of the variable. Lambda and Tau are the length scale in meters and the timescale in seconds of each perturbation, respectively. Considering random perturbations as a Gaussian distribution, Cut_off number 3 means that 3% of the edges are excluded. The seed controls which random numbers to start with. Vert_s provides information on the variable dimension. Vert_s number 0 or 1 means that the dimension of each variable is 2 or 3, respectively.

Table 4. Default Settings for Adding Stochastic Perturbations to WRF-Solar

#	Variable	Std	Lambda (m)	Tau (s)	Cut_off	Seed	Vert_s
1	ALBEDO	0.10	100000.0	86400.0	3.0	17	0
2	AOD5502D	0.25	100000.0	3600.0	3.0	18	0
3	Angexp2d	0.10	100000.0	3600.0	3.0	19	0
4	Aerasy2d	0.05	100000.0	3600.0	3.0	20	0
5	QVAPOR	0.05	100000.0	3600.0	3.0	21	1
6	QCLOUD	0.10	100000.0	3600.0	3.0	22	1
7	QICE	0.10	100000.0	3600.0	3.0	23	1
8	QSNOW	0.10	100000.0	3600.0	3.0	24	1
9	NI	0.05	100000.0	3600.0	3.0	25	1
10	Theta	0.001	100000.0	3600.0	3.0	26	1
11	QKE	0.05	80000.0	600.0	3.0	27	1
12	SMOIS	0.10	80000.0	21600.0	3.0	28	1
13	TSLB	0.001	80000.0	21600.0	3.0	29	1
14	W	0.10	80000.0	21600.0	3.0	30	1

Figure 11 shows the distribution of the perturbations for two variables, which are AOD and turbulent kinetic energy. We can check the perturbation length scales and sizes from this example. The standard deviation of the perturbation for the AOD is 0.25. It indicates that a maximum of 25% of the AOD can be added to or subtracted from the original value. The length scale of the AOD is 100 km and that of the turbulent kinetic energy is 80 km. The timescale of the AOD is 1 hour, and that of the turbulent kinetic energy is 10 minutes. It means that perturbations are implemented more frequently for turbulent kinetic energy.

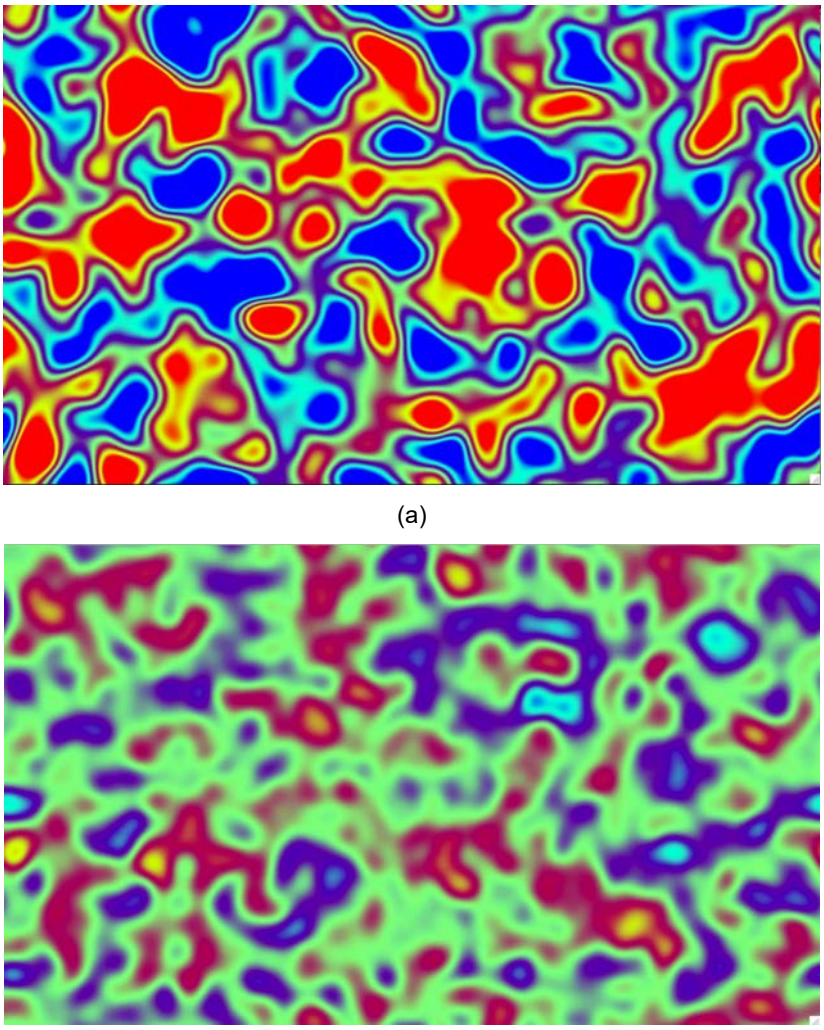

(a)

(b)

Figure 11. Distributions of perturbations for (a) AOD and (b) turbulent kinetic energy

3.2.3 Test of Stochastic Perturbation to Generate Ensemble Members from the Fast All-Sky Radiation Model for Solar Applications

The stochastic perturbations for seven variables—ALBEDO, AOD5502D, Angexp2d, Aerasy2d, QVAPOR, QCLOUD, and QSNOW—were implemented in the FARMS scheme. We ran two WRF-Solar simulations, one without perturbations and the other with perturbations, to see if the implemented perturbations work as expected. Simulated GHI were compared to SURFRAD observations, and results show that the GHI simulation with perturbations better match the GHI observation than the simulation without perturbations, especially for cloudy time periods (**Figure 12 and Figure 13**).

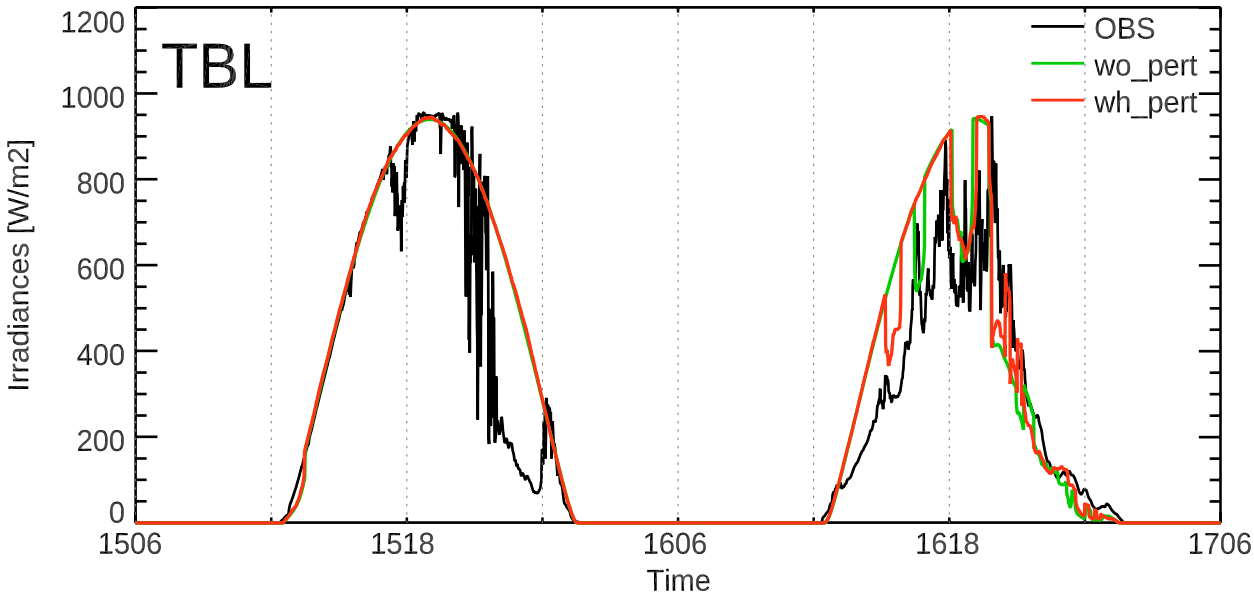

Figure 12. Time series of observed and simulated GHI at the TBL SURFRAD site in Boulder, Colorado (40.13°N, 105.24°W). The green and red lines indicate the WRF-Solar simulations without and with perturbations, respectively.

Figure 13 shows the simulated GHI distribution and differences when perturbations were added to the FARMS radiation scheme on 15 UTC April 16, 2018, over the CONUS domain. The difference in GHI tends to increase significantly in cloudy areas near noon.

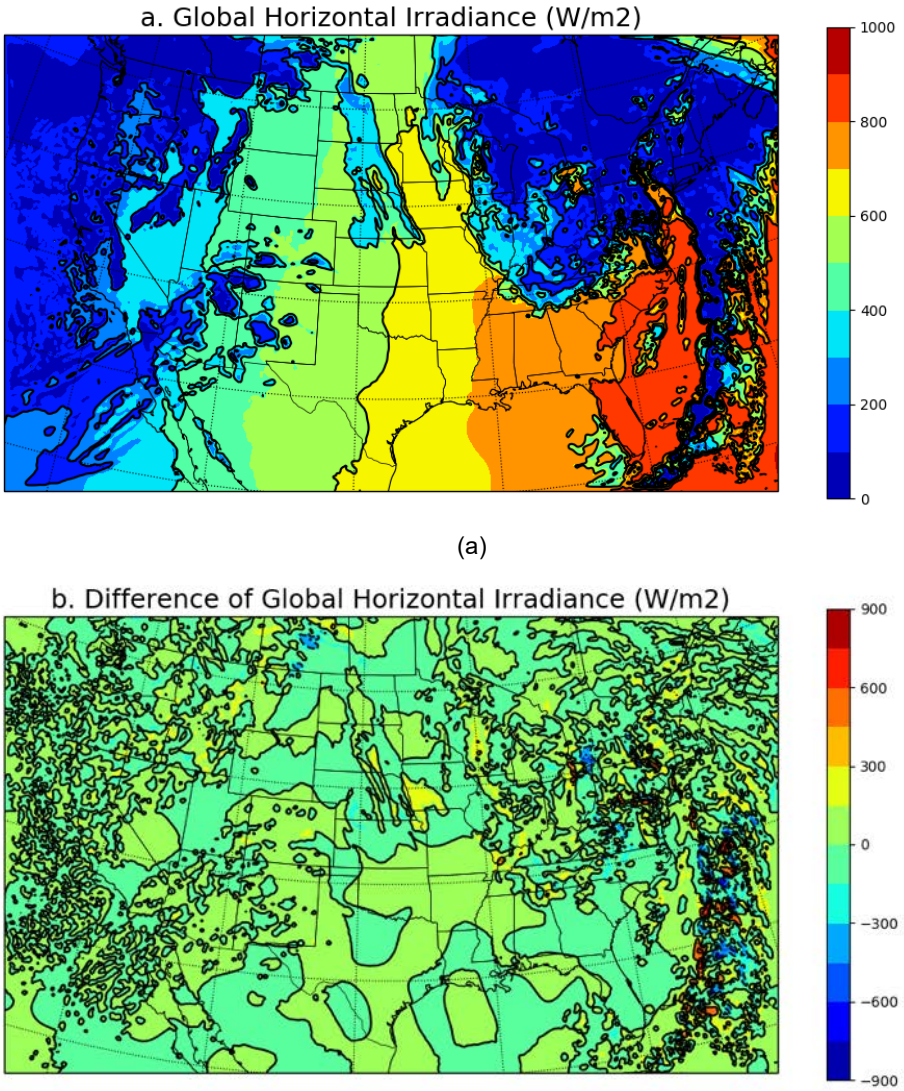

Figure 13. (a) Simulated GHI distribution on 15 UTC April 16, 2018, and (b) differences in GHI simulations without and with perturbations (GHI_wh_pert – GHI_wo_pert)

Five ensemble members of WRF-Solar were tested in a preliminary version of the WRF-Solar ensemble system, and simulated GHI were compared to the TBL SURFRAD site (Boulder, Colorado) observations (**Figure 14**). The simulation time is from 06 UTC April 15, 2018, to 06 UTC April 17, 2018. Results show that the impact of perturbations on five ensemble members was more pronounced in cloudy conditions.

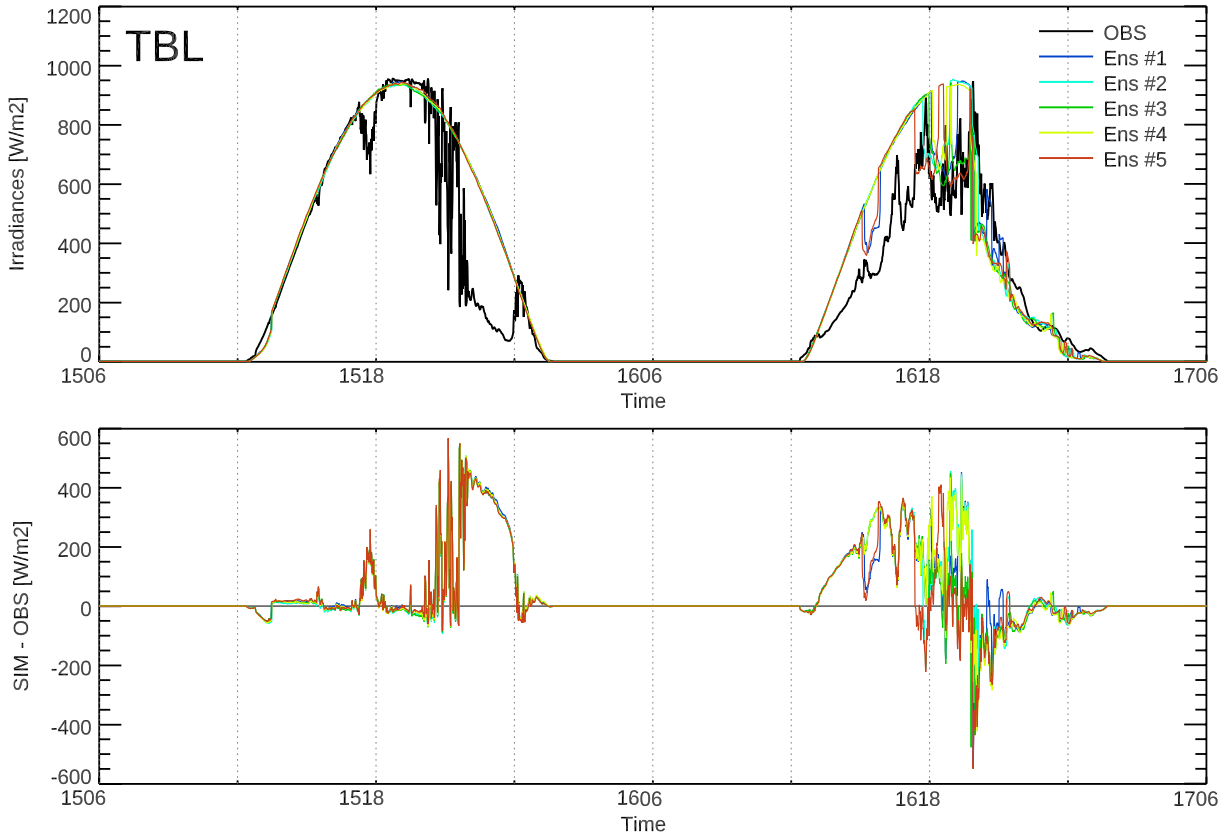

Figure 14. Observed and simulated GHI from the five ensemble members of WRF-Solar at the TBL SURFRAD site in Boulder, Colorado (40.13°N, 105.24°W) from 06 UTC April 15, 2018, to 06 UTC April 17, 2018

3.2.4 Implementation of Stochastic Perturbations for Six WRF-Solar Modules

The stochastic perturbations for seven variables—albedo, AOD (AOD5502D), angstrom wavelength exponent (Angexp2d), asymmetry factor (Aerasy2d), water vapor (QVAPOR), cloud water (QCLOUD), and snow (QSNOW)—were implemented for the FARMS scheme. We implemented a perturbation of a single variable in the WRF-Solar model and ran five ensembles to confirm that the perturbations work as expected. All the steps were repeated for every variable, and then we implemented seven perturbations together at the end.

The NSRDB observations are used for the validation of the WRF-Solar forecast results. The next subsection (Section 3.2.5) provides a verification of the satellite-derived data with SURFRAD observations.

Differences in the ensemble mean to the NSRDB ($\sqrt{(\bar{f} - obs)^2}$) observations were calculated to estimate the model forecast error compared to observations for the five ensemble runs. **Figure 15a** shows those differences for the experiment that added perturbations to all the selected variables from the FARMS scheme at a specific forecast time (1530 UTC April 16, 2018). Standard deviations for the five ensemble forecasts ($\sqrt{\frac{1}{N-1}\sum_{i=1}^{N}(f_i - \bar{f})^2}$) were also calculated to estimate the ensemble spread. **Figure 15b** displays these scores.

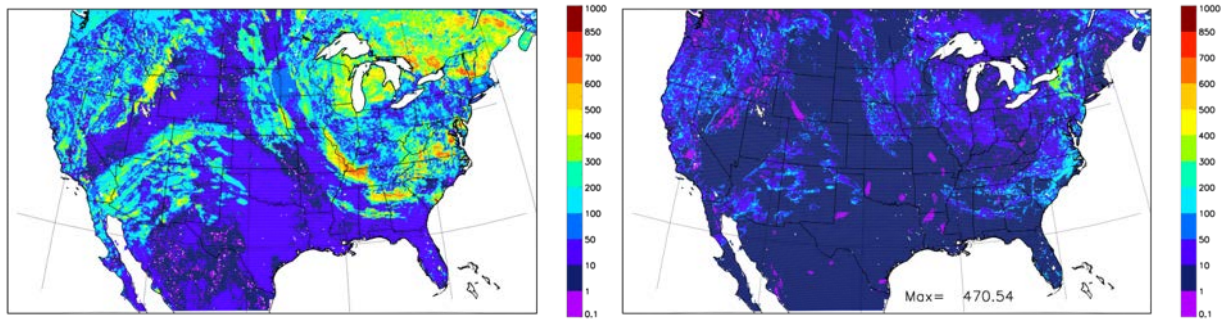

(a) (b)

Figure 15. (a) Differences in the ensemble mean to the NSRDB and (b) standard deviations for five ensemble forecasts on 1530 UTC April 16, 2018, when perturbations are added to the FARMS scheme

Stochastic perturbations were added to four variables in the Deng scheme: water vapor, cloud water, temperature (Theta), and vertical wind (W). The development process followed the same steps as the FARMS's development. The differences in the ensemble means and the standard deviations of the five ensembles were also compared to the NSRDB (**Figure 16**).

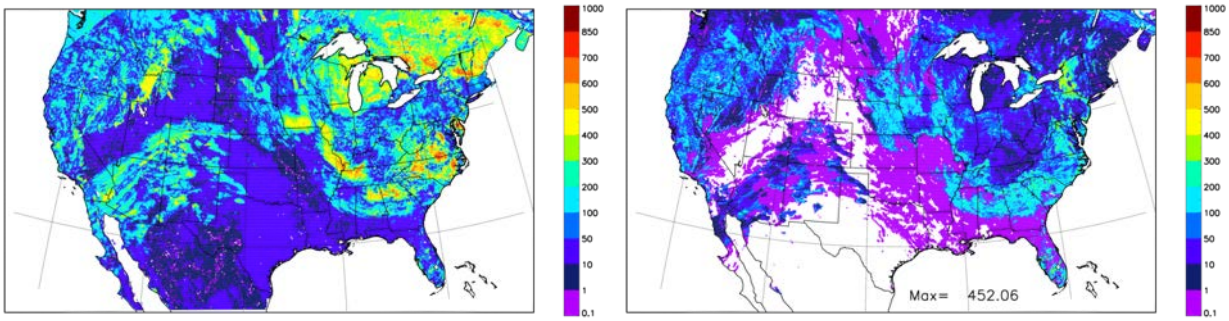

(a) (b)

Figure 16. Same as Figure 15 except perturbations are added to the Deng shallow cumulus scheme

Stochastic perturbations were added to four variables in the MYNN PBL scheme: water vapor, cloud water, temperature (Theta), and turbulent kinetic energy (qke). Again, the development process followed same steps as the FARMS's development. The differences in the ensemble means and the standard deviations of the five ensembles were compared to the NSRDB observations (**Figure 17**).

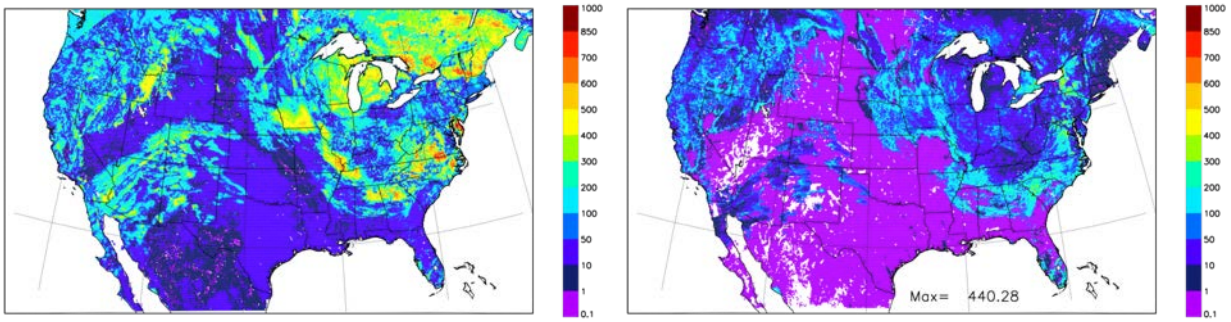

(a) (b)

Figure 17. Same as Figure 15 except perturbations are added to the MYNN PBL scheme

Stochastic perturbations were added to four variables in the Noah LSM scheme: water vapor, temperature (Theta), soil moisture (SMOIS), and soil temperature (TSLB). The development process followed the same steps as the FARMS's development. The differences in the ensemble means and the standard deviations of the five ensembles were compared to the NSRDB observations (**Figure 18**).

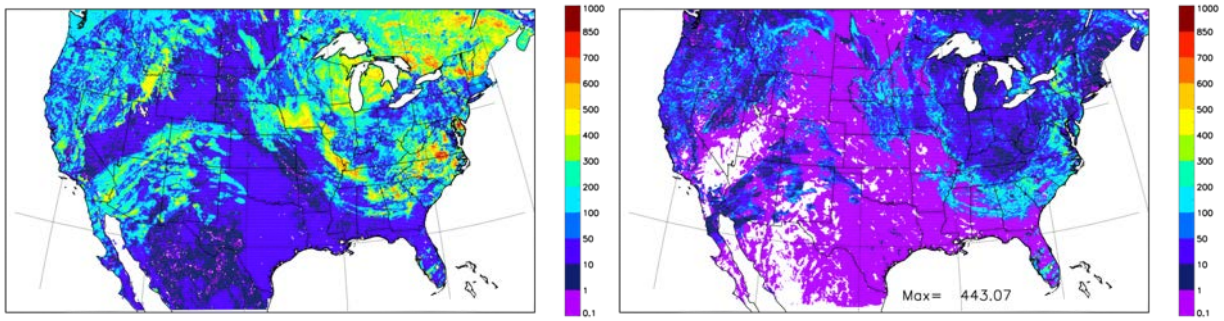

(a) (b)

Figure 18. Same as Figure 15 except perturbations are added to the Noah land surface scheme

Stochastic perturbations were added to five variables in the Thompson microphysics scheme: water vapor, cloud water, cloud ice (QICE), snow (QSNOW), and ice number concentration (Ni). The development process followed the same steps as the FARMS's development. The differences in the ensemble means and the standard deviations of the five ensembles were compared to the NSRDB observations (**Figure 19**).

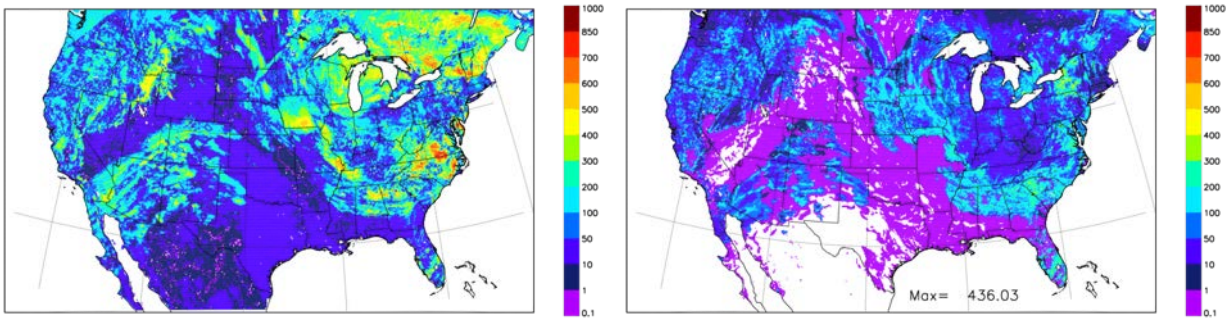

(a) (b)

Figure 19. Same as Figure 15 except perturbations are added to the Thompson microphysics scheme

Stochastic perturbations were added to two variables in the CLD3 scheme: water vapor and temperature. The development process followed the same steps as the FARMS's development. The differences in the ensemble means to the observations and standard deviations of the five ensembles were compared to the NSRDB observations (**Figure 20**).

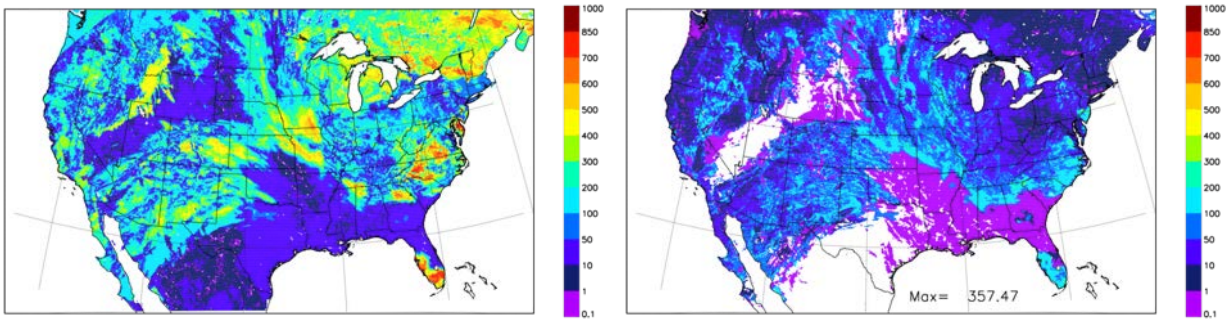

(a) (b)

Figure 20. Same as Figure 15 except perturbations are added to the CLD3 sub-grid cloud scheme

Finally, stochastic perturbations were added to all 14 variables in the six WRF-Solar physics modules. The development process followed the same steps as the FARMS's development. The differences in the ensemble means to the observations and standard deviations of the five ensembles were also compared to the development of adding perturbations to all schemes (**Figure 21**).

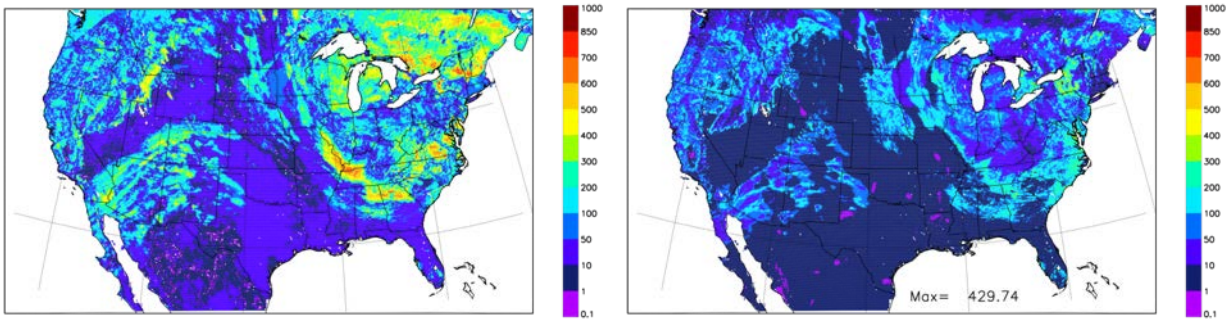

(a) (b)

Figure 21. Same as Figure 15 except perturbations are added to all of six physics schemes

3.2.5 Validation of National Solar Radiation Database for Ensemble Evaluation

The NSRDB is a satellite-based solar radiation database of observations (Sengupta et al. 2018). This is a public data set that has been created for the last 21 (1998–2018) years and provides GHI and DNI at a 4-km horizontal resolution at 30-minute intervals for the CONUS region. These data show good agreement with surface observations, with mean percentage biases within 5% and 10% for GHI and DNI, respectively. The NSRDB observations were interpolated to the 9-km WRF-Solar grid resolution to validate the forecast results.

Figure 22 shows a comparison of GHI observations from the NSRDB and SURFRAD and the forecast results of WRF-Solar_V1 during 06 UTC April 15, 2018, to 06 UTC April 17, 2018, at seven SURFRAD sites. The two observational data sets generally show good agreement for this case. The difference between the NSRDB and SURFRAD is significantly smaller than the bias of the WRF-Solar forecast, which indicates that the NSRDB observation can be used for the model evaluation. When we look at the BON (Bondville, Illinois) and PSU (Pennsylvania State, Pennsylvania) sites (**figures 22b and 22f**), those locations are cloudy for both days. For cloudy conditions, it is observed that the NSRDB and SURFRAD observations agree well. The WRF-Solar GHI forecast was significantly underestimated in the SXF (Sioux Falls, South Dakota) region because the model predicts a larger area of thick cloudy conditions than the observations (**Figure 22d**). **Figure 22f** also shows that the WRF-Solar_V1 forecast overpredicts the cloud optical thickness but captures the cloud timing well.

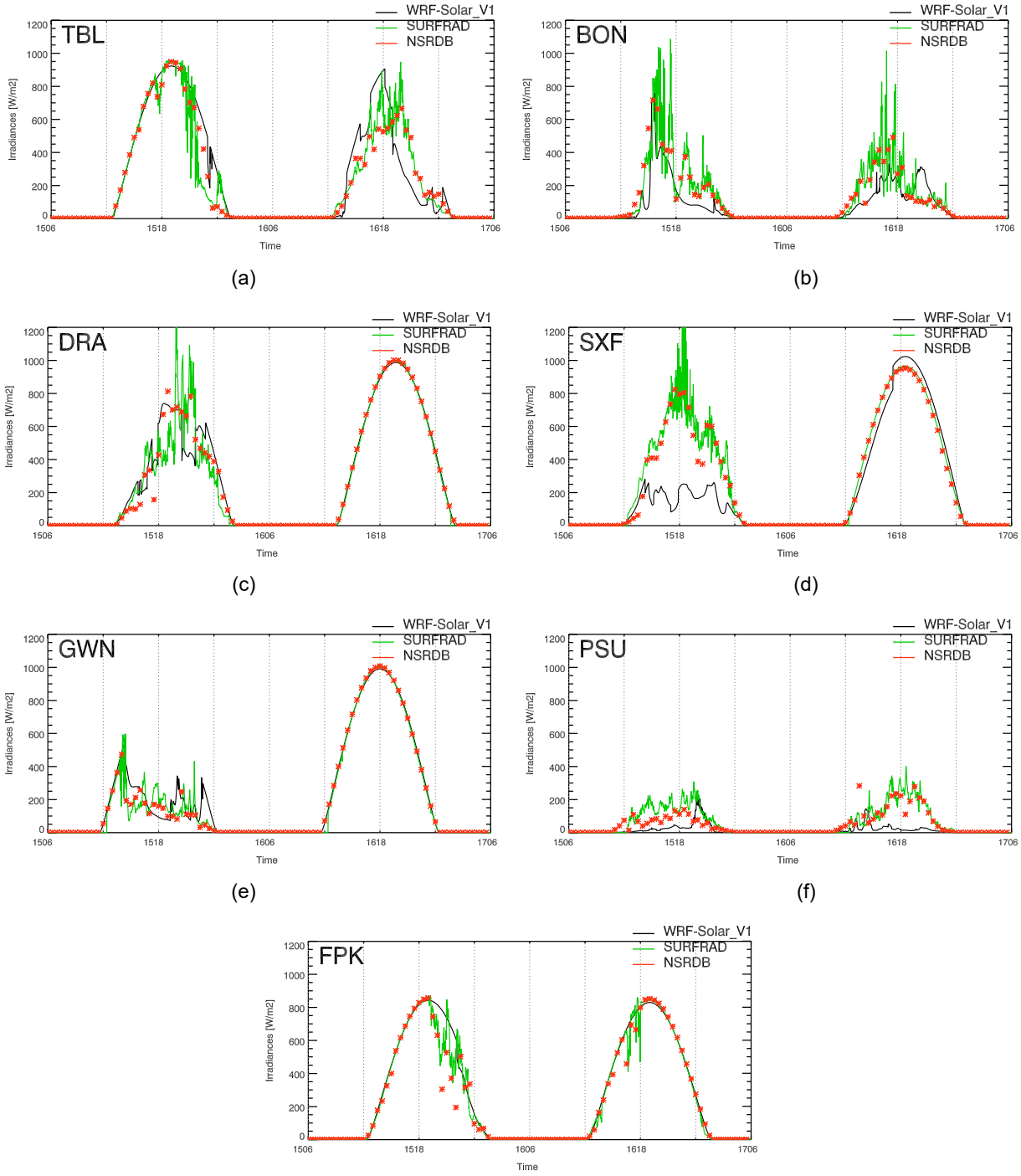

Figure 22. Time series of GHI observations from SURFRAD and the NSRDB and GHI forecasts from WRF-Solar_V1 during 06 UTC April 15, 2018, to 06 UTC April 17, 2018, at seven SURFRAD sites

3.2.6 WRF-Solar Ensemble Forecast Result

3.2.6.1 Result for One-Day-Ahead Forecast

The WRF-Solar ensemble forecast using 10 ensembles was run from 06 UTC April 15, 2018, to 06 UTC April 17, 2018. **Figure 23** compares the forecasted GHI and SURFRAD observations at the TBL site. The 10 ensemble members show different GHI distributions, and the impact of the stochastic perturbations was more pronounced in cloudy conditions.

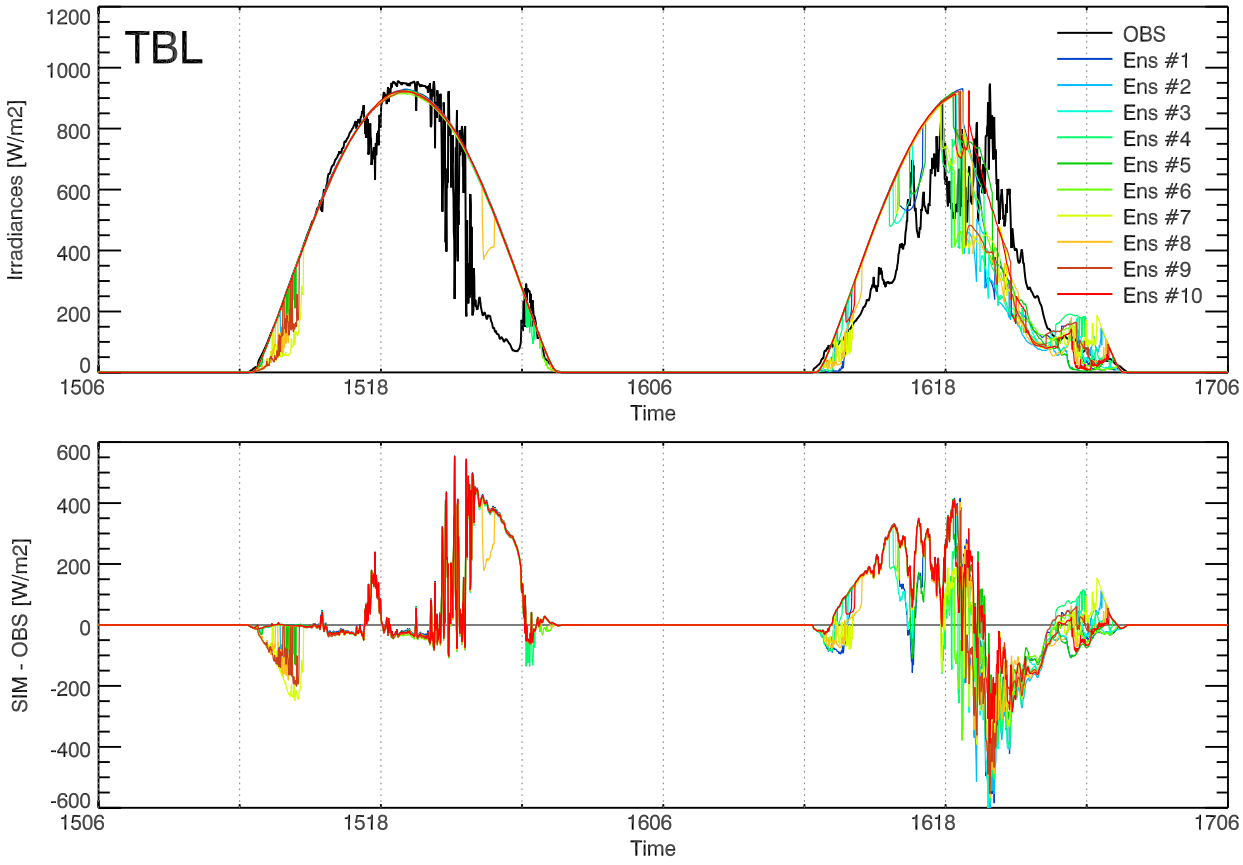

Figure 23. Observed and simulated GHI from the 10 ensemble members of WRF-Solar at the TBL SURFRAD site in Boulder, Colorado (40.13°N, 105.24°W) from 06 UTC April 15, 2018, to 06 UTC April 17, 2018

Figure 24 compares the GHI forecasts from WRF-Solar_V1 and WRF-Solar ensemble forecasts against NSRDB observations on 1530 UTC April 16, 2018. The WRF-Solar forecast tends to produce more clouds than the observations. The results are promising because cloud distributions from the WRF-Solar ensemble move closer to the observations by reducing some of the clouds.

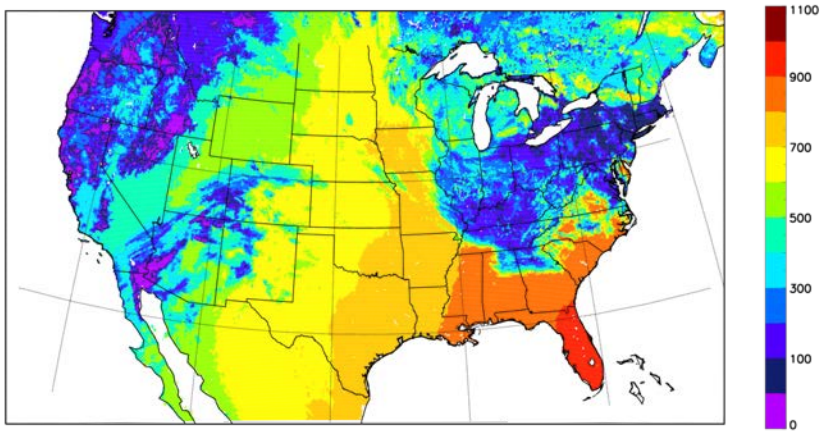

(a) NSRDB (W/m^2)

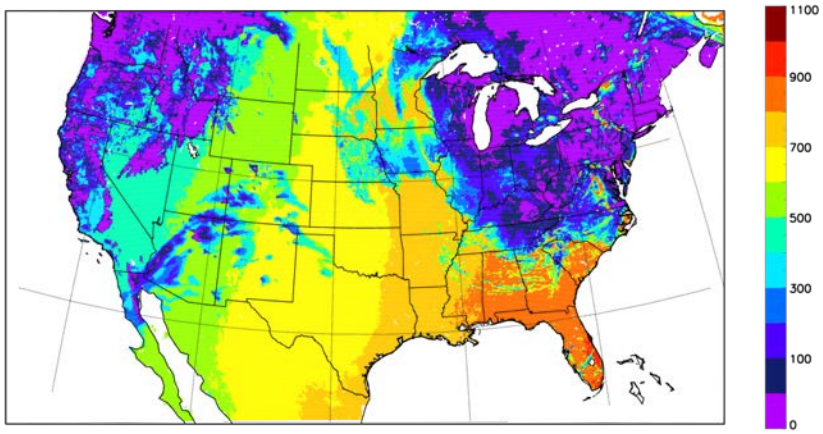

(b) WRF-Solar_V1 (W/m^2)

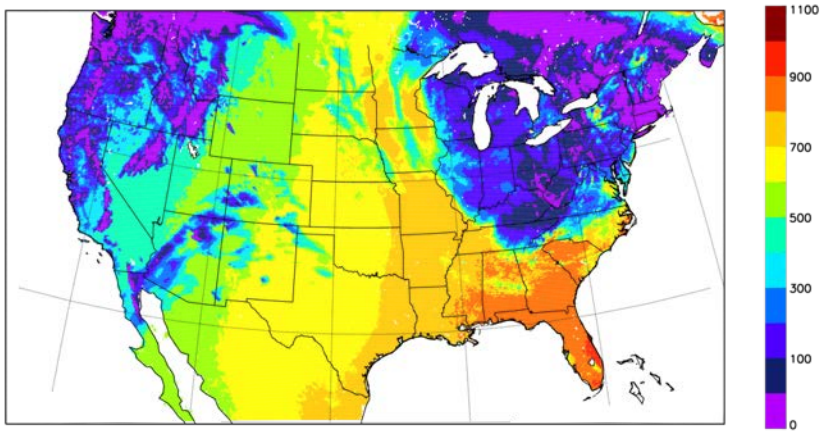

(c) WRF-Solar_Ensemble (W/m^2)

Figure 24. (a) GHI observations on 1530 UTC April 16, 2018, and predicted GHI from the (b) WRF-Solar_V1 and (c) WRF-Solar ensembles

3.2.6.2 Results for Seven Sets of Day-Ahead Forecasts Sampled from April 2018

The forecast skills of each member of the WRF-Solar stochastic ensemble were investigated using the NSRDB for April 2018. Forty-eight-hour forecasts had been performed every 4 days during April 2018 (seven samples) initialized at every 06 UTC.

Figure 25 shows the bias and MAE for WRF-Solar Version 1 (V1), WRF-Solar V1 with coupling FARMS (couple_farms = true), and 10 stochastic ensemble members. It shows that coupling of FARMS GHI to the Noah land surface model has a positive impact on the GHI forecast. Ten ensembles show a similar bias and MAE during the forecast hours, and the bias and MAE are less than WRF-Solar. The perturbations in five physics schemes seem to play a positive role in the GHI predictions.

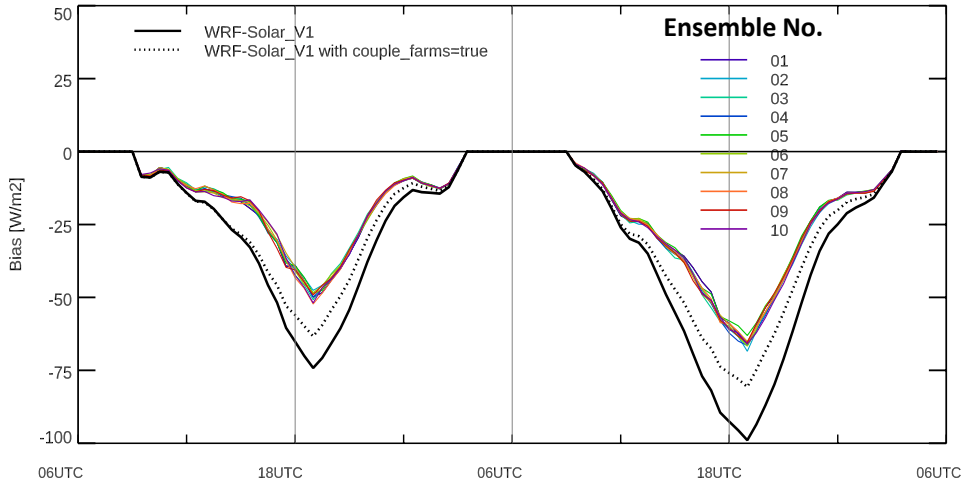

(a)

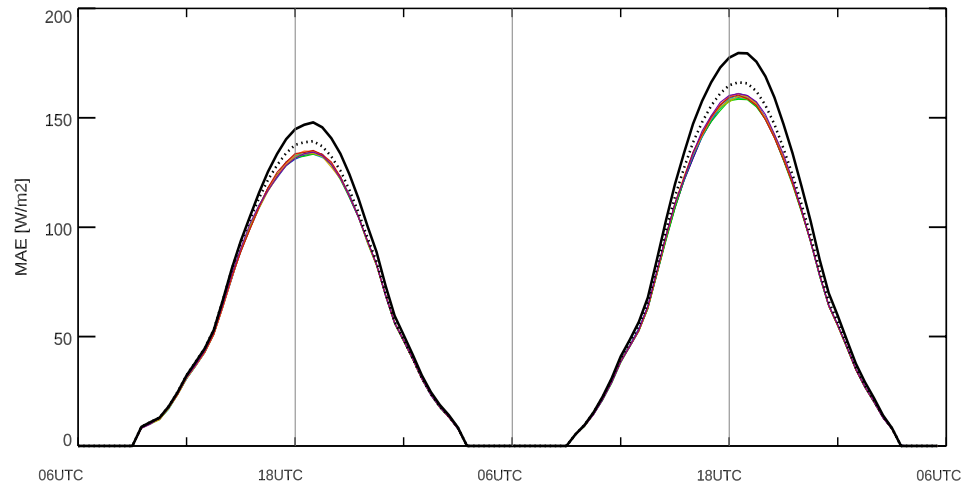

(b)

Figure 25. (a) Bias and (b) MAE of the GHI calculated with the 10 WRF-Solar stochastic ensemble forecasts and WRF-Solar V1 over the CONUS domain for the April 2018 NSRDB observations

3.2.6.3 Analysis of Stochastic Ensemble Using Different Ensemble Sizes

Three different numbers of stochastic ensembles are tested and evaluated in terms of root meant square error (RMSE), spread, bias, rank histogram, and continuous rank probability score.

Forty-eight-hour forecasts were performed for every day during April 2018 (30 samples) initialized at every 06 UTC. The forecast results of the second day are evaluated using 7 NSRDB observations. When using 20 ensemble members, the RMSE, spread, and bias scores are slightly better, but the results are generally similar as when using 10 or 5 ensemble members (**figures 26, 27, and 28**).

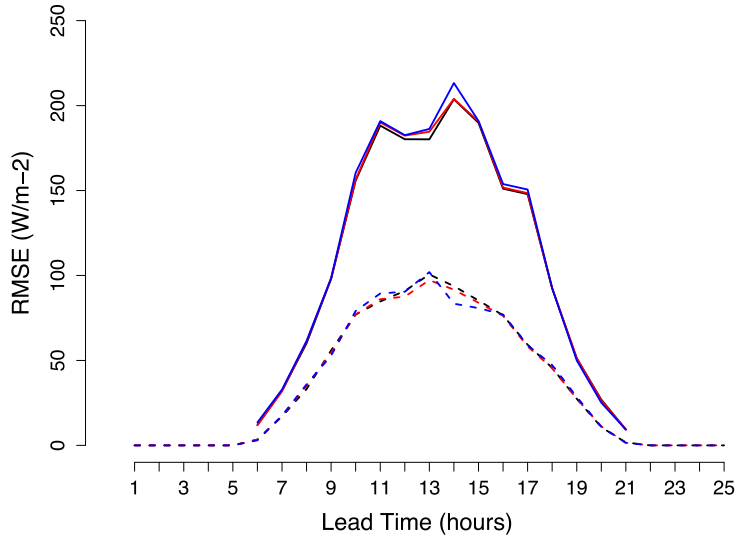

(a)

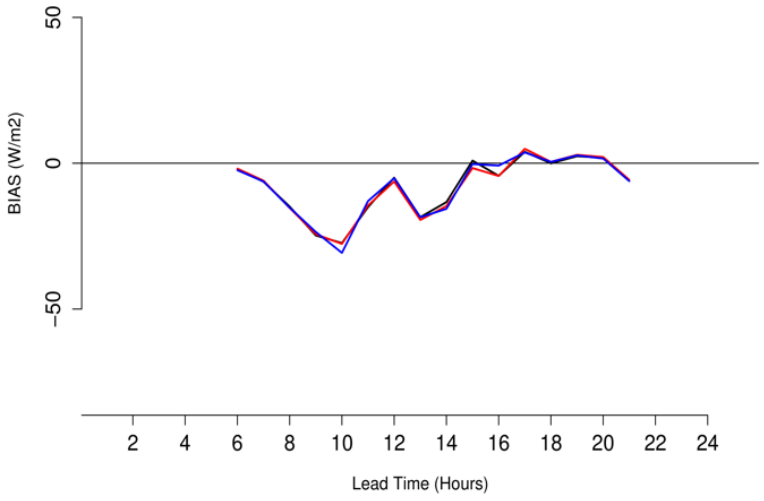

(b)

Figure 26. (a) RMSE (solid line) and spread (dashed line) from 20 (black), 10 (red), and 5 (blue) stochastic ensemble forecasts. (b) Bias from 20 (black), 10 (red), and 5 (blue) stochastic ensemble forecasts

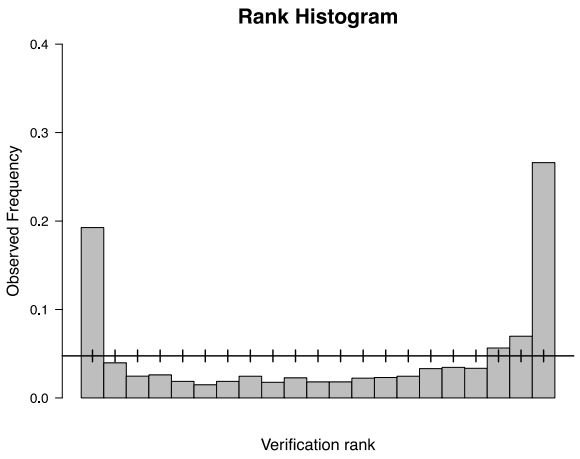

(a)

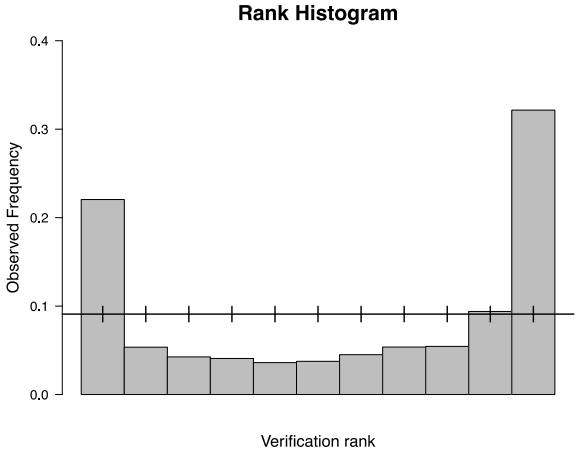

(b)

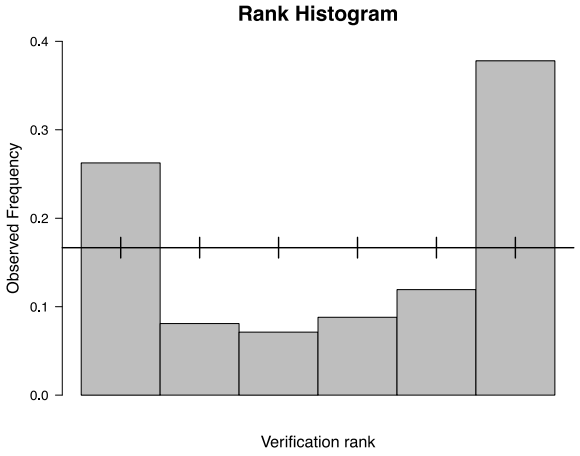

(c)

Figure 27. Rank histogram from (a) 20, (b) 10, and (c) 5 members of the stochastic ensemble forecasts

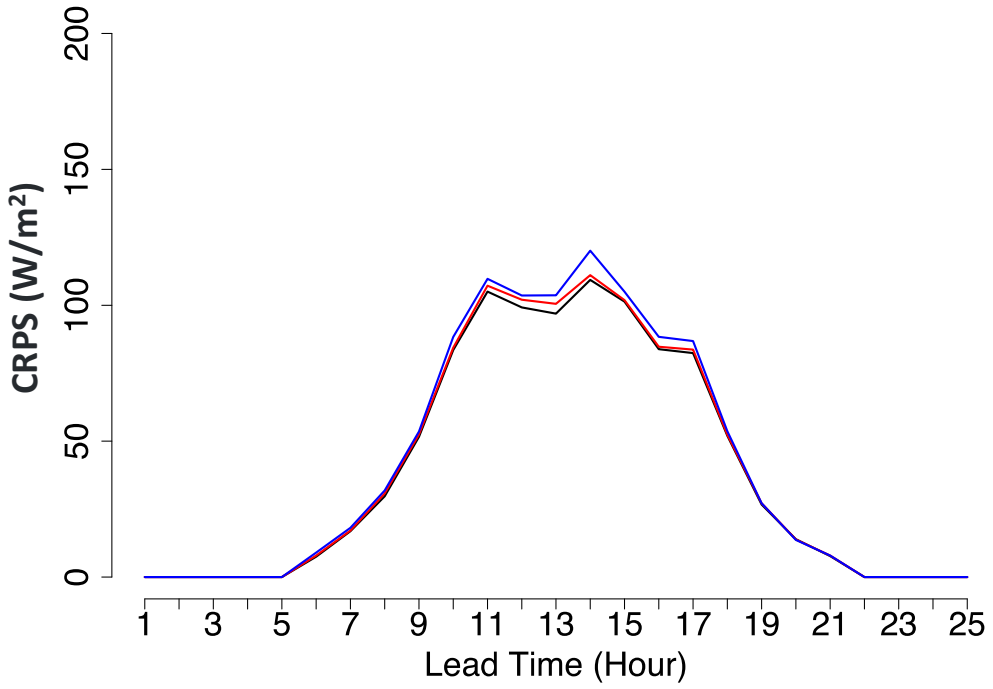

Figure 28. Continuous rank probability score as a function of the lead time from 20 (black), 10 (red), and 5 (blue) members of the stochastic ensemble forecasts

3.2.7 WRF-Solar Experiments Using Different Physics and a Stochastic Perturbation Method

The 24 configurations of the physics parameterizations in WRF-Solar were tested for April 2018, and NSRDB observations were used for validation over CONUS. The 24 configurations are focused on different methodologies for accounting for the effects of unresolved clouds, the grid resolving cloud microphysics, PBL parameterization, and the atmospheric radiation processes. Cloud microphysics and atmospheric radiation processes are the main driver for the formation and dissipation of clouds and solar radiation. The importance of unresolved cumulus clouds on shortwave radiative process was also investigated in Jiménez et al. (2016b).

For this analysis, 30 day-ahead forecasts (i.e., 24-hours ahead at 30-minute resolution) were simulated for April 2018 (30 samples). All the forecasts were initialized at 06 UTC, and the NSRDB observations were used for the validation of the forecasts over CONUS.

Figure 29a shows the bias of the GHI computed at each grid point (600 x 354) of the WRF-Solar domain, and **Figure 29b** shows the MAE of the GHI as a function of lead time. Various combinations of WRF-Solar physics have been tested. The combinations include four types of shallow cumulus schemes (Deng, CLD3, MYNN, and Grell), four types of cloud microphysics schemes (Thompson aerosol awareness, Thompson, WSM6, and Goddard), three types of shortwave radiation schemes (Rapid Radiative Transfer Model for GCMs [RRTMG], Dudhia, and Goddard), and three types of PBL schemes (MYNN, YSU, and MYJ). The 10 members of the WRF-Solar stochastic ensemble based on WRF-Solar_V1 (couple_farms=true) have also been included in the analysis.

The WRF-Solar_V1 without shallow cumulus scheme exhibits the smallest bias and MAE scores. The 10 members of the WRF-Solar stochastic forecast also show good agreement with the NSRDB observations, with MAE scores similar to those of the WRF-Solar_V1 without the shallow cumulus experiment. This indicates that our control physics configuration of the MYNN PBL, Thompson aerosol awareness, Noah LSM, Deng shallow cumulus, and RRTMG radiation schemes is working reasonably for the day-ahead GHI forecasts. The performance of 10 members of the WRF-Solar stochastic ensemble is confirmed based on these results, and an ensemble calibration is applied to the 10 stochastic ensemble members (Section 4).

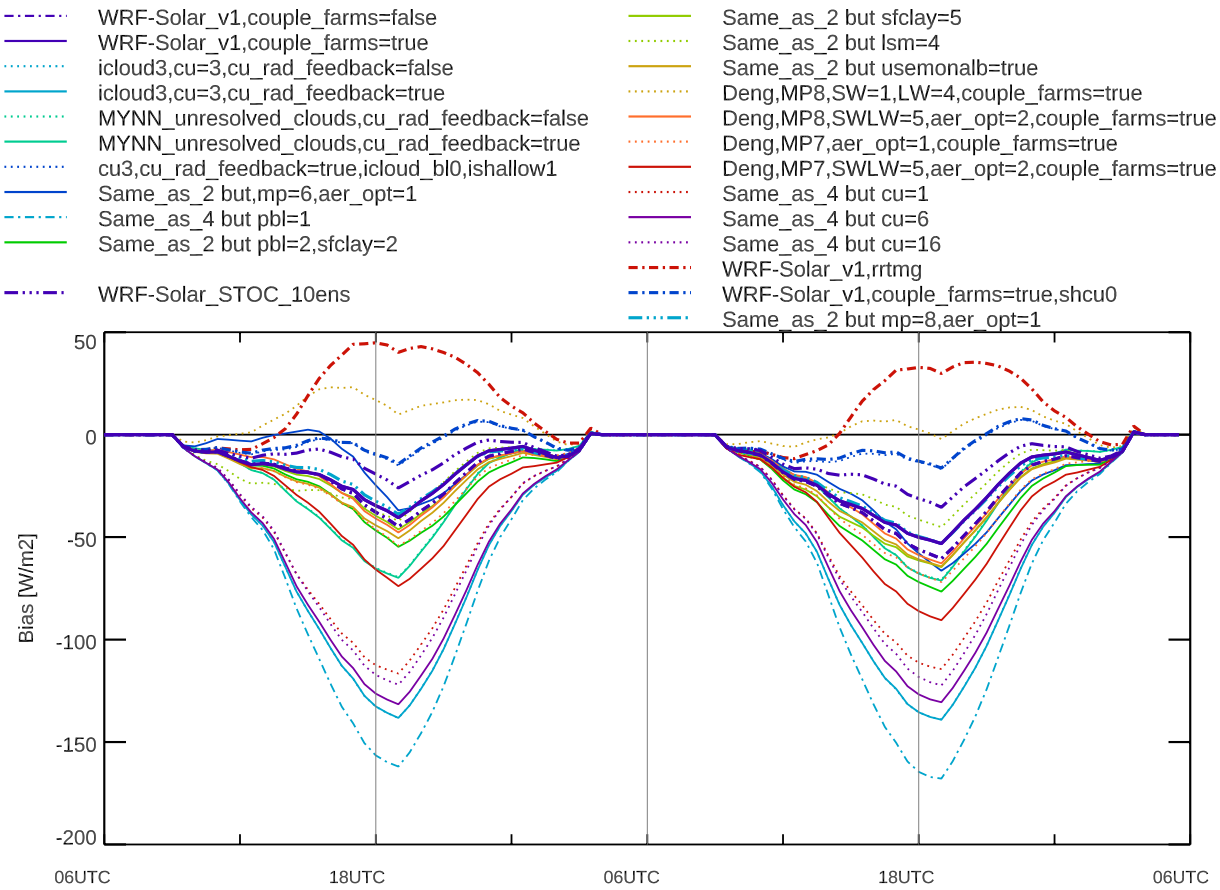

(a)

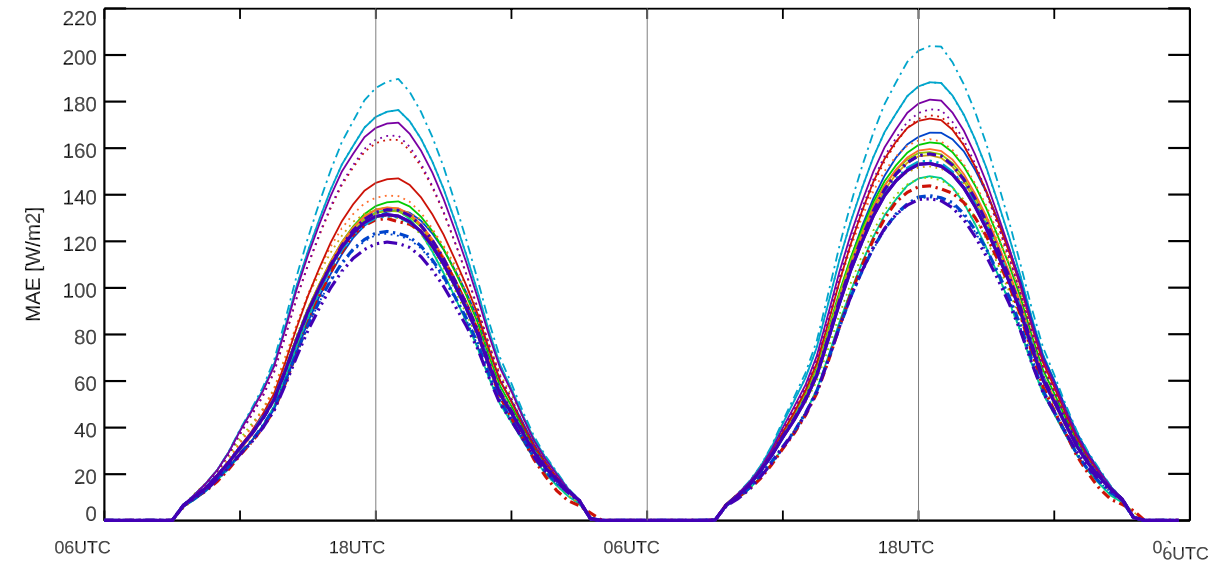

(b)

Figure 29. (a) Bias and (b) MAE of the GHI from 24 different configurations of WRF-Solar against NSRDB observations over the CONUS domain for April 2018. The statistical metrics are calculated with all available data at a given lead time.

3.2.8 Representation of Horizontal Cloud Fraction in FARMS

FARMS was lacking a horizontal cloud fraction. This led to an overestimation of the GHI predictions under regimes with partial cloudiness. To overcome this limitation, we investigated four cloud fraction representation methods in the FARMS scheme:

1. Maximum overlap. The horizontal cloud fraction (CLDFRA_H) is represented following Eq. 3.5, which uses the maximum fraction value in 40 vertical layers (max_cldfra):

$$CLDFRA\_H(i,j) = \max(cldfra(i,*,j) \tag{3.5}$$

   where cldfra is the three-dimensional variable for cloud fraction.

2. Weighted average by cloud mass from Eq. 3.6 (wgtAvg_cldfra):

$$CLDFRA\_H = \sum_{n=1}^{nlayer} \frac{Q\_clouds\ (n)}{\sum_{k=1}^{nlayer} Q\_clouds\ (k)} \times cldfra(n) \tag{3.6}$$

   where Q_clouds represents the sum of cloud water, ice, and snow.

3. The third method is to use a logarithm average, as in Eq. 3.7 (logAvg_cldfra):

$$CLDFRA\_H = \exp[\left(\sum_{k=1}^{nlayer} \log(cldfra(k))\right)/nlayer] \tag{3.7}$$

4. Use a CLDFA_H value of 1 (wo_cldfra).

Simulations from the RRTMG were also tested, and these results were compared to NSRDB observations in January 2018 and July 2018. **Figure 30 and Figure 31** compare the bias and the MAE of the five different experiments. When the cloud fraction is set to (1), the result shows the smallest bias, but it is difficult to say that the forecast result is improved even though positive bias has been reduced. Indeed, the MAE shows a larger value than the other methodologies. The weighted average by clouds method (wgtAvg_cldfra) shows the best MAE performance. Based on these results, we selected the weighted average method in FARMS.

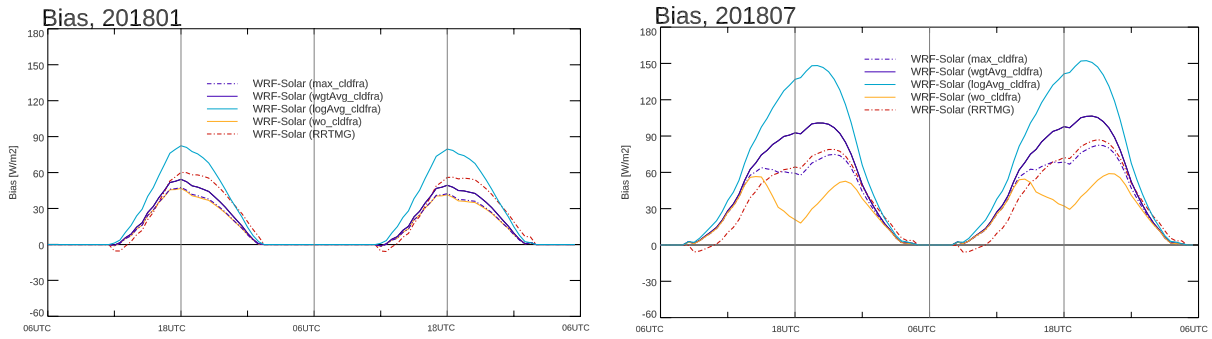

Figure 30. Bias calculated at each forecast lead time in (a) January 2018 and (b) July 2018 for five different experiments

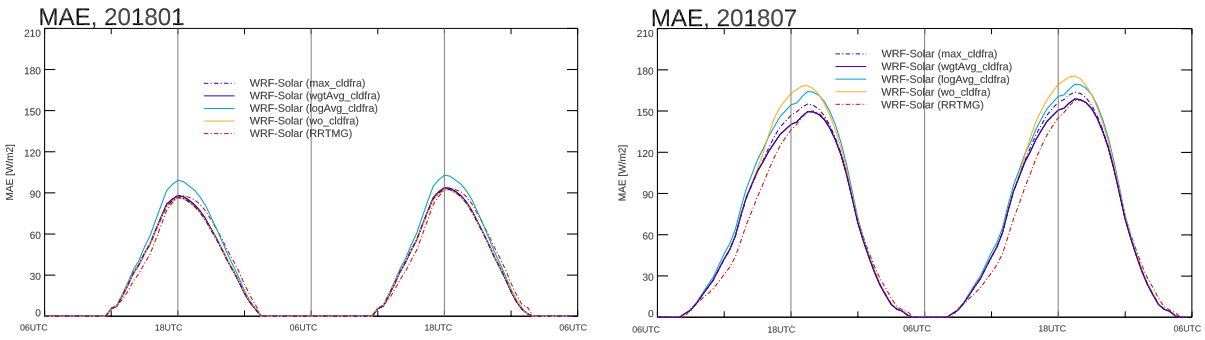

(a) (b)

Figure 31. MAE calculated at each forecast lead time in (a) January 2018 and (b) July 2018 for five different experiments

4 Validation of Day-Ahead Forecasts

4.1 Ensemble Calibration

4.1.1 Analog Ensemble

The analog ensemble (AnEn) technique (Alessandrini, Sperati, and Delle Monache 2019) was applied to calibrate ensemble forecasts of GHI and DNI simulated from the WRF-Solar EPS. The AnEn method selects a set of past observations that corresponded to the best analogs of the NWP and provides a set of ensemble members of the selected observation data set. The set of ensemble members can then be used in a probabilistic or deterministic (e.g., ensemble mean of AnEn) way.

The analog metric is defined as follows (Delle Monache et al. 2011; Delle Monache et al. 2013; Alessandrini, Sperati, and Delle Monache 2019):

$$\|F_t, A_{t'}\| = \sum_{i=1}^{N} \frac{w_i}{\sigma_{f_i}} \sqrt{\sum_{j=-\tilde{t}}^{\tilde{t}} (F_{i,t+j} - A_{i,t'+j})^2} \tag{4.1}$$

where F_t is the current forecast at future time t; $A_{t'}$ is an analog forecast with the same forecast lead time but valid at a past time t'; N and w_i are the number of meteorological predictors and their weights; σ_{f_i} is the standard deviation of the time series of past forecasts of a given predictor at the same location (to normalize the contribution to the metric of predictors with different units); $\tilde{t}$ is half of the time window over which the analog metric is computed; and $F_{i,t+j}$ and $A_{i,t'+j}$ are the values of the current forecast and the analog of the atmospheric predictors in the time window.

In this work, the training data set comprised 365 sets of WRF-Solar EPS simulations covering 2017. We used four predictors to select the best analogs sets from past forecasts for each station (Kim et al. 2021)—the mean of GHI, the mean of DNI, the standard deviation of GHI, and the standard deviation of DNI—from 10 ensemble members simulated from WRF-Solar EPS (see Section 4.1.2). The weight optimization was performed independently for each location by choosing the optimal weights that minimize the error over the training data set (2017).

4.1.2 Impact of Different Combinations of AnEn Predictors

We tested different sets of predictors: the mean and standard deviation of GHI, DNI, 2-m temperature, and the total column of water vapor from WRF-Solar EPS. This AnEn technique includes a "weight optimization" method that can allocate a different weight to each predictor. The impact of the weight optimization was also compared. **Table 5** includes AnEn predictor combinations applied to the calibration of WRF-Solar EPS.

Table 5. AnEn Predictor Combinations

Predictor Combination	Predictor							
	GHI (Mean)	GHI (Std)	DNI (Mean)	DNI (Std)	Temperature (Mean)	Temperature (Std)	Water Vapor (Mean)	Water Vapor (Std)
1P	√							
2P	√	√						
4P	√	√	√	√				
4P_T	√	√			√	√		
4P_W	√	√					√	√

Figure 32 shows the bias and RMSE of the AnEn prediction results. The yellow boxes show the results of the unweighted optimization, which implies that all predictors have the same weight. The green boxes show the results of the weight optimization. For example, yellow 4P_T means that the mean and standard deviation of GHI and DNI are used as predictors, and each predictor has the same weight. The best results using RMSE and bias as metrics are obtained when using the mean and standard deviation of GHI and DNI as predictors (4P).

When we analyzed the results from using an optimized weight distribution, the mean of GHI had the highest weight for all combinations, but the weight optimization did not significantly improve the results in this study.

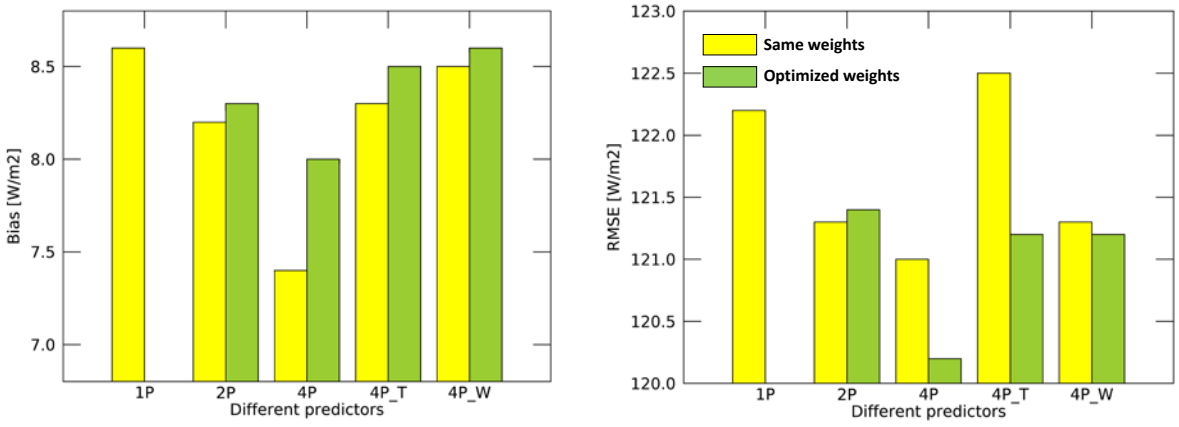

(a) (b)

Figure 32. The mean (a) bias and (b) RMSE of the calibrated WRF-Solar EPS for different combinations of predictors

4.1.3 Evaluation of Calibrated Forecasts

The AnEn has been applied to calibrate the GHI prediction from the WRF-Solar forecasting system over CONUS for every 5 x 5 WRF grid point (8,520 grid points). We compared the forecast results of two prediction systems: WRF-Solar V1 and WRF-Solar EPS. The analog ensemble (AnEn) has been applied to calibrate the solar irradiance forecast results from these two systems.

Figure 33 shows the maps of the RMSE in the GHI prediction over the CONUS region. The upper panels are the results of the raw forecasts, which are WRF-Solar V1 and WRF-Solar EPS. The lower panels are the results of the calibrated ensembles from the two systems. WRF-Solar EPS reduces the RMSE in WRF-Solar V1 by 9%, and the AnEn reduces the RMSE in WRF-Solar EPS by 5%. The total improvement of 14% is attained by the calibrated WRF-Solar EPS, indicated by the reduction in RMSE with respect to WRF-Solar V1. The GHI bias is reduced by 81% (calibrated WRF-Solar EPS versus WRF-Solar V1) (**Figure 34**). The calibrated WRF-Solar EPS provides unbiased estimations of the solar irradiance within 1% of the satellite observations of GHI.

Figure 35 exhibits the RMSE maps for DNI. Compared to WRF-Solar V1, WRF-Solar EPS reduces the RMSE by 7% in the DNI prediction, and the AnEn reduces the RMSE in WRF-Solar EPS by 10% in the DNI prediction. Consistent with the GHI results for RMSE, an overall improvement of 16% for DNI is attained by the calibrated WRF-Solar EPS (calibrated WRF-Solar EPS versus WRF-Solar V1). The DNI bias is reduced by 75% (calibrated WRF-Solar EPS versus WRF-Solar V1) (**Figure 36**). The calibrated WRF-Solar EPS improves the DNI forecasts of WRF-Solar V1 with unbiased estimations of the DNI within 3.2% of the satellite observations.

Figure 37 shows the annual cycles of bias, RMSE, and correlation in GHI prediction. The AnEn reduces the positive biases, especially in the summer season. The calibrated WRF-Solar EPS shows the smallest RMSE throughout 2018. The WRF-Solar EPS shows a higher correlation than WRF-Solar V1.

Figure 38 shows the diurnal cycles of bias, RMSE, and correlation in GHI prediction. Results shows that the diurnal cycle of the bias scores of the calibrated WRF-Solar V1 is similar to that of the calibrated WRF-Solar EPS. The calibrated WRF-Solar EPS shows the smallest RMSE throughout the day. Also, the calibrated WRF-Solar EPS reduces the RMSE peak of WRF-Solar V1 by 17%. The WRF-Solar EPS shows a correlation value as high as the calibrated WRF-Solar.

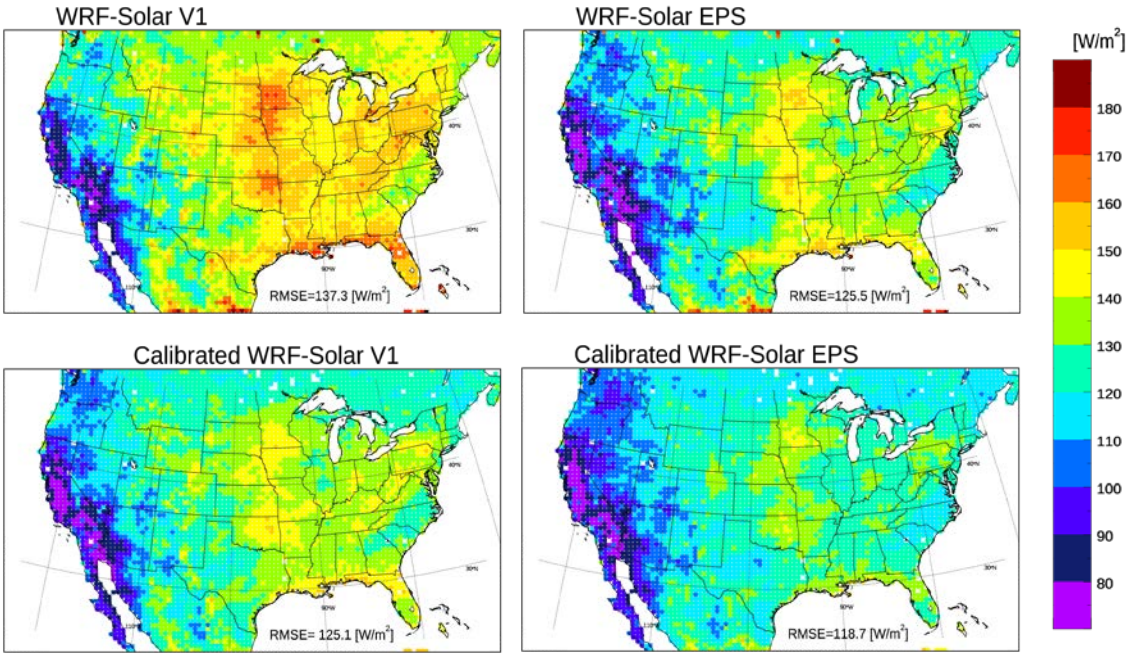

Figure 33. RMSE maps of GHI forecasts from WRF-Solar V1, WRF-Solar EPS, the calibrated WRF-Solar V1, and the calibrated WRF-Solar EPS against 2018 NSRDB observations

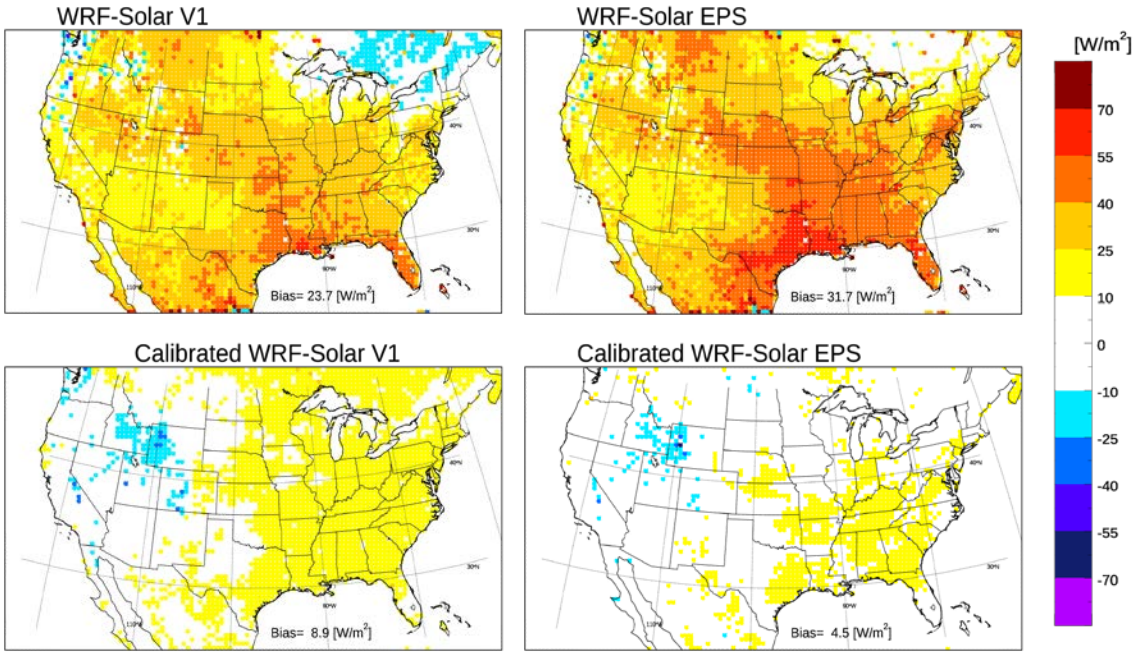

Figure 34. Bias maps of GHI forecasts from WRF-Solar V1, WRF-Solar EPS, the calibrated WRF-Solar V1, and the calibrated WRF-Solar EPS against 2018 NSRDB observations

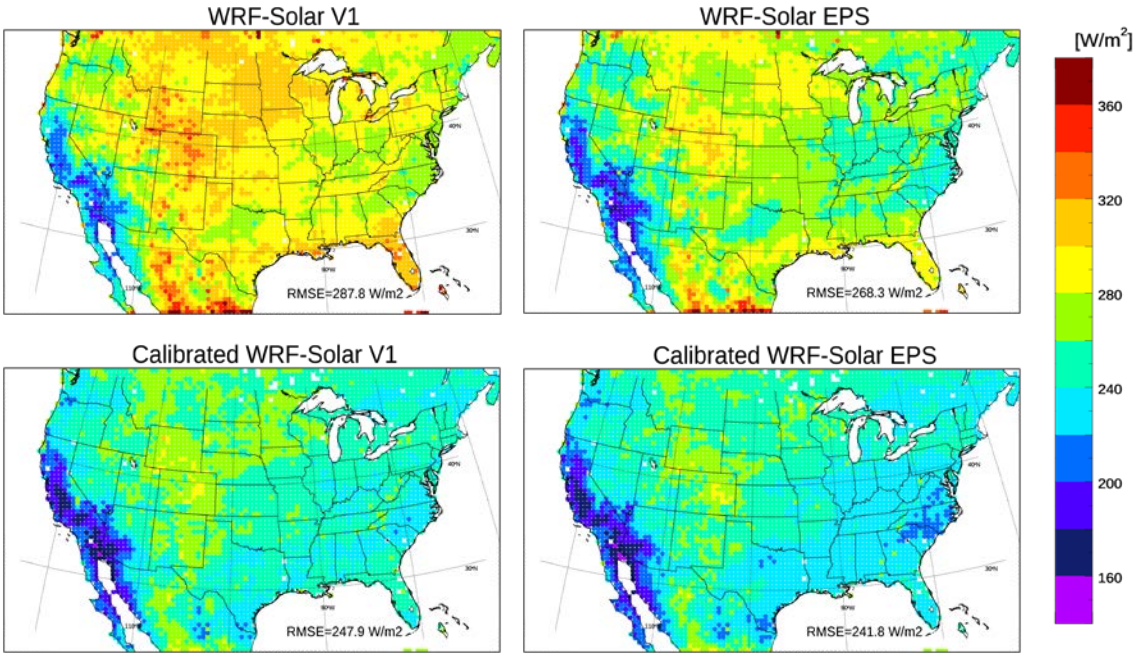

Figure 35. RMSE maps of DNI forecasts from WRF-Solar V1, WRF-Solar EPS, the calibrated WRF-Solar V1, and the calibrated WRF-Solar EPS against 2018 NSRDB observations

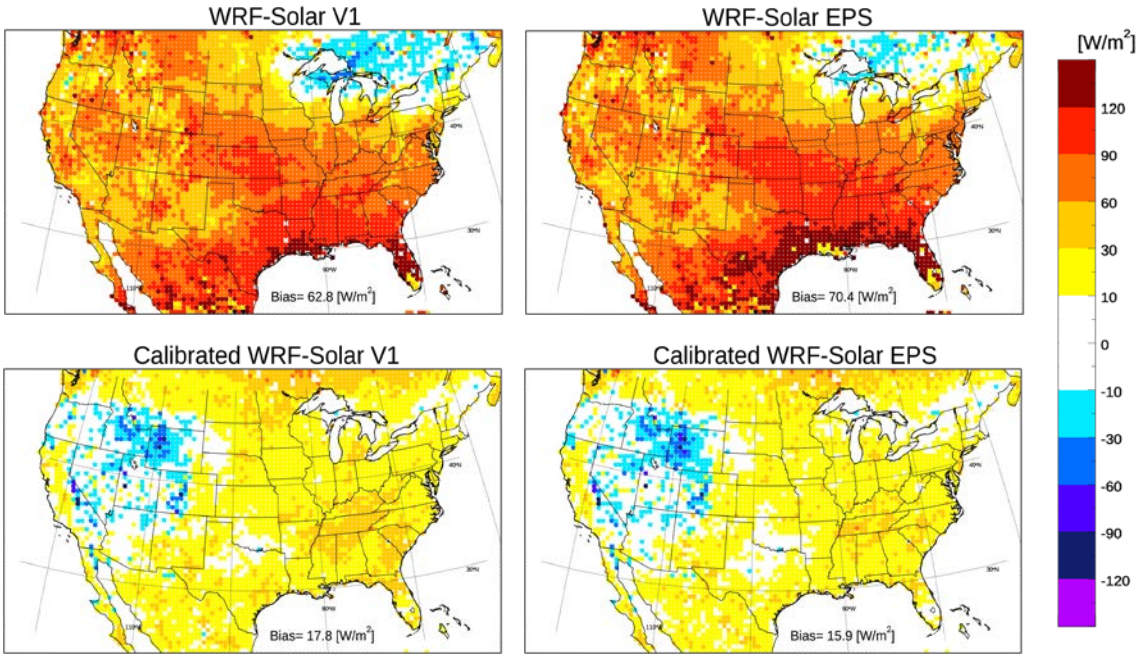

Figure 36. Bias maps of DNI forecasts from WRF-Solar V1, WRF-Solar EPS, the calibrated WRF-Solar V1, and the calibrated WRF-Solar EPS against 2018 NSRDB observations

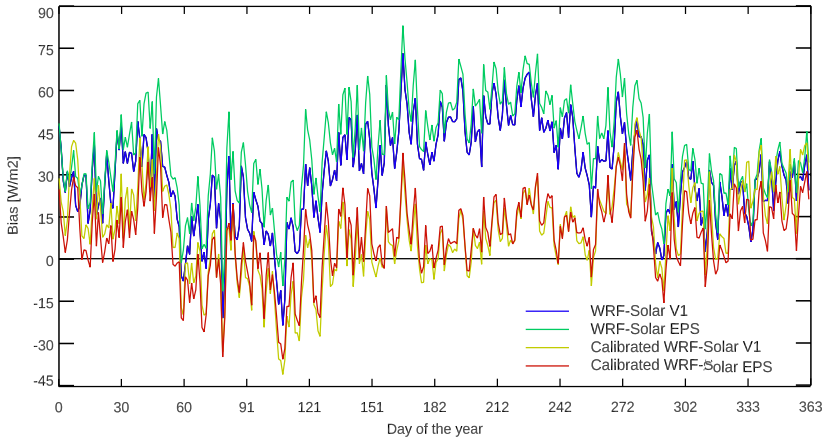

(a)

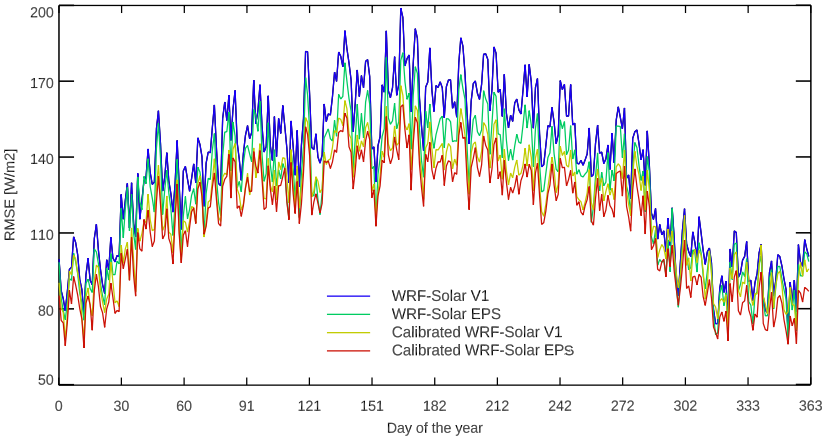

(b)

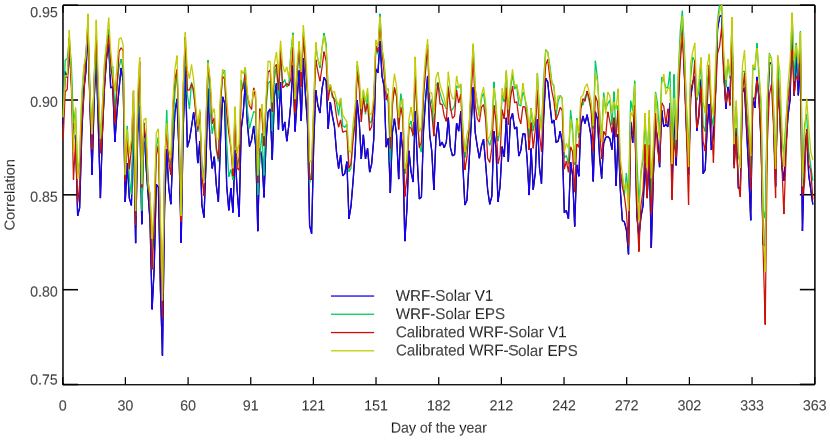

(c)

Figure 37. Annual cycles of (a) bias, (b) RMSE, and (c) correlation of GHI forecasts from WRF-Solar V1, WRF-Solar EPS, the calibrated WRF-Solar V1, and the calibrated WRF-Solar EPS against 2018 NSRDB observations

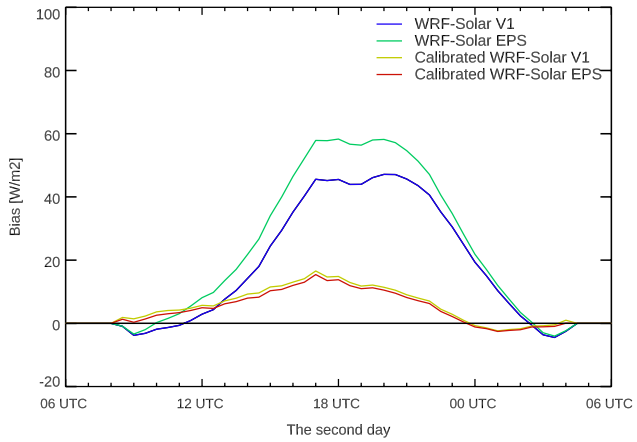

(a)

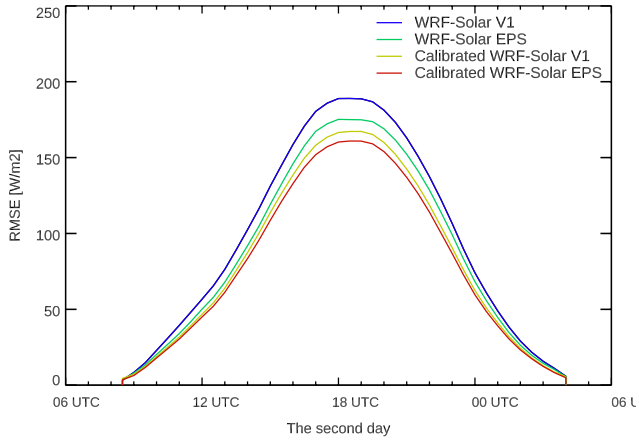

(b)

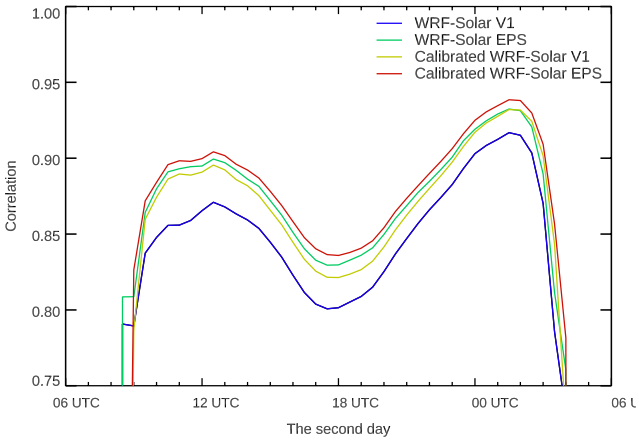

(c)

Figure 38. Diurnal cycles of (a) bias, (b) RMSE, and (c) correlation of GHI forecasts from WRF-Solar V1, WRF-Solar EPS, the calibrated WRF-Solar V1, and the calibrated WRF-Solar EPS against 2018 NSRDB observations

4.2 Forecasts for Topic Area 1 Evaluation Plan

4.2.1 Sites Determined by Topic Area 1

For this task, ground observations were obtained for 1-minute GHI and DNI from 10 stations, including the SURFRAD, SOLRAD, and Atmospheric Radiation Measurement Southern Great Plains sites, etc. **Figure 39** shows the sites determined by Topic Area 1, which include two stations in California and one station each in South Dakota, Oklahoma, Mississippi, Pennsylvania, Virginia, Florida, Washington, and Colorado. **Table 6** includes general information for the locations of the ground measurements. We acquired the observations from the Solar Forecast Arbiter website (https://solarforecastarbiter.org) and processed the data sets to meet the requirements for the Topic Area 1 evaluation plan. The data sets were used to perform calibrations and evaluations of GHI and DNI forecasts simulated from WRF-Solar EPS.

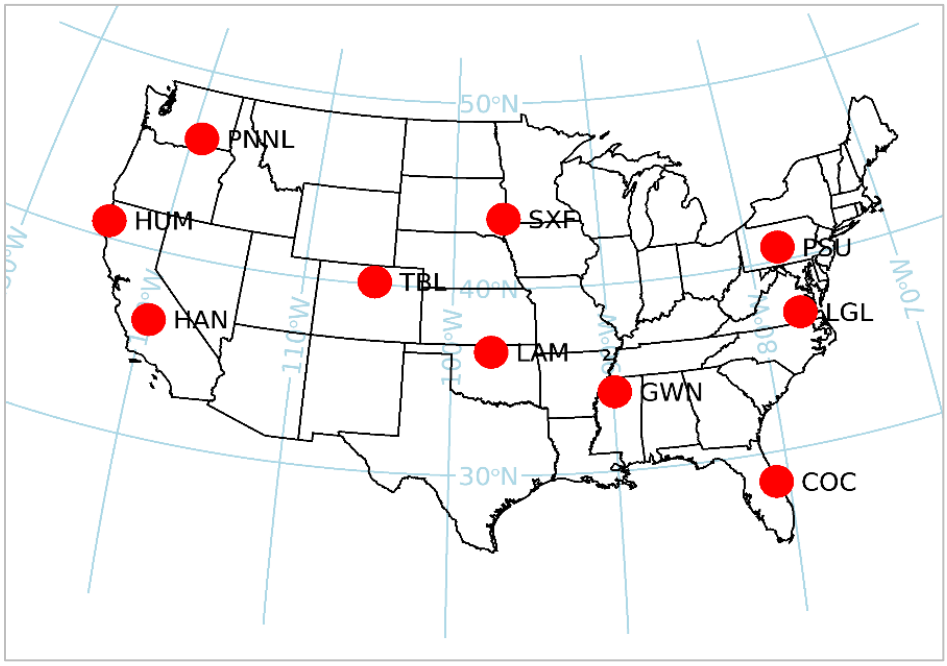

Figure 39. Observation locations determined by Topic Area 1

Table 6. Information of 10 Sites in Figure 39

Name	Latitude (°N)	Longitude (°W)	Elevation (m)	Time Zone
NASA Langley, VA (LGL)	37.10	77.39	3	UTC-5
Goodwin Creek, MS (GWN)	34.25	89.87	98	UTC-6
Penn. State Univ., PA (PSU)	40.72	77.93	376	UTC-5
Sioux Falls, SD (SXF)	43.73	96.62	473	UTC-6
Hanford, CA (HAN)	36.31	119.63	73	UTC-8
Lamont, OK (LAM)	36.61	97.49	307	UTC-6
Humboldt State Univ., CA (HUM)	40.88	124.08	36	UTC-8
Cocoa Beach, FL (COC)	28.40	80.77	11	UTC-5
Richland, WA (PNNL)	46.34	119.28	123	UTC-8
Table Mountain, CO (TBL)	40.12	105.24	1689	UTC-7

4.2.2 Calibration of WRF-Solar Ensemble for Locations Determined by Topic Area 1

The predictability of solar irradiances from WRF-Solar EPS and the calibrated WRF-Solar EPS was evaluated using the ground-measured observations provided by the Solar Forecast Arbiter. We analyzed the final products to be delivered that meet all requirements for the 10 sites determined by the Topic Area 1 evaluation plan.

The WRF-Solar model was configured to provide day-ahead predictions over CONUS using 9-km grid spacing. One year (365 days) of day-ahead forecasts spanning December 31, 2017–December 30, 2018, were produced for every 15 minutes from WRF-Solar EPS. Each simulation was initialized at 6 UTC, and the forecast length was 48 hours. The National Centers for Environmental Prediction Global Forecast System (0.25° x 0.25°; 3-hour intervals) forecast data were used for the initial and boundary conditions of the WRF-Solar model. We simulated 10 ensemble members to predict GHI and DNI from WRF-Solar EPS.

The AnEn technique (Alessandrini, Sperati, and Delle Monache 2019) was applied to calibrate the ensemble forecasts of GHI and DNI simulated from WRF-Solar EPS. The training data set comprised 365 sets of WRF-Solar EPS simulations covering 2017. We used four predictors to select the best analogs sets from past forecasts for each station: the mean of GHI, the mean of DNI, the standard deviation of GHI, and the standard deviation of DNI. The WRF-Solar reference (WRF-Solar REF; Jiménez et al. 2022) forecast has been simulated and compared to the calibrated WRF-Solar EPS forecast results. The WRF-Solar REF configuration was used for the WRF-Solar REF simulation, which is a deterministic forecast.

Forecasts of GHI and DNI obtained from WRF-Solar REF and the calibrated WRF-Solar EPS were evaluated against surface observations covering the full year of 2018. The bias and RMSE were calculated with all available model-observation pairs at a given forecast lead time for the second day.

Figure 40 and **Figure 41** display diurnal cycles of bias and RMSE of the two forecast results. It is observed that AnEn effectively reduces biases for both the GHI and DNI forecasts. **Figure 42** and **Figure 43** exhibit bias and RMSE computed with all available predicted and observed data of GHI and DNI for each station. Improvements from the ensemble calibration are indicated by the overall reductions in bias and RMSE across all stations. In particular, a large reduction in bias and RMSE is achieved by AnEn for the Humboldt State University site (**Figure 42**), which is near the coastline, which is generally prone to large forecast errors. Predicted DNI shows higher forecast errors compared to predicted GHI from WRF-Solar EPS. Nevertheless, the AnEn calibration improved the ensemble DNI forecasts for all 10 locations (**Figure 43**).

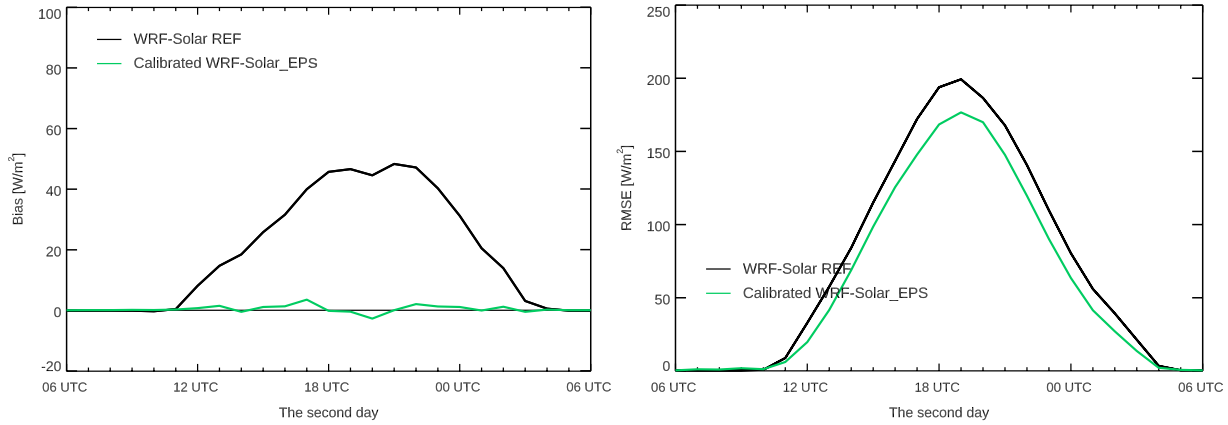

Figure 40. (a) Bias and (b) RMSE of the 2018 GHI forecasts for WRF-Solar REF (black) and the calibrated WRF-Solar EPS (green) as a function of forecast lead time

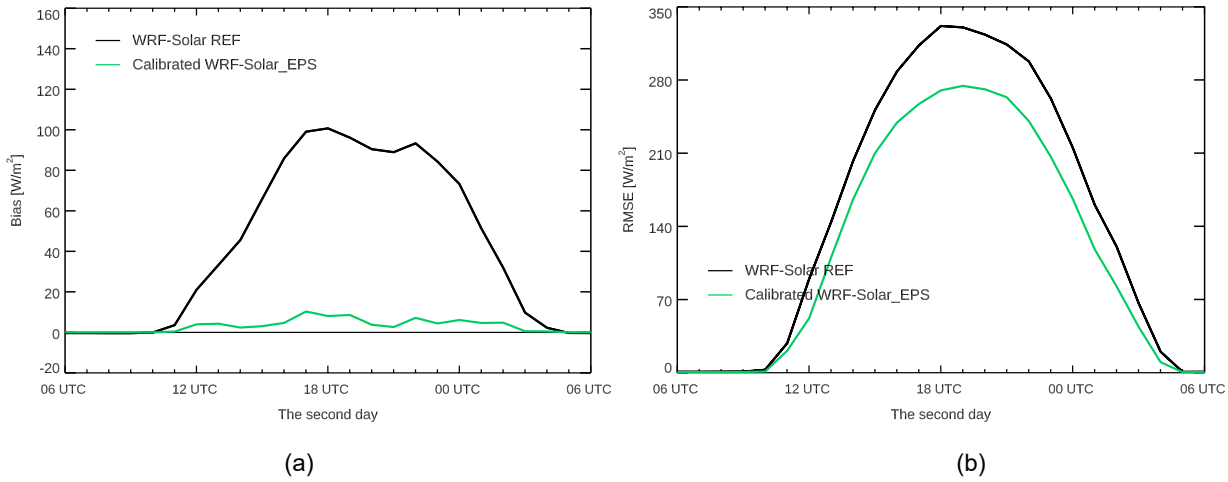

Figure 41. Same as Figure 40 except for the 2018 DNI forecasts

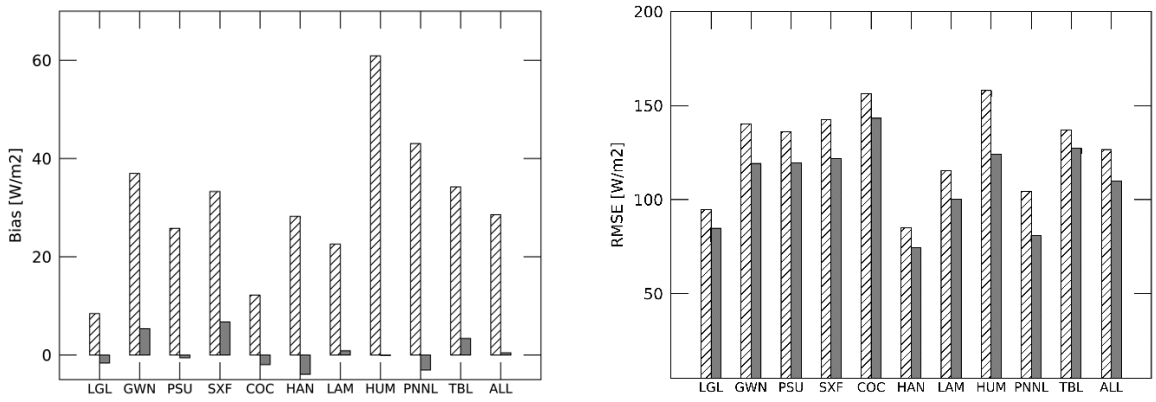

(a) (b)

Figure 42. (a) Bias and (b) RMSE of the 2018 GHI forecasts using WRF-Solar EPS (hatched rectangular) and the calibrated WRF-Solar EPS (gray rectangular) for each station (LGL, GWN, PSU, SXF, COC, HAN, LAM, HUM, PNNL, and TBL) and all stations (ALL)

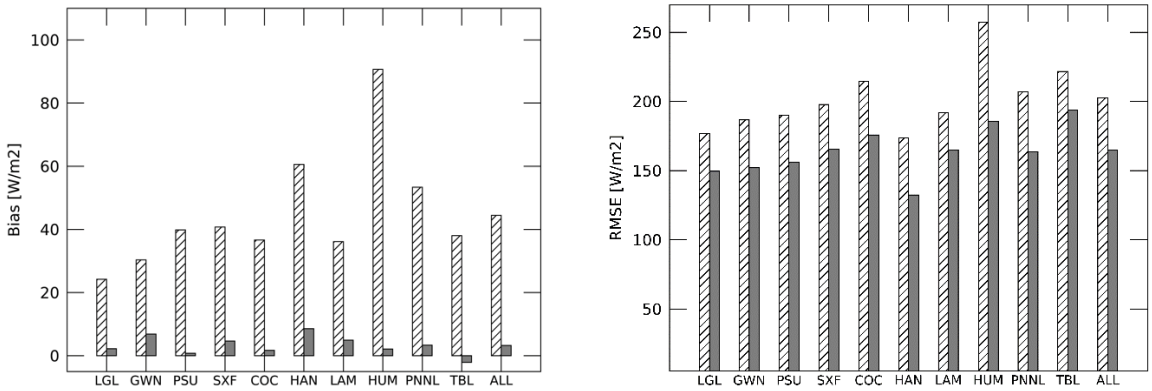

(a) (b)

Figure 43. Same as Figure 4 except for the DNI forecasts

4.2.3 Uploading National Renewable Energy Laboratory Forecasts to the Solar Forecast Arbiter

We completed the upload of the day-ahead forecast data to the Solar Forecast Arbiter. Forty sets of forecast data for the year 2018 [i.e., 10 stations × 2 variables (GHI and DNI) × 2 forecasts (average of calibrated ensemble members and reference WRF-Solar forecasts)] were processed to meet all requirements shown in **Table 7**. An example of the uploaded data to the website is in **Figure 44**.

Table 7. Requirements for Day-Ahead Forecasts for Topic Area 1 Evaluation Plan

Variables	Evaluation Time Range	Forecast Parameters
GHI DNI	Start: 2018-01-01 00:00 local time at each site End: 2018-12-31 23:59 local time at each site	Forecast issue time: 10 a.m. local standard time Forecast lead time: 14 hours Forecast run length: 24 hours Value type: interval mean Interval length: 1 hour Interval label: ending

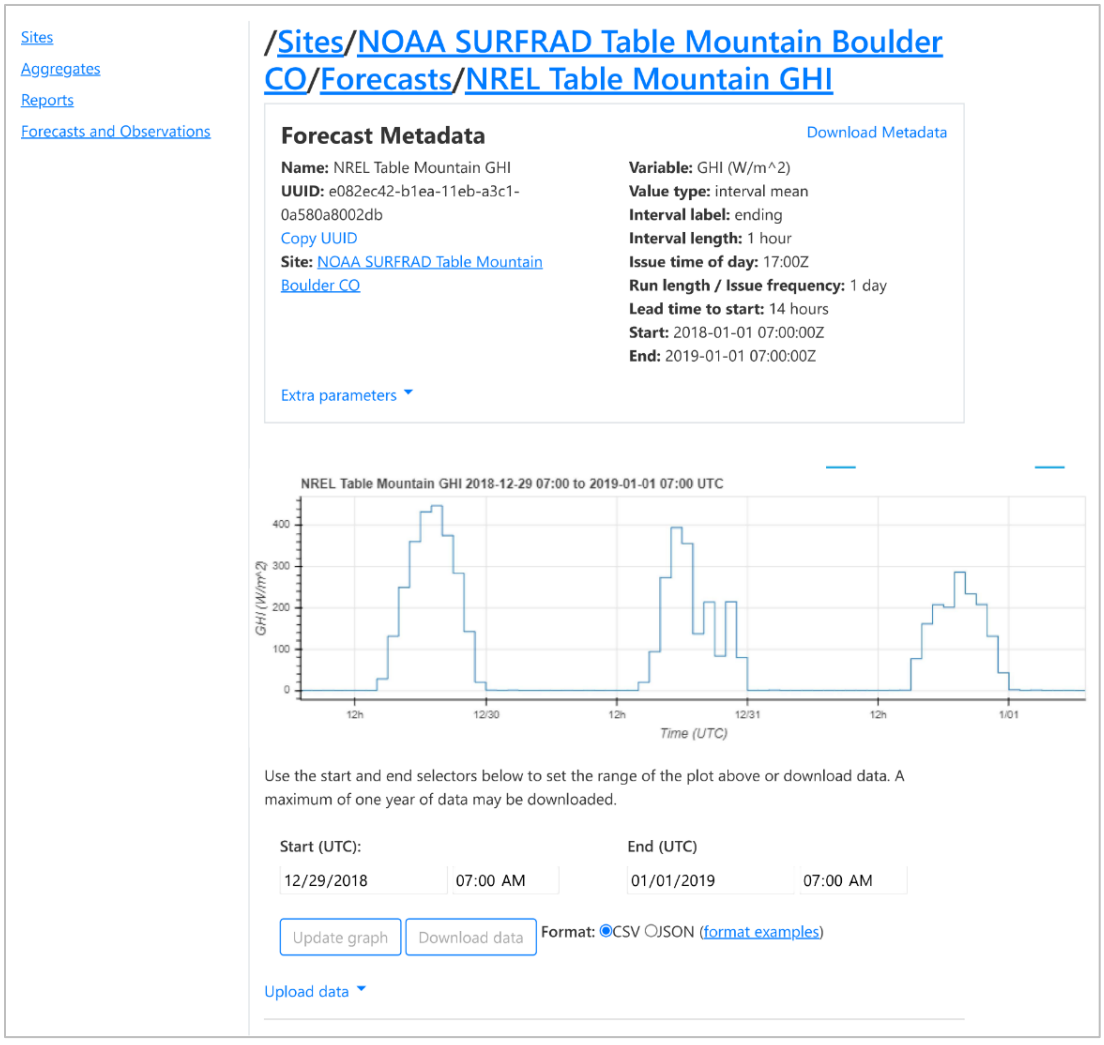

Figure 44. An example of uploaded GHI forecasts on the Solar Forecast Arbiter

4.3 Evaluation of Solar Irradiance Forecasts from WRF-Solar Using the National Solar Radiation Database

We explored the use of the NSRDB to evaluate solar irradiance forecasts from WRF-Solar. In this work, we analyze the advantages and limitations of using GHI observations from the NSRDB to quantify the performance of the WRF-Solar model as well as to evaluate GHI

forecasts from WRF-Solar with a robust analysis framework in time and space. This aims to further understand the model performance to continue improving the value of WRF-Solar for solar energy applications. Based on our findings for 2018, the model bias is positive in winter and in summer indicates an underestimation of the cloudiness field, or the simulation of optically thinner clouds, or a combination of both. In addition, the reference WRF-Solar configuration in combination with NSRDB retrievals has been used to explore sensitivities to the model configuration and to quantify the degradation of the forecasts as a function of the lead time. The model sensitivities also explored the impact of increasing the grid spacing from 9 km (reference) to 3 km and the benefits of parametrizing shallow cumulus at both resolutions. This work was presented in Jiménez et al. 2022.

4.4 Model Inter-Comparison between WRF-Solar V1, WRF-Solar EPS, SKEBS, and the Physics-Based Ensemble of WRF-Solar

This study evaluates simulated solar irradiance forecasts from WRF-Solar V1, WRF-Solar EPS, the stochastic kinetic energy backscatter scheme (SKEBS) (Shutts 2005; Berner et al. 2009; Berner et al. 2011; Berner et al. 2015), and the multiphysics ensemble of WRF-Solar (WRF-Solar PHYS). One-year simulations covering 2018 have been completed for the four WRF systems. WRF-Solar V1 is a deterministic forecast system. WRF-Solar EPS introduces stochastic perturbations in the most relevant physical variables for solar irradiance predictions in WRF-Solar V1. In SKEBS, kinetic energy from unresolved scales is made available, or backscattered onto, the resolved scales via stochastic perturbations of the stream function and potential temperature at selected wave numbers. The WRF-Solar PHYS system runs 10 different combinations of the physics parameterization suite of WRF-Solar V1.

Figure 45 compares distributions of MAE. All forecasts show higher forecasting errors in the eastern United States, and the regions with large errors in the prediction results are highly correlated with the optically thick cloud regions. WRF-Solar EPS significantly reduces the MAE of WRF-Solar V1 in the eastern region. Forecast results from SKEBS and WRF-Solar PHYS show lower MAE than WRF-Solar EPS.

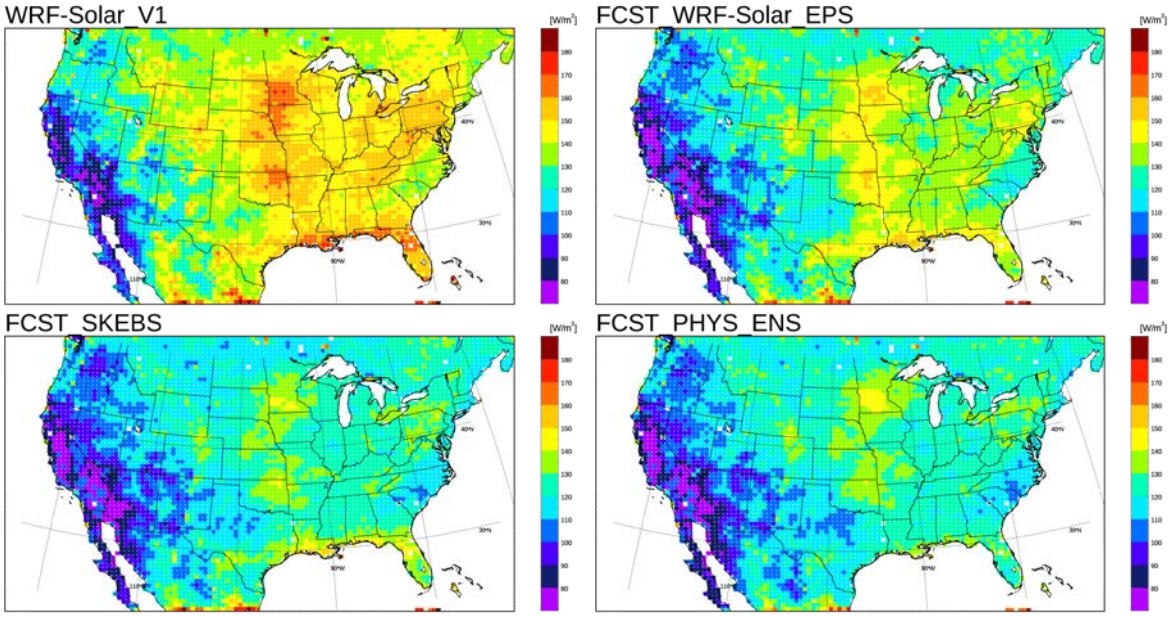

Figure 45. Spatial distribution of MAE of the 2018 GHI forecasts from WRF-Solar V1, WRF-Solar EPS, SKEBS, and WRF-Solar PHYS against the NSRDB observations

Figure 46 compares rank histograms and missing rate error (MRE) from three ensemble forecast systems. Three ensemble systems show under-dispersive prediction results. WRF-Solar PHYS produces an ensemble with better statistical consistency than WRF-Solar EPS and SKEBS. It is anticipated that the three ensemble systems will be improved insofar as ensemble calibration techniques are applied.

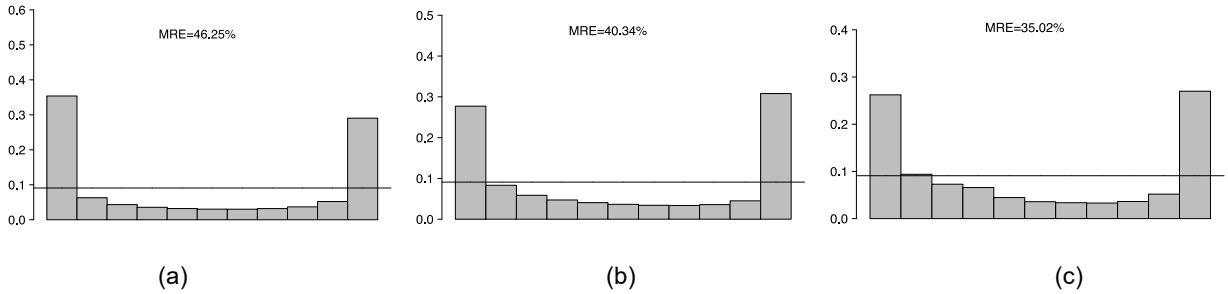

Figure 46. Rank histogram for the 2018 GHI forecasts from (a) WRF-Solar EPS, (b) SKEBS, and (c) WRF-Solar PHYS against the NSRDB observations

4.5 Evaluation of Cloud Mask Forecasts from WRF-Solar EPS

The main purpose of this study is to develop a method to evaluate cloud forecasts from NWP models. The limitation in the current verification of gridded solar forecasts, which focus only on the evaluation of NWP outputs for the prediction of solar irradiance using simple statistical metrics, has motivated a new approach in this study to assess the prediction accuracy of solar irradiance. Forecasting of clouds in NWP is the key factor in predicting solar irradiance because that directly impacts the solar irradiance under overcast or partial cloudy-sky conditions (i.e., solar irradiance forecasts are influenced by errors stemming from the cloud forecasts); thus, it is essential to implement an evaluation of cloud forecasts from NWP models.

In this work, we propose a method for validating cloud products from WRF-Solar EPS to provide grid operators with high-quality probabilistic solar forecasts.

This work includes three objectives:

1. Assessment of cloud mask forecasts from WRF-Solar against the NSRDB
2. Analysis of cloud detection metrics (e.g., hit rate, false alarm rate, Kuiper's skill score)
3. Development of evaluation techniques to verify WRF-Solar EPS using the cloud detection metrics.

The cloud detection metrics introduced by Karlsson and Johansson (2013) were used to quantify the results. We evaluated 10 stochastic ensemble members simulated by WRF-Solar EPS against NSRDB data sets for 2018.

To analyze the capability of WRF-Solar EPS predicting the cloud mask, we need to filter the NSRDB and the forecasts of WRF-Solar EPS for clear- and cloudy-sky conditions. The following are the main steps of the filtering algorithm:

- Step1: An absolute difference between clear-sky GHI and all-sky GHI is calculated for each individual pixel and time step:

$$DIFF = \left| GHI_{Clear} - GHI_{All\ Sky} \right| \tag{4.2}$$

- Step 2: Each pixel is filtered by the conditions in **Table 8**. If DIFF from Eq. 4.2 is smaller than 1 W/m^2, the pixel is treated as clear sky; otherwise, the pixel is treated as cloudy sky. For ensemble forecasts simulated from WRF-Solar EPS, additional criteria are employed. For example, if more than 50% of the ensemble members satisfy the condition of DIFF ≥ 1.0 W/m^2, that pixel is treated as cloudy sky. Note that nighttime data are excluded by filtering with a threshold for inclusion (0° < solar zenith angle < 85°) in this analysis.

Table 8. Criteria for Data Processing of NSRDB and WRF-Solar EPS for Clear-/Cloudy-Sky Conditions

	NSRDB	WRF-Solar EPS
Clear sky	DIFF < 1.0 W/m^2	> 50% of ensemble members are: DIFF < 1.0 W/m^2
Cloudy sky	DIFF ≥ 1.0 W/m^2	≥ 50% of ensemble members are: DIFF ≥ 1.0 W/m^2

After filtering is completed, the cloud detection metrics are calculated based on a contingency table (**Table 9**). The four categories in **Table 9** indicate binary representations for the cloud occurrences for the NSRDB and WRF-Solar EPS.

Table 9. Contingency Matrix for WRF-Solar EPS and NSRDB

		WRF-Solar EPS	
	Scenario	Clear	Cloudy
NSRDB	Clear	a	b
	Cloudy	c	d

We compute the total number of frequencies that corresponded to each category (i.e., a, b, c, and d) and then calculate the following metrics (Karlsson and Johansson 2013) to quantify the results:

$$POD_{clear} = \frac{a}{a+b} \times 100\% \tag{4.3}$$

$$POD_{cloudy} = \frac{d}{c+d} \times 100\% \tag{4.4}$$

$$FAR_{clear} = \frac{c}{a+c} \times 100\% \tag{4.5}$$

$$FAR_{cloudy} = \frac{b}{b+d} \times 100\% \tag{4.6}$$

$$HR = \frac{a+d}{a+b+c+d} \times 100\% \quad (where\ 0 \leq HR \leq 100\%) \tag{4.7}$$

$$KSS = \frac{a \cdot d - c \cdot b}{(a+b) \cdot (c+d)} \times 100\% \quad (where\ -100\% \leq KSS \leq 100\%) \tag{4.8}$$

Monthly variation of four metrics was assessed—including false alarm rate (FAR) and probability of detection (POD) in cloudy conditions, hit rate (HR), and Kuiper's skill score (KSS)—calculated from paired data sets of WRF-Solar EPS and the NSRDB (**Figure 47**). The metrics are calculated independently for each grid points and then spatially averaged as a final step. **Figure 47** shows that the POD_{cloudy}, hit rate, and KSS are smaller in summer than in the other seasons. Especially in July and August, high FAR_{cloudy} and low scores of POD_{cloudy}, hit rate, and KSS are apparently related to the higher uncertainty in predicting the location and timing of the occurrence of convection in summer.

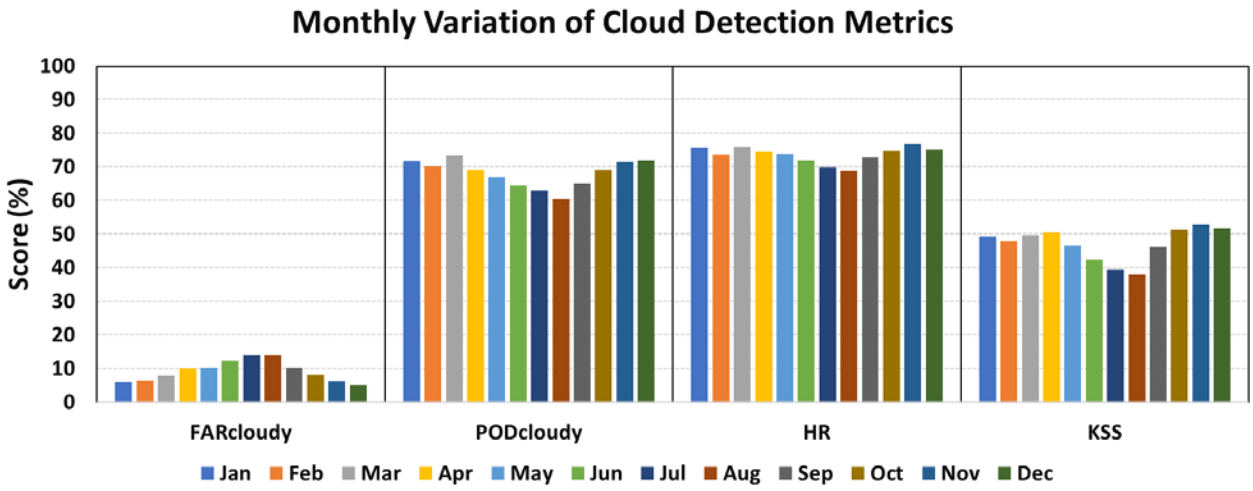

Figure 47. Monthly variation of FAR_{cloudy}, POD_{cloudy}, hit rate, and KSS of WRF-Solar EPS for 2018

To investigate the uncertainties in predicting different types of clouds from WRF-Solar EPS, we analyzed two metrics (POD_{cloudy} and FAR_{cloudy}) classified using cloud optical depth (OPD) and cloud top height (CTH) ranges with data obtained from WRF-Solar EPS and the NSRDB. **Figure 48** shows monthly POD_{cloudy} and FAR_{cloudy} classified into cloud optical depth and cloud top height for CONUS in 2018. Given the POD_{cloudy} and FAR_{cloudy}, WRF-Solar EPS provides accurate forecasts for high and thick clouds, whereas low and thin clouds cause difficulties in predicting cloud masks from WRF-Solar EPS. Consistent with the results of the cloud detection metrics shown in **Figure 47**, patterns of the classified POD_{cloudy} and FAR_{cloudy} for different cloud optical depths and cloud top heights are similar throughout the seasons, noting that WRF-Solar produces lower POD_{cloudy} and higher FAR_{cloudy} in summer than winter.

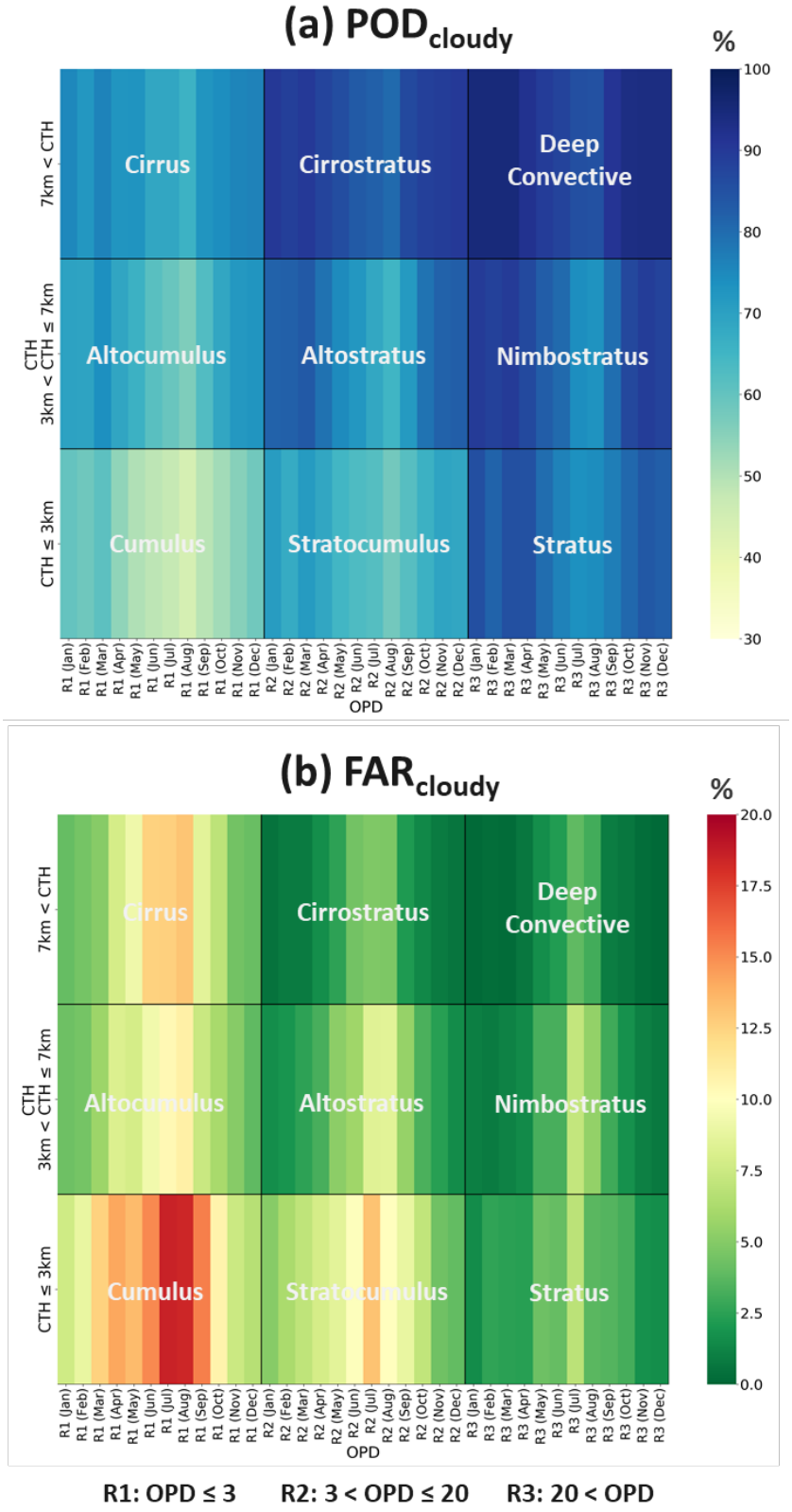

Figure 48. (a) POD_{cloudy} and (b) FAR_{cloudy} of WRF-Solar EPS classified in three cloud optical depths and three cloud levels for 2018

5 Summary

This report presents the development of WRF-Solar EPS to improve the management of the variability and uncertainty of solar generation. The main research steps in developing WRF-Solar EPS include (1) tangent linear sensitivity analysis for identifying key variables significantly related to the forecasting of cloud and solar irradiance, (2) combining the stochastic perturbation method with WRF-Solar, and (3) ensemble calibration to improve the probabilistic forecasts simulated from WRF-Solar EPS.

The major achievements and findings in (1), (2), and (3) are:

1. Fourteen key variables responsible for the largest uncertainties in surface irradiance and clouds were identified using tangent linear analysis of six physics packages of WRF-Solar.
2. The stochastic perturbations were added to the 14 variables selected inside the six WRF-Solar modules. The technique was fully linked to the WRF-Solar name list with a user-friendly interface that provides controllable parameters of stochastic perturbations using configuration files in the model package.
3. An AnEn method was used to calibrate the stochastic ensemble forecasts. The improvements obtained by the ensemble calibration are shown with bias reductions of 81% and 75% with respect to the stochastic ensemble for GHI and DNI, respectively. Overall, the ensemble forecasts calibrated from the analog method provided unbiased estimations of the irradiance within 1% of the satellite observations of GHI and 3.2% of DNI.

In addition, we successfully implemented the AnEn technique to calibrate solar irradiance forecasts simulated from WRF-Solar EPS for 10 sites determined by Topic Area 1. The AnEn calibration improved GHI and DNI forecasts with a reduction in RMSE and a bias removal of raw ensemble forecasts. These final forecast products were uploaded to the Solar Forecast Arbiter for the Topic Area 1 evaluation plan.

In this report, we also described plans for future enhancements to reduce errors in solar irradiance forecasts with the WRF-Solar model (sections 4.4 and 4.5).

Last, the WRF-Solar EPS model is already publicly available. It is an open-source model for the solar energy community that can provide a baseline level of forecasts for grid operation in the United States. Because the system will fit directly into grid operations, there will be a low barrier to adoption, ensuring high impact.

Publications

Conference presentations

Jiménez, P. A., M. Sengupta, Y. Xie, J. H. Kim, J. Dudhia, and B. Kosovic. 2019. "Enhancing WRF-Solar to Provide Probabilistic Cloud Optimized Day-Ahead Forecasts." In *99th American Meteorological Society Annual Meeting*. https://ams.confex.com/ams/2019Annual/meetingapp.cgi/Paper/353075.

Kim, J. H., P. A. Jiménez, M. Sengupta, J. Yang, J. Dudhia, and Y. Xie. 2020. "Enhancing WRF-Solar to Provide Solar Irradiance Probabilistic Forecasts under All-sky Conditions." In *100th American Meteorological Society Annual Meeting*. https://ams.confex.com/ams/2020Annual/meetingapp.cgi/Paper/364754.

Yang, J., M. Sengupta, Y. Xie, P. A. Jiménez, and J. H. Kim. 2020. "Sensitivity Study for Forecasting Variables of WRF-Solar Using a Tangent Linear Approach." In *100th American Meteorological Society Annual Meeting*. https://ams.confex.com/ams/2020Annual/meetingapp.cgi/Paper/365260.

Jiménez, P. A., M. Sengupta, J. H. Kim, J. Yang, J. Dudhia, and Y. Xie. 2021. "An Overview of the WRF-Solar Ensemble Prediction System." In *101st American Meteorological Society Annual Meeting*. https://ams.confex.com/ams/101ANNUAL/meetingapp.cgi/Paper/380565.

Kim, J. H., P. A. Jiménez, S. Alessandrini, J. Yang, M. Sengupta, and J. Dudhia. 2021. "Improving the WRF-Solar Ensemble Prediction Using Analog Ensemble Technique." In *101st American Meteorological Society Annual Meeting*. https://ams.confex.com/ams/101ANNUAL/meetingapp.cgi/Paper/381206.

Yang, J., J. H. Kim, M. Sengupta, P. A. Jiménez, and Y. Xie. 2021. "Evaluating Cloud Forecasts from the WRF-Solar Ensemble Prediction System Using the National Solar Radiation Database." In *101st American Meteorological Society Annual Meeting*. https://ams.confex.com/ams/101ANNUAL/meetingapp.cgi/Paper/379927.

Sengupta, M., P. A. Jiménez, J. Yang, J. H. Kim, J. Dudhia, and Y. Xie. 2021. "New Developments in Ensemble-based Probabilistic Forecasting of Solar Radiation: The WRF-Solar Ensemble Prediction System." *In European Meteorological Society Annual Meeting 2021*. https://meetingorganizer.copernicus.org/EMS2021/EMS2021-347.html.

Sengupta, M., P. A. Jimenez, J.H. Kim, J. Yang, J. Dudhia, Y. Xie, and S. Alessandrini. 2022. "Development of the WRF-Solar Ensemble Prediction System for Ensemble-Based Probabilistic Solar Forecasts." In *102nd American Meteorological Society Annual Meeting*. https://ams.confex.com/ams/102ANNUAL/meetingapp.cgi/Paper/397623

Conference papers

Yang, J., M. Sengupta, Y. Xie, P. A. Jiménez, and J. H. Kim. 2019. "Adjoint Sensitivity of FARMS to the Forecasting Variables of WRF-Solar." Presented at the 2019 European Photovoltaic Specialists Conference (EU PVSEC), Marseille, France, September 9–13, 2019. https://www.nrel.gov/docs/fy19osti/74756.pdf.

Kim, J. H., P. A. Jiménez, J. Dudhia, J. Yang, M. Sengupta, and Y. Xie. 2020, "Probabilistic Forecast of All-sky Solar Radiation Using Enhanced WRF-Solar." Presented at the 37th European Photovoltaic Solar Energy Conference and Exhibition (EU PVSEC 2020), September 7–11, 2020. https://www.nrel.gov/docs/fy20osti/77693.pdf.

Kim, J. H., P. A. Jiménez, M. Sengupta, J. Yang, J. Dudhia, S. Alessandrini, and Yu Xie. 2021. "The WRF-Solar Ensemble Prediction System To Provide Solar Irradiance Probabilistic Forecasts." *In 48th IEEE Photovoltaic Specialists*. https://ieeexplore.ieee.org/stamp/stamp.jsp?tp=&arnumber=9518554.

Yang, J., J. H. Kim, M. Sengupta, P. A. Jiménez, and Y. Xie. 2021. "Assessment of Cloud Mask Forecasts from the WRF-Solar Ensemble Prediction System." In *38th European Photovoltaic Solar Energy Conference and Exhibition*. Presented at the 38th European Photovoltaic Solar Energy Conference and Exhibition (EU PVSEC 2021), September 6–10, 2021. https://www.nrel.gov/docs/fy21osti/80400.pdf.

Journal papers

Yang, J., J. H. Kim, P. A. Jiménez, M. Sengupta, J. Dudhia, Y. Xie, A. Golnas, and R. Giering. 2021. "An Efficient Method to Identify Uncertainties of WRF-Solar Variables in Forecasting Solar Irradiance Using a Tangent Linear Sensitivity Analysis." *Solar Energy* 220: 509–22. https://doi.org/10.1016/j.solener.2021.03.044.

Jiménez, P. A., J. Yang, J. H. Kim, M. Sengupta, and J. Dudhia. 2022. "Assessing the WRF-Solar Model Performance Using Satellite-derived Irradiance from the National Solar Radiation Database." *Journal of Applied Meteorology and Climatology* 61 (2): 129–42. https://doi.org/10.1175/JAMC-D-21-0090.1.

Kim, J. H, P. A. Jiménez, M. Sengupta, J. Yang, J. Dudhia, S. Alessandrini, and Y. Xie. 2021. "The WRF-Solar Ensemble Prediction System to Provide Solar Irradiance Probabilistic Forecasts." *IEEE Journal of Photovoltaics* 12 (1): 141–4. https://doi.org/10.1109/JPHOTOV.2021.3117904.

References

Alessandrini, S., S. Sperati, and L. Delle Monache. 2019. "Improving the Analog Ensemble Wind Speed Forecasts for Rare Events." *Monthly Weather Review* 147 (7): 2677–92.

Berner, J., G. J. Shutts, M. Leutbecher, and T. N. Palmer. 2009. "A Spectral Stochastic Kinetic Energy Backscatter Scheme and its Impact on Flow-Dependent Predictability in the ECMWF Ensemble Prediction System." *Journal of the Atmospheric Sciences* 66 (3): 603–26.

Berner, J., K. R. Fossell, S. Y. Ha, J. P. Hacker, and C. Snyder. 2015. "Increasing the Skill of Probabilistic Forecasts: Understanding Performance Improvements from Model-Error Representations." *Monthly Weather Review* 143 (4): 1295–1320.

Berner, J., S. Y. Ha, J. P. Hacker, A. Fournier, and C. Snyder. 2011. "Model Uncertainty in a Mesoscale Ensemble Prediction System: Stochastic versus Multiphysics Representations." *Monthly Weather Review* 139 (6): 1972–95.

Chen, F., and J. Dudhia. 2001. "Coupling an Advanced Land Surface–Hydrology Model with the Penn State–NCAR MM5 Modeling System. Part I: Model Implementation and Sensitivity." *Monthly Weather Review* 129(4): 569–85.

Delle Monache, L., F. A. Eckel, D. L. Rife, B. Nagarajan, and K. Searight. 2013. "Probabilistic Weather Prediction with an Analog Ensemble." *Monthly Weather Review* 141 (10): 3498–516.

Delle Monache, L., T. Nipen, Y. Liu, G. Roux, and R. Stull. 2011. "Kalman Filter and Analog Schemes to Postprocess Numerical Weather Predictions." *Monthly Weather Review* 139(11): 3554–70.

Deng, A., N. L. Seaman, and J. S. Kain. 2003. "A Shallow-Convection Parameterization for Mesoscale Models. Part I: Submodel Description and Preliminary Applications." *Journal of the Atmospheric Sciences* 60 (1): 34–56.

Giering, R., and T. Kaminski. 1998. "Recipes for adjoint code construction." *ACM Trans. Math. Software* 24: 437–474.

Habte, A., M. Sengupta, and A. Lopez. 2017. *Evaluation of the National Solar Radiation Database (NSRDB): 1998–2015*. Golden, CO: National Renewable Energy Laboratory. NREL/TP-5D00-67722.

Jiménez, P. A., J. P. Hacker, J. Dudhia, S. E. Haupt, J. A. Ruiz-Arias, C. A. Gueymard, G. Thompson, T. Eidhammer, and A. Deng. 2016a. "WRF-Solar: Description and Clear-Sky Assessment of an Augmented NWP Model for Solar Power Prediction." *Bulletin of the American Meteorological Society* 97 (7): 1249–64.

Jiménez, P. A., S. Alessandrini, S. E. Haupt, A. Deng, B. Kosovic, J. A. Lee, and L. Delle Monache. 2016b. "The Role of Unresolved Clouds on Short-Range Global Horizontal Irradiance Predictability. *Monthly Weather Review* 144 (9); 3099–107.

Jiménez, P. A., J. Yang, J. H. Kim, M. Sengupta, and J. Dudhia. 2022. "Assessing the WRF-Solar Model Performance Using Satellite-Derived Irradiance from the National Solar Radiation Database." *Journal of Applied Meteorology and Climatology* 61 (2): 129–42.

Jiménez, P. A., M. Sengupta, J. H. Kim, J. Yang, J. Dudhia, and Y. Xie. 2021. "An Overview of the WRF-Solar Ensemble Prediction System." In *101st American Meteorological Society Annual Meeting*. AMS.

Karlsson, K. G., and E. Johansson. 2013. "On the Optimal Method for Evaluating Cloud Products from Passive Satellite Imagery Using CALIPSO-CALIOP Data: Example Investigating the CM SAF CLARA-A1 Dataset." *Atmospheric Measurement Techniques* 6 (5): 1271–86.

Kim, J. H., P. A. J. Munoz, M. Sengupta, J. Yang, J. Dudhia, S. Alessandrini, and Y. Xie. 2021. "The WRF-Solar Ensemble Prediction System to Provide Solar Irradiance Probabilistic Forecasts." *IEEE Journal of Photovoltaics* 12 (1): 141–4.

Kim, J. H., P. A. Jiménez, J. Dudhia, J. Yang, M. Sengupta, and Y. Xie. 2020. *Probabilistic Forecast of All-Sky Solar Radiation Using Enhanced WRF-Solar*. Presented at the 37th European Photovoltaic Solar Energy Conference and Exhibition (EU PVSEC 2020), September 7–11, 2020. NREL/CP-5D00-77693.

Nakanishi, M., and H. Niino. 2009. "Development of an Improved Turbulence Closure Model for the Atmospheric Boundary Layer." *Journal of the Meteorological Society of Japan. Ser. II* 87 (5): 895–912.

Sengupta, M., P. A. Jimenez, J.H. Kim, J. Yang, J. Dudhia, Y. Xie, and S. Alessandrini. 2022. "Development of the WRF-Solar Ensemble Prediction System for Ensemble-Based Probabilistic Solar Forecasts." In *102nd American Meteorological Society Annual Meeting*. AMS.

Sengupta, M., P. Jiménez, J. Yang, J. H. Kim, and Y. Xie. 2021. "New Developments in Ensemble-based Probabilistic Forecasting of Solar Radiation: The WRF-Solar Ensemble Prediction System" (No. EMS2021-347). *Copernicus Meetings*.

Sengupta, M., Y. Xie, A. Lopez, A. Habte, G. Maclaurin, and J. Shelby. 2018. "The National Solar Radiation Database (NSRDB)." *Renewable and Sustainable Energy Reviews* 89: 51–60.

Shutts, G. 2005. "A Kinetic Energy Backscatter Algorithm for Use in Ensemble Prediction systems." *Quarterly Journal of the Royal Meteorological Society: A Journal of the Atmospheric Sciences, Applied Meteorology and Physical Oceanography* 131 (612): 3079–102.

Talagrand, O. 1991. "The use of adjoint equations in numerical modeling of the atmospheric circulation." *Automatic Differentiation of Algorithms: Theory, Implementation, and Application*: 169–180.

Thompson, G., P. R. Field, R. M. Rasmussen, and W. D. Hall. 2008. "Explicit Forecasts of Winter Precipitation Using an Improved Bulk Microphysics scheme. Part II: Implementation of a New Snow Parameterization." *Monthly Weather Review* 136 (12): 5095–115.

Thompson, G., R. M. Rasmussen, and K. Manning. 2004. “Explicit Forecasts of Winter Precipitation Using an Improved Bulk Microphysics Scheme. Part I: Description and Sensitivity Analysis.” *Monthly Weather Review* 132 (2): 519–42.

Xiao, Q., Y. H. Kuo, Z. Ma, W. Huang, X. Y. Huang, X. Zhang, D. M. Barker, J. Michalakes, and J. Dudhia. 2008. “Application of an Adiabatic WRF Adjoint to the Investigation of the May 2004 McMurdo, Antarctica, Severe Wind Event.” *Monthly Weather Review* 136 (10): 3696–713.

Xie, Y., J. Yang, M. Sengupta, Y. Liu, and X. Zhou. 2022. “Improving the Prediction of DNI with Physics-Based Representation of All-Sky Circumsolar Radiation.” *Solar Energy* 231: 758–66.

Xie, Y., M. Sengupta, and J. Dudhia. 2016. “A Fast All-Sky Radiation Model for Solar Applications (FARMS): Algorithm and Performance Evaluation.” *Solar Energy* 135: 435–45.

Yang, J., J. H. Kim, P. A. Jiménez, M. Sengupta, J. Dudhia, Y. Xie, A. Golnas, and R. Giering. 2021a. “An Efficient Method to Identify Uncertainties of WRF-Solar Variables in Forecasting Solar Irradiance Using a Tangent Linear Sensitivity Analysis.” *Solar Energy* 220: 509–22.

Yang, J., J. H. Kim, M. Sengupta, P. A. Jiménez, and Y. Xie. 2021b. “Assessment of Cloud Mask Forecasts from the WRF-Solar Ensemble Prediction System.” Presented at the 38th European Photovoltaic Solar Energy Conference and Exhibition (EU PVSEC 2021), September 6–10, 2021. NREL/CP-5D00-80400.

Yang, J., M. Sengupta, Y. Xie, P. A. Jiménez, and J. H. Kim. 2019. Adjoint Sensitivity of FARMS to the Forecasting Variables of WRF-Solar. Presented at the 2019 European Photovoltaic Specialists Conference (EU PVSEC), Marseille, France, September 9–13, 2019. NREL/CP-5D00-74756.

Zhang, X., X. Y. Huang, and N. Pan. 2013. “Development of the Upgraded Tangent Linear and Adjoint of the Weather Research and Forecasting (WRF) Model.” *Journal of Atmospheric and Oceanic Technology* 30 (6): 1180–88.